VRIJE
UNIVERSITEIT
BRUSSEL

MASTER THESIS

The Strong CP Problem and Gravitational Waves

Kevin Turbang

June 3, 2020

Promotor: Professor Alberto Mariotti
Co-promotor: Dr. Iason Baldes

Sciences and Bio-Engineering Sciences

Abstract

Gravitational waves were predicted as part of Einstein's theory of general relativity a bit more than a century ago. These can be generated during high energetic transient phenomena such as the merger of binary neutron stars or binary black holes. However, the interest of this work will be in a different type of signal, namely a stochastic background of gravitational waves. It is a quasi-continuous signal of gravitational waves which permeates the Universe and as such, is the equivalent of the Cosmic Microwave Background for photons. Such a stochastic background can be generated during phase transitions in the cosmological evolution of the Universe. The generation of gravitational waves from the so-called Peccei-Quinn phase transition will be the focus of this thesis. The introduction of the Peccei-Quinn symmetry arises as a possible solution to the Strong CP problem. This problem stems from a CP violating term which has to be included to the Standard Model Lagrangian. This term contributes to the neutron electric dipole moment (eDM) and its coefficient, called the θ-angle, can be constrained to be less than 10^{-9} from measurements of the neutron eDM. The question why this angle is so small compared to other sources of CP violation in the SM, which are of $\mathcal{O}(1)$, is known as the Strong CP problem. This problem as well as a possible solution involving the Peccei-Quinn symmetry will be reviewed in this thesis, after which original work is conducted on the analysis of the Peccei-Quinn phase transition leading to a stochastic gravitational wave background.

Contents

1 Introduction

This thesis brings together two topics, namely gravitational waves generated from phase transitions and the Strong CP problem. Both are briefly introduced below, after which the connection between the two is explained and the structure of the thesis is outlined.

Most of us are familiar with the concept of phase transitions. If not, think of one of the most day-to-day examples: boiling water, where it changes from liquid to gas. Phase transitions in the context of fundamental physics relate to changes of the vacuum state during the evolution of the universe. The phase transition is the process of going from some false vacuum to the lower energy true one. Two qualitatively different ways to go from one vacuum to the other can be distinguished: first or higher order phase transition [1]. The difference is that a barrier in the potential is present in the case of a first order phase transition, which forces the process to happen via quantum tunneling or thermal fluctuation. If the transition is second or higher order, one can just roll from the false vacuum into the true vacuum, as no barrier is present. First order phase transitions are of particular interest because they can give rise to gravitational waves. Gravitational waves (GW) are solutions of the Einstein equation and are fluctuations of space-time that travel at the speed of light [2, 3]. During first order phase transitions, bubbles will form, in much the same way as bubbles form when boiling water. Various bubbles of true vacuum start appearing in a sea of false vacuum. The bubbles themselves cannot generate a GW signal, because the gravitational wave signal is related to the quadrupole moment, which is only non-zero if asymmetry is present in the system [4]. Nevertheless, the collision of such bubbles will break the symmetry and allow for the generation of gravitational waves.

The other topic addressed in this work is one of the problems in the Standard Model (SM). The SM is one of the biggest successes in physics and has been proven to describe a multitude of physical processes to high accuracy. However, some aspects remain unexplained by it, e.g. dark matter, neutrino masses and the hierarchy problem. Another aspect that cannot be understood with the SM theory is called the Strong CP problem. The strong CP problem stems from the fact that a term $\frac{\theta}{32\pi^2} G_{\mu\nu}\tilde{G}^{\mu\nu}$ cannot be excluded on the basis of symmetries from the QCD Lagrangian of the SM. This term contains the gluon field strength $G_{\mu\nu}$ and its dual denoted $\tilde{G}^{\mu\nu}$. This term is odd under parity, but even under charge conjugation and thus, violates CP. This extra term contributes to the neutron electric dipole moment (eDM). However, strong experimental bounds exist on the value of the neutron eDM, constraining the value of θ to be less than 10^{-9} [5]. One recalls that the other sources of CP violation in the SM come from the CKM matrix and are all of $\mathcal{O}(1)$ [6]. The smallness of the θ-parameter compared to the CP violating CKM terms is dubbed the Strong CP problem. Various solutions to this problem have been suggested, including one proposed by Peccei and Quinn [7, 8]. This solution consists of adding an anomalous U(1) symmetry to the SM model, called the Peccei-Quinn symmetry. This $\mathrm{U}(1)_{PQ}$ will be spontaneously broken, giving rise to a Goldstone boson, called

the axion. Due to the coupling to gluons coming from the anomaly, the axion enters in the same term as the θ-term. The vacuum expectation value of the axion is such that it cancels with the θ, resulting in the vanishing of the $G\tilde{G}$ term and thus, solving the Strong CP problem.

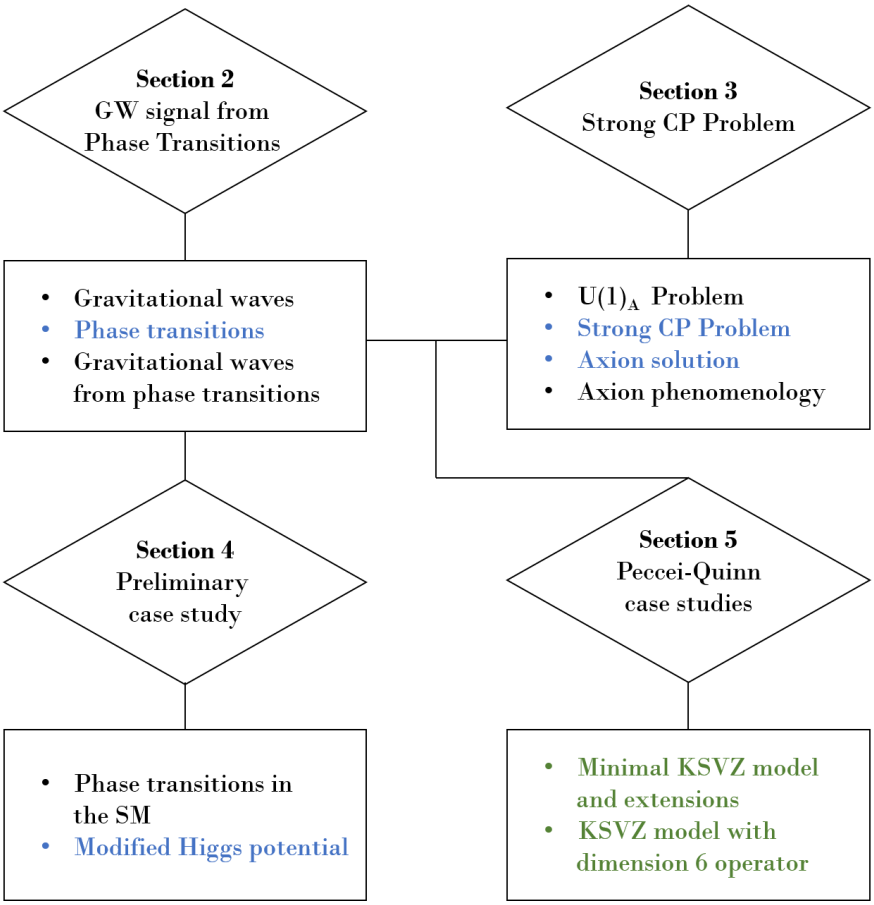

Figure 1: Diagram illustrating the structure of the thesis, where black stands for a review of the theory, blue for sections including the reproduction of existing results and green for original contributions.

The two subjects above are united in this work by exploring the prospect of generating a gravitational wave signal from a first order phase transition associated with the breaking of the Peccei-Quinn symmetry. To illustrate the structure of the thesis, a diagram is displayed in Fig. 1. The following color code is used: black stands for a review of the theory, blue for sections including the reproduction of existing results and green for original contributions. The content of the chapters is as follows. Section 2 is dedicated to gravitational waves. Concepts of phase transitions are reviewed and explained in more depth, followed by an overview of how these phase transitions can lead to a stochastic background of gravitational waves. In the following section, Section 3, the Strong CP

problem is addressed, together with some of the proposed solutions. There, the focus will be on the axion solution to the Strong CP problem. Some models, such as the KSVZ and the DFSZ model, as well as the phenomenology of the axion will be discussed. A preliminary case study concerning the electroweak phase transition is performed in Section 4. In this case study, the possibility of having a strong first order phase transition in the SM is explored by adding a cubic term to the Higgs potential. This section takes care of establishing all the necessary skills needed for the axion models studied in Section 5. There, various realizations of the axion are considered, together with the gravitational wave signals generated from first order phase transitions associated with the breaking of $\mathrm{U}(1)_{PQ}$. A large part of this section is devoted to the investigation of an original model[1]. The Peccei-Quinn phase transition is studied in detail and the gravitational wave signal resulting from it is derived. More particularly, it is shown that the model under consideration can be tested at future gravitational wave interferometers, e.g. at the Einstein Telescope, or even at LIGO-Virgo for some range of parameters. Although the Peccei-Quinn phase transition happens at very high scales, unreachable by collider experiments, it can still be probed in gravitational wave signatures, thus opening a new experimental window to models addressing the Strong CP problem.

This master's thesis came about (in part) during the period in which higher education was subjected to a lock-down and protective measures to prevent the spread of the COVID-19 virus. The process of formatting, data collection, the research method and/or other scientific work the thesis involved could therefore not always be carried out in the usual manner. The reader should bear this context in mind when reading this Master's thesis, and also in the event that some conclusions are taken on board.

[1]The gravitational wave spectrum associated with Peccei-Quinn phase transitions has also been studied in three scientific papers [9–11] appearing during the development of this thesis, though for different models.

2 Gravitational wave signal from cosmological phase transitions

The first part of this work will explore the mechanism behind the generation of gravitational waves during cosmological phase transitions. First, gravitational waves will be introduced, together with some aspects related to experimental detection. After this, the theory of phase transitions will be reviewed. This will then be applied to explore the generation of gravitational wave signals from a first order phase transition in the last part of this section.

2.1 Gravitational wave signal

In what follows, gravitational waves are introduced, with an emphasis on a specific type, namely a stochastic background of gravitational waves. Various experiments are discussed and different constraints on this background are mentioned.

A bit more than a century ago, gravitational waves (GW) were predicted by Einstein as part of his theory of general relativity [2,3]. These are solutions to the Einstein equation in the form of waves, traveling at the speed of light. The polarization of the waves can be realized in two different ways, usually denoted '+' and '×' [4]. The passing wave will stretch spacetime in one direction and contract it in the other one. To illustrate this, the effect of the '+' polarized gravitational wave is depicted in Fig. 2. The effect of the '×' polarized one would be very similar, only stretching diagonally instead of vertically and horizontally. The strain $h(t)$ is the quantity used to measure the stretching. It varies in time according to the wave frequency, which in turn depends on the source of the gravitational wave.

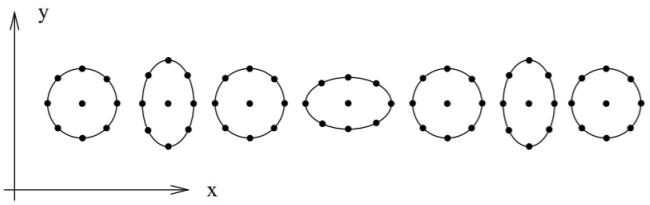

Figure 2: Illustration of the effect of a '+' polarized GW [12].

To make the concept of polarization and strain more concrete, consider a gravitational wave traveling in the z direction [13]. The x and y axes can be chosen arbitrarily. The '+' polarized gravitational wave will stretch and contract space along these two axes. The gravitational wave can be written as

$$h_{ij}(z,t) = h_+ \begin{pmatrix} 1 & 0 & 0 \\ 0 & -1 & 0 \\ 0 & 0 & 0 \end{pmatrix}_{ij} e^{i(kz-\omega t)}, \tag{2.1}$$

where the amplitude of the wave h_+ is the strain that the gravitational wave produces on spacetime. Because of this, spacetime is stretched, inducing a length oscillation in the x direction:

$$L(t) = L_0 + \frac{h_+ L_0}{2} \cos \omega t, \tag{2.2}$$

where L_0 is the length one started with in the x direction. Similarly for the y direction, such that one can write the variation in length due to the gravitational wave as

$$\Delta L_x = \frac{h_+ L_0}{2} \cos \omega t \qquad \text{and} \qquad \Delta L_y = -\frac{h_+ L_0}{2} \cos \omega t. \tag{2.3}$$

Note that these have opposite signs. Indeed, as one direction is stretched, the other one is contracted (as can be seen in Fig. 2). The total change in length in terms of the variation of the two arms is

$$\Delta L = \Delta L_x - \Delta L_y = h_+ L_0 \cos \omega t, \tag{2.4}$$

which at $t = 0$ yields

$$h_+ = \frac{\Delta L}{L_0}. \tag{2.5}$$

This briefly illustrates how the strain relates to the variation in arm length of gravitational wave detectors. For a complete review on the subject, see [14].

The first indirect detection of gravitational waves was realized through the observation of a binary pulsar whose orbit was noticed to decay [15]. Matching the energy loss due to the emisson of gravitational radiation, its orbital decay was soon attributed to emission of gravitational waves. A direct detection was instead only achieved recently by the LIGO-Virgo collaboration [16]. This direct discovery of GW in 2016 marked an extraordinary success of the theory of general relativity, confirming Einstein's prediction one century later.

LIGO and Virgo are two of the cutting-edge experiments to detect gravitational waves. Others, such as the Japanese KAGRA, have just joined or will soon join this worldwide network of so-called second generation gravitational wave detectors [17]. The detection method is the same for the above detectors and is called laser interferometry. As a gravitational wave passes through the L-shaped experiment, a variation in the length of the arms of the interferometer is induced, as was explained above. This can be very precisely measured by detecting the relative phase between the lasers in the two detector arms. This is then converted into the strain h, which quantifies the passage of a GW across Earth.

Gravitational waves are produced in various astrophysical events. These include binary neutron star or binary black hole mergers, supernova explosions, or even neutron stars that display some asymmetry. The LIGO-Virgo collaboration has already proven to be successful by detecting many of these events. The current list includes more than

$O(10)$ events, including gravitational waves originating from the merger of binary black holes and binary neutron stars [18,19]. With the data collected in the current and future runs, many more gravitational wave signals associated to very energetic astrophysical events are expected to be observed. A new way of probing astrophysical phenomena is provided by these observations as this multi-messenger astronomy allows to observe the same astrophysical process through various complementary detection methods, including electromagnetic waves ranging from radio waves to gamma rays and neutrino observations. Furthermore, gravitational waves could have been emitted at the very early stages of the Universe, providing a unique new window to the cosmological history of the Universe.

The efforts to reach higher sensitivities in such experiments do not cease, as the so-called third generation detectors are on their way. As an example, the Einstein Telescope will be part of a new generation of gravitational wave detectors, bringing gravitational wave physics to its full potential. This will be achieved by having a detector with a larger accessible frequency range and an order of magnitude better sensitivity [20]. ET will be a ground-based gravitational wave detector, just like its predecessors. However, a few differences can be noticed compared to the previous detectors. ET will have a triangular shape, corresponding to three nested interferometers, and will be built underground, reducing seismic noise. The arm length will be 10 km instead of 4 km for LIGO and 3 km for Virgo, which will reduce displacement noise. Furthermore, the laser power at the interferometer input will be increased as well. Because of these improvements, ET will be active in the frequency range of a few Hz to a few kHz and should be able to record signals other than coalescing binary systems, such as isolated pulsars, supernovae or even a stochastic background of gravitational waves, which will be explained below.

Another proposed detector is the Laser Interferometer Space Antenna (LISA), which is a space-based laser interferometer expected to be launched in 2030-2035 [21, 22]. It will consist of three identical spacecraft, each 2.5 million km apart, following Earth's orbit around the Sun. This interferometer will allow to probe gravitational wave signals in a lower frequency range, namely 10^{-4} Hz to 10^{-1} Hz, never explored before.

Stochastic background of gravitational waves

Throughout the rest of this work, the interest will be in a specific type of gravitational wave signals, namely a stochastic background of gravitational waves (SBGW). This type of signal significantly differs from the signals associated with the high energetic transient phenomena that were introduced above. A SBGW is a quasi-continuous signal of GW in time which permeates the Universe (see [13] for a review on the topic). It is the equivalent of the Cosmic Microwave Background (CMB) for photons, and as such, it would at first appear as a noise in the detector. As the SBGW is identical to irreducible detector noise, one needs to find a way to disentangle the two. This is where cross-correlation between detectors comes into play and hence, the importance of having more than one detector becomes clear. The idea is that the random output of one detector

acts as a template for the other. The key aspect here is that the SBGW signal will be correlated across detectors, whereas the instrumental noise usually is not. The SBGW would be measured in terms of the amount of energy density which is carried by the SBGW with respect to the critical energy density of the Universe, and is conventionally denoted as

$$\Omega_{\mathrm{GW}}(f) = \frac{f}{\rho_c}\frac{d\rho_{GW}}{df} \tag{2.6}$$

where f denotes the frequency and $\rho_c = \frac{3c^2H_0^2}{8\pi G} \approx 7.6\times10^{-9}$ erg/cm^3 is the critical energy density of the Universe [13]. Equivalently, the energy density of gravitational waves can be considered over a frequency band:

$$\Omega_{\mathrm{GW}} = \int d\ln f \rho_{GW}. \tag{2.7}$$

It is the same parameterization in which e.g. the content of baryonic matter ($\Omega_{\mathrm{baryons}} \simeq 5\%$) or of dark matter ($\Omega_{\mathrm{DM}} \simeq 27\%$) in the Universe is measured [23].

The stochastic background of gravitational waves can usually be divided into two categories depending on its origin. The first one contains the SBGW that could have originated from events taking place during the cosmological evolution of the Universe. These events include inflation and phase transitions, as will be explained in detail in the following subsection. On the other hand, it could have been generated by the superposition of a large number of unresolved sources, resulting in a background from astrophysical origin. These sources can include binary black hole (BBH) mergers, binary neutron star (BNS) mergers, supernovae, pulsars,... Given the current rate of observed binary mergers (BBH and BNS), it is expected that the future Advanced LIGO-Virgo network and future detectors will detect a sizable signal of a SBGW from such unresolved astrophysical sources.

Using astrophysical observations and other measurements, various constraints can be set on the SBGW. These are complementary as the constraints apply to different frequencies, thus covering a large range of frequencies. Fig. 3 shows a summary of the constraints as well as the possible SBGW for several sources.

A first constraint comes from the first two observation runs of LIGO-Virgo, which yielded a limit $\Omega_{\mathrm{GW}}(f)h^2 < 6.0\times10^{-8}$ for frequencies ranging from 20 Hz - 86 Hz [24].

Another constraint comes from pulsars, which are neutron stars that emit regular radio pulses due to the misalignment of their magnetic field dipole axis and the rotation axis [25]. Since the emission of such pulses is very regular, any deviation could be measured and used to detect gravitational waves. A gravitational wave would alter the time between pulses, although many other effects could change the arrival time of the pulses. Among these, there is the decrease of frequency due to energy loss, as well as the dispersion through the interstellar medium that need to be taken into account. After taking this into consideration, a limit on the SBGW can be set, as was already done in 1987: $\Omega_{\mathrm{GW}}(f)h^2 < 4\times10^{-7}$ for a frequency of 7×10^{-7} Hz [26]. More recently, a more

stringent constraint has been established, namely $\Omega_{\rm GW}(f)h^2 < 1.1 \times 10^{-9}$ at 2 nHz [27]. Future experiments such as the Square Kilometer Array (SKA) will be able to probe frequencies in the range $10^{-9} - 10^{-7}$ Hz [28].

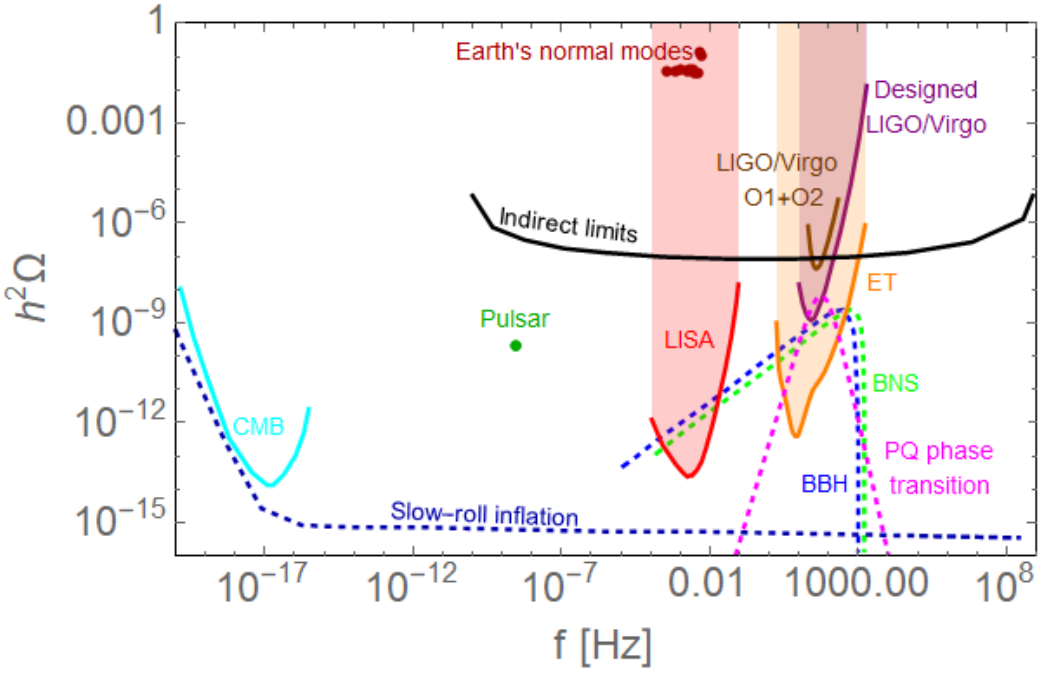

Figure 3: The limits on the SBGW from LIGO's and Virgo's first two observation runs as well as their designed sensitivity are shown. For completeness, the sensitivity of the future LISA [22] and ET [35] detectors are displayed. Various backgrounds are included: binary black holes (BBH), binary neutron stars (BNS), a phase transition in a realization of the Peccei-Quinn model (as obtained in Section 5), as well as slow-roll inflation. All the other lines depict constraints on the SBGW. These come from pulsars, Earth's normal modes, Cosmic Microwave Background (CMB) measurements and indirect limits from CMB and Big-Bang nucleosynthesis (BBN) [10,13,36,37].

Because of its near isotropy, the Cosmological Microwave Background (CMB) can also be used to set constraints on the SBGW. Gravitational waves would generate a quadrupole anisotropy or fluctuations on smaller angular scales. The constraints as displayed in Fig. 3 are such that an energy density above these values would have altered the observations made on the CMB [29–31].

Limits on the energy density of the SBGW can also be inferred from measurements of the normal modes of the Earth. In this case, the limits were established to be ranging from 0.035 to 0.15 for frequencies between 0.3 mHz and 5 mHz [32].

Finally, there are indirect limits on the SBGW energy density. These can be deduced from the abundance of deuterium, helium and lithium. Their production in the Big Bang Nucleosynthesis (BBN) would have been influenced by the gravitational waves. Indeed, an energy density that is too high would have caused the expansion rate of the universe to go up and thus, lowering the amount of helium produced from deuterium.

This would result in different abundances than the ones that are observed today. This yields a constraint $\Omega_{\mathrm{GW}}(f)h^2 < 1.8 \times 10^{-5}$ for frequencies above 10^{-10} Hz [33, 34].

As mentioned above, the detection of gravitational waves started a new era. It will allow to probe physics phenomena at the very early stages of the Universe. Among these phenomena are phase transitions in the Universe. This work will explore the possibility of generating a detectable gravitational wave signal from phase transitions. To this end, the theory of phase transitions is reviewed in the following subsection, after which it will be discussed in the context of gravitational waves.

2.2 Stochastic background of gravitational waves from phase transitions

In this subsection, the generation of a stochastic background of gravitational waves from phase transitions is explored. First, the concept of the effective potential and temperature corrections will be treated. This will be followed by a review of the phase transition dynamics. The section will then be concluded by the introduction of a stochastic background of gravitational waves generated from phase transitions.

2.2.1 Effective potential and temperature corrections

Phase transitions will prove to constitute a possible contribution to the stochastic background of gravitational waves described in the previous section. Before considering phase transitions themselves, the concept of effective potential is introduced, following the approach of [1]. This is a fairly technical subsection where the formulas needed to evaluate the quantum and thermal corrections to the tree-level potential are introduced, as well as some aspects of renormalization. The reader not interested in these details can look at Eq. (2.11), (2.14) and (2.15) and move on to Section 2.2.2, where the dynamics of phase transitions is explained.

When thinking of the potential for a scalar field, one usually only takes the tree-level potential into account. A typical example for a scalar field potential is the well known Mexican hat potential, which is given by

$$V_0(\phi) = -\frac{\mu^2}{2}\phi^2 + \frac{\lambda}{4}\phi^4. \tag{2.8}$$

However, this potential gets corrections induced by one-loop and thermal effects. Quantum field theory is perfectly suited to describe particles in a vacuum, but the early stages of the Universe are different from the idealized scenario of a vacuum. With a non-negligible matter and radiation density at high temperature, one needs to move away from regular quantum field theory to thermal field theory. Indeed, in that formalism the background is described as a thermal bath, rather than a vacuum. This field theory at finite temperature will cause thermal corrections to the tree-level potential. Taking the

leading contributions into account, the potential now reads

$$V_{\text{eff}}(\phi, T) = V_0(\phi) + V_1^{\text{CW}}(\phi) + V_T(\phi, T) + V_{\text{Daisy}}(\phi, T), \tag{2.9}$$

where V_0 is the tree-level potential, V_1^{CW} is the one-loop Coleman Weinberg correction (zero-temperature quantum correction), V_T are the thermal corrections with the Daisy correction terms V_{Daisy}.

One-loop correction
The various corrections will not be computed explicitly here, but will be stated for completeness. For a complete review on the subject, [1] can be used. However, it is important to note that when the one-loop correction is computed, one would find this result to be ultraviolet-divergent. Thus, the theory needs to be regularized and divergent contributions are canceled by the introduction of counter-terms, taking the following form

$$V_1^{ct} = \delta\Omega + \frac{\delta m}{2}\phi^2 + \frac{\delta\lambda}{4}\phi^4. \tag{2.10}$$

The coefficients of the counter-terms are then chosen such that the divergences of the one-loop correction cancel with the ones of the counter-terms. The choice of these counter-terms is determined by the choice of renormalization conditions, which determine the so-called renormalization scheme. Here, two possibilities for the renormalization scheme will be discussed.

The first option for renormalization is called $\overline{\text{MS}}$ renormalization. Although the computation will not be performed here, a brief outline of it will be stated for completeness. Starting from the one-loop correction obtained by dimensional regularization, one would find that it is divergent due to a pole $1/(n-4)$, where n is the dimension of space-time. The $\overline{\text{MS}}$ scheme consists of subtracting the term containing this pole by a specific choice of counter-terms. Adding one-loop and counter-terms together, one finds that the divergences cancel and one arrives at a finite effective potential of the form

$$V(\phi) = V_0(\phi) + \frac{1}{64\pi^2}\sum_i n_i m_i^4(\phi)\left(\log\frac{m_i^2(\phi)}{\mu^2} - C_i\right). \tag{2.11}$$

In this expression, n_i are the degrees of freedom with a negative sign for fermions (e.g. -12 for a SM fermion with color charge such as the top quark, etc.) and C_i are constants given by $C_i = 5/6$ for gauge bosons and $C_i = 3/2$ for other fields. Another possibility for the renormalization uses a cut-off regularization (the cut-off arises when performing loop momentum integrals). Using this regularization scheme, one finds a one-loop contribution

$$V_1(\phi) = \frac{1}{32\pi^2}\sum_i n_i\left(m_i^2(\phi)\Lambda^2 + \frac{m_i^4(\phi)}{2}\left(\log\frac{m_i^2(\phi)}{\Lambda^2} - \frac{1}{2}\right)\right), \tag{2.12}$$

where n_i are the degrees of freedom and m_i the mass of the i-th particle.

Furthermore, a convenient choice for the renormalization conditions is that the minimum at the vacuum expectation value (vev) v and the scalar mass do not change with respect to their tree-level value, namely by requiring

$$\left.\frac{d(V_1+V_1^{ct})}{d\phi}\right|_{\phi=v}=0 \qquad \text{and} \qquad \left.\frac{d^2(V_1+V_1^{ct})}{d\phi^2}\right|_{\phi=v}=0. \tag{2.13}$$

Note that in the context of the usual SM content, this is a perfectly well-motivated choice for the renormalization. As the vev of the Higgs field is measured to be around $v \approx 246$ GeV [6], it only makes sense to not want higher order effects to influence this value and thus, require that Eq. (2.13) holds. Starting from Eq. (2.12), adding counter-terms and requiring Eq. (2.13), it can be shown that if the squared masses of the different fields are of the form $m^2(\phi) = m_0^2 + \lambda\phi^2$, the potential takes the form:

$$V(\phi) = V_0(\phi) + \sum_i \frac{n_i}{64\pi^2}\left(m_i^4(\phi)\left(\log\frac{m_i^2(\phi)}{m_i^2(v)}-\frac{3}{2}\right)+2m_i^2(\phi)m_i^2(v)\right), \tag{2.14}$$

where the sum runs over the various fields and v denotes the vev. Similarly, from the expression of the one-loop correction in the $\overline{\text{MS}}$ scheme given by Eq. (2.11), it is also possible to recover the above equation for the one-loop contribution by requiring Eq. (2.13), as shown in Appendix A. Note that in both cases the dependence on μ and Λ has disappeared.

Thermal corrections

On top of the tree-level and one-loop contribution, thermal corrections come into play when considering field theories at finite temperatures [1]. The thermal contribution reads

$$V_T(\phi,T) = \sum_i n_i \frac{g_i T^4}{2\pi^2}\int \mathrm{d}x\; x^2 \log\left(1-(-1)^{F_i}\exp\left(-\sqrt{x^2+\beta^2 m_i^2(\phi)}\right)\right), \tag{2.15}$$

where $\beta = \frac{1}{T}$. Let $J_F(m^2/T^2)$ be the integral above for fermions, i.e. where $F_i = 1$, and $J_B(m^2/T^2)$ for bosons, where $F_i = 0$. Both functions can be approximated by their high-temperature expansion, admitting the following form

$$J_F(m^2/T^2) = \frac{7\pi^4}{360} - \frac{\pi^2}{24}\frac{m^2}{T^2} - \frac{1}{32}\frac{m^4}{T^4}\log\frac{m^2}{a_f T^2} + \dots \tag{2.16}$$

and

$$J_B(m^2/T^2) = -\frac{\pi^4}{45} + \frac{\pi^2}{12}\frac{m^2}{T^2} - \frac{\pi}{6}\left(\frac{m^2}{T^2}\right)^{3/2} - \frac{1}{32}\frac{m^4}{T^4}\log\frac{m^2}{a_b T^2} + \dots, \tag{2.17}$$

where $\log a_f = 2.6351$ and $\log a_b = 5.4076$ [1]. For $T \ll m$, both obey the following relation

$$J_B(m^2/T^2) = J_F(m^2/T^2) = \left(\frac{m}{2\pi T}\right)^{3/2} e^{-m/T}\left(1+\frac{15T}{8m}+\mathcal{O}\left(\frac{T^2}{m^2}\right)\right), \tag{2.18}$$

showing Boltzmann suppression in the case the particles are a lot heavier than the temperature [38].

The last contribution V_{Daisy} is needed because of the fact that the perturbative expansion in finite temperature field theory breaks down. These so-called Daisy corrections arise due to IR divergences. It turns out that these contributions can be parametrized by a shift in the bosonic mass terms as $m_b(\phi)^2 \to m_b(\phi)^2 + \Pi_b(T)$ in Eq. (2.15), where $\Pi_b(T)$ is the self-energy of the bosonic field in the IR limit [39]. Explicit formulas for these shifts will be given when needed in later sections.

2.2.2 Phase transition dynamics

The previous formulas illustrate how the tree level potential gets corrections from the one-loop level, as well as thermal contributions. Now that the concept of effective potential is clear, one can move on to phase transitions. To make this concept more concrete, as well as to illustrate the difference between first and second order phase transitions, two toy models for the potential are considered following [1].

Second order phase transitions
Starting with a second order phase transition, the following potential is considered:

$$V(\phi, T) = D(T^2 - T_0^2)\phi^2 + \frac{\lambda}{4}\phi^4, \tag{2.19}$$

where D, T_0 and λ are constants. This is the typical form one would obtain including the high-temperature expansion in Eq. (2.16) (only for fermions, as the bosonic contribution would include a ϕ^3 term). In a general theory, the above constants would be determined by the underlying parameters and field content of that theory, through the expressions entering the effective potential that was previously introduced. At $T = 0$, the origin is unstable since the mass-squared term is negative, whereas the other minimum is favored and corresponds to $\phi = \pm\sqrt{\frac{2D}{\lambda}}T_0$. This energetically favored state spontaneously breaks the original symmetry $\phi \leftrightarrow -\phi$ of the theory. The $\phi = 0$ is said to be in the symmetric phase, whereas the $\phi \neq 0$ is in the broken phase. The T-dependent curvature is given by

$$m^2(\phi, T) = 3\lambda\phi^2 + 2D(T^2 - T_0^2) \tag{2.20}$$

and the stationary points of the system read

$$\phi(T) = 0, \qquad \phi(T) = \sqrt{\frac{2D(T_0^2 - T^2)}{\lambda(T)}}. \tag{2.21}$$

Let us now consider the evolution of the potential as a function of the temperature. For temperatures above T_0, only the first solution in Eq. (2.21) exists and $m^2(\phi, T) > 0$, such that the origin forms a stable minimum. At $T = T_0$, the potential takes the form

$$V(\phi, T_0) = \frac{\lambda}{4}\phi^4 \tag{2.22}$$

and both stationary points coincide. For temperatures below T_0, we now have that $m^2(\phi, T) < 0$, making the origin a local maximum, and have two new stationary points ($\phi \neq 0$) appearing. As can be noticed, the second order phase transition does not exhibit a barrier between the symmetric and the broken phase. This phase transition is illustrated in Fig. 4.

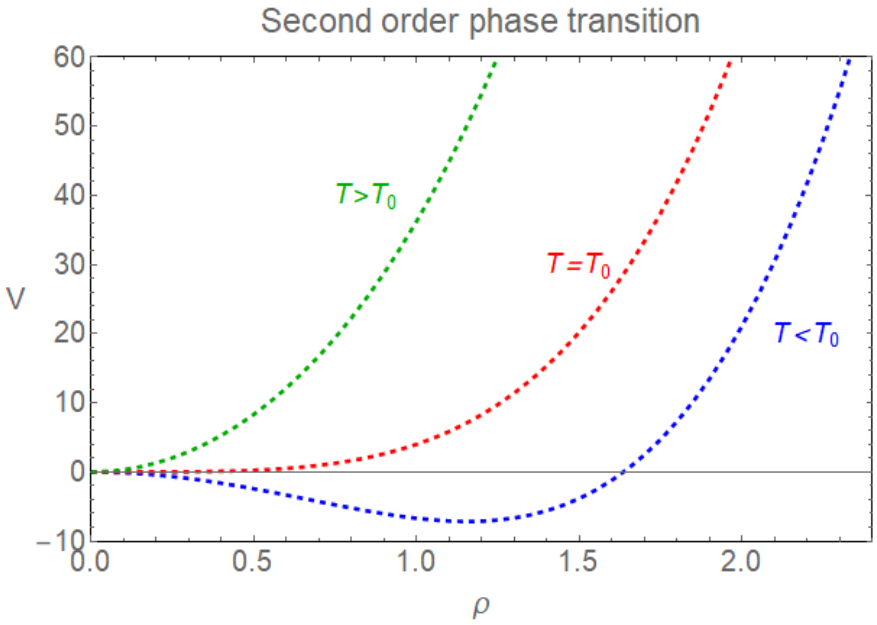

Figure 4: Illustration of a second order phase transition for $D = 1$, $T_0 = 10$ and $\lambda = 16$ in Eq. (2.19). Units have not been specified as only the dimensionless ratio of the parameters matters.

First order phase transitions

The case of a first order phase transition is different, because it contains a barrier between the symmetric and broken phase. This type of phase transition is achieved by adding a cubic term to the previous potential in Eq. (2.19), which now reads:

$$V(\phi, T) = D(T^2 - T_0^2)\phi^2 - ET\phi^3 + \frac{\lambda}{4}\phi^4, \tag{2.23}$$

where D, T_0, λ and E are constants, which would be determined by the underlying parameters of the full theory and its field content. Again starting from high temperature, the only minimum is situated at the origin. As the temperature drops, an inflection point forms, i.e. a point where the graph changes from being concave to convex. This happens at $T = T_1$, where

$$T_1^2 = \frac{8\lambda D T_0^2}{8\lambda D - 9E^2}, \tag{2.24}$$

and field value $\phi(T_1)$:

$$\langle\phi(T_1)\rangle = \frac{3ET_1}{2\lambda}. \tag{2.25}$$

Lowering the temperature even more, causes a barrier to appear between this point and the minimum at the origin. While this happens, the inflection point separates into a maximum and a minimum. The latter and the origin eventually become degenerate when $T = T_c$, where the critical temperature T_c is given by

$$T_c^2 = \frac{\lambda D T_0^2}{\lambda D - E^2}. \tag{2.26}$$

From then on, the origin becomes metastable and the other minimum is now the global one. At some temperature T_0, the barrier completely disappears and the origin becomes a local maximum. The first order phase transition described above is illustrated in Fig. 5.

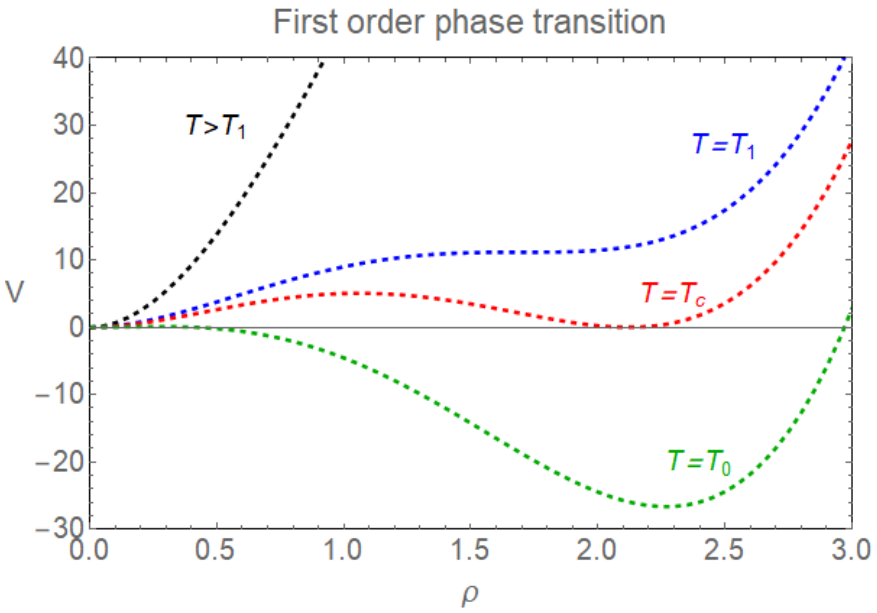

Figure 5: Illustration of a first order phase transition for $D = 2$, $T_0 = 3$, $E = 4$ and $\lambda = 16$ in Eq. (2.23). Units have not been specified as only the dimensionless ratio of the parameters matters.

Bubble dynamics

In the remainder of this section, first order phase transitions are discussed in more detail, as these will be the one of interest in order to generate a gravitational wave signal. The approach of [14] will be used. As seen above, the potential displays two minima for a certain temperature range. After reaching the critical temperature T_c, thermal tunneling from the false vacuum at $\phi = 0$ to the true vacuum at $\phi \neq 0$ can happen via the creation

of bubbles. Indeed, bubbles of the true vacuum (broken phase) will expand in a sea of false vacuum (symmetric phase), converting false vacuum into true vacuum. This is depicted in Fig. 6.

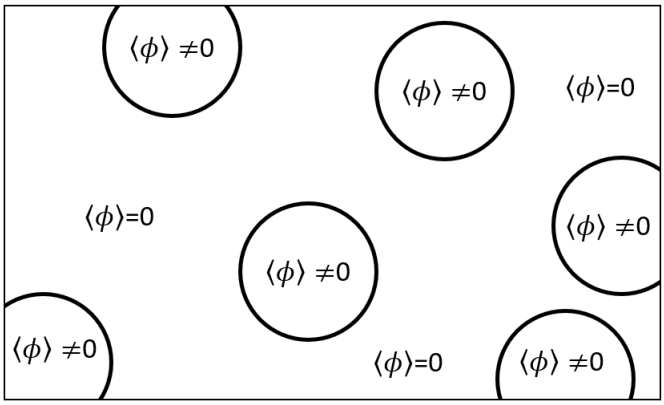

Figure 6: Illustration of the creation of bubbles. The true vacuum lies inside the bubble, whereas the false vacuum is outside.

To describe such a process, the tunneling probability per unit volume is introduced:

$$\frac{\Gamma}{V} = A(T)e^{-S(T)}, \tag{2.27}$$

where $A(T)$ is a proportionality constant and $S(T)$ is the Euclidean action [40–42]. Here, a few comments need to be made about this action. At zero temperature, one starts with the Minkowskian action in four dimensions, which, after a Wick rotation, i.e. $\tau = it$, yields the Euclidean action:

$$S_E = \int d^4x \, \left(\frac{1}{2}(\partial_\mu \phi)^2 + V(\phi) \right), \tag{2.28}$$

where $(\partial_\mu \phi)^2 = (\partial\phi/\partial\tau)^2 + (\partial_i \phi)^2$. It makes sense to look for a solution which possesses the $O(4)$ symmetry of Euclidean space [14]. Thus, a radial coordinate $\rho = \sqrt{\tau^2 + \mathbf{x}^2}$ is defined and a solution $\phi = \phi(\rho)$ is searched for. With this in mind, the action now takes the form

$$S_E(\phi) = 2\pi^2 \int d\rho \; \rho^3 \left(\frac{1}{2} \left(\frac{d\phi}{d\rho} \right)^2 + V(\phi) \right), \tag{2.29}$$

such that the equation of motion reads

$$\frac{d^2\phi}{d\rho^2} + \frac{3}{\rho}\frac{d\phi}{d\rho} - \frac{\partial V}{\partial \phi}(\phi) = 0. \tag{2.30}$$

However, when tunneling at finite temperature, a few modifications need to be made. The potential will now be replaced by the effective potential at finite temperature. Without too many details, it is mentioned that the integration over Euclidean time τ in

Eq. (2.28) happens over a range from 0 to β, where $\beta = \frac{1}{T}$, after which the limit $T \to 0$ or equivalently, $\beta \to \infty$, is taken. However, in the case of finite temperature field theory, this limit is not considered, as one works at finite temperature T. Therefore, the tunneling rate will be obtained from the action

$$S_4(\phi, T) = \int_0^{1/T} d\tau \int d^3x \ \left(\frac{1}{2}(\partial_\mu \phi)^2 + V(\phi, T) \right), \tag{2.31}$$

where the potential was replaced by the effective potential at finite temperature. If $T \to 0$, one goes back to the previous zero-temperature case. On the other hand, when considering finite temperature tunneling, T is large. In this case, the dependence of ϕ on Euclidean time is negligible. This because of the smallness of the range of the Euclidean time. The Euclidean action can thus be approximated by

$$S_4(\phi) \simeq \frac{S_3(\phi)}{T}, \tag{2.32}$$

where

$$S_3(\phi, T) = \int d^3x \ \left(\frac{1}{2}(\partial_i \phi)^2 + V(\phi, T) \right). \tag{2.33}$$

Instead of looking for solutions that possess an $O(4)$ symmetry, it is now reasonable to look for a solution that has an $O(3)$ symmetry. For such a solution $\phi(r)$, the action takes the form

$$S_3(\phi, T) = 4\pi \int_0^\infty \mathrm{d}r \ r^2 \left(\frac{1}{2} \left(\frac{d\phi}{dr} \right)^2 + V(\phi, T) \right). \tag{2.34}$$

The equation of motion is then given by

$$\frac{d^2\phi}{dr^2} + \frac{2}{r}\frac{d\phi}{dr} - \frac{\partial V}{\partial \phi}(\phi, T) = 0, \tag{2.35}$$

with the following boundary conditions

$$\lim_{r \to \infty} \phi(r) = 0 \qquad \text{and} \qquad \frac{d\phi}{dr}(0) = 0. \tag{2.36}$$

Furthermore, $A(T)$ in Eq. (2.27), takes the form cT^4 in the case of the $O(3)$-symmetric solution, where c is a constant of $\mathcal{O}(1)$ [14]. It is important to note that both $O(3)$- and $O(4)$-symmetric solution can exist at the same time, although the smallest action will dominate. This because the action enters the decay rate as e^{-S}. Therefore, the decay rate will be given by

$$\Gamma(T) \simeq \max \left\{ T^4 \exp\left(-\frac{S_3}{T} \right), A(T) \exp\left(-S_4 \right) \right\}. \tag{2.37}$$

The $O(4)$-symmetric solution will dominate up until a certain temperature after which the $O(3)$-symmetric one takes over. This will be illustrated below and in more detail

when considering a case study in Section 4.

The remaining task in computing the tunneling probability Γ/V is to determine the solution of Eq. (2.35). This can be done numerically by using what is called the shooting method [43]. An intuitive way to understand how this bounce solution is computed can be found by reversing the potential, which is illustrated in Fig. 7. One can then consider a ball being dropped from a certain point on the mountain. In that case, the problem reduces to finding the initial value of the field ϕ such that the ball reaches the other top and stops there, ensuring that the boundary conditions in Eq. (2.36) are satisfied within numerical accuracy. Needless to say that this is a task that requires a lot of fine-tuning. Indeed, values a bit lower than the optimal one will cause the ball to never reach the top and oscillate around the minimum. Overshooting will cause the ball to go over the top and never return.

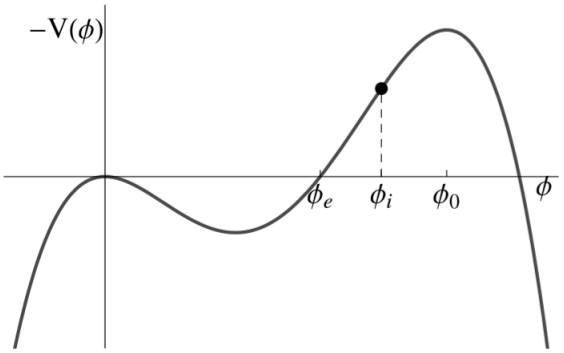

Figure 7: Illustration of the reversed potential together with the optimal field value of ϕ such that the ball reaches the top at the origin [14].

After using the above method to compute the bounce trajectory (depicted in Fig. 8), this solution can be plugged back into the expression for S_3 given by Eq. (2.34) or in Eq. (2.29) to compute S_4. Both are illustrated in Fig. 9. This also shows how S_4 will be smaller for low temperatures and how S_3/T quickly becomes smaller for larger temperatures, thus dominating in the decay rate given by Eq. (2.37). This numerical computation of the bounce action, as well as the computations in the following sections, were performed using Mathematica. In the first instance, the computation of the bounce action was done by using original code. However, it was soon realized that the code of [44] was more efficient for calculating the bounce action, although yielding the same result. Thus, the code of [44] was used for that part of the computations when performing large numerical scans.

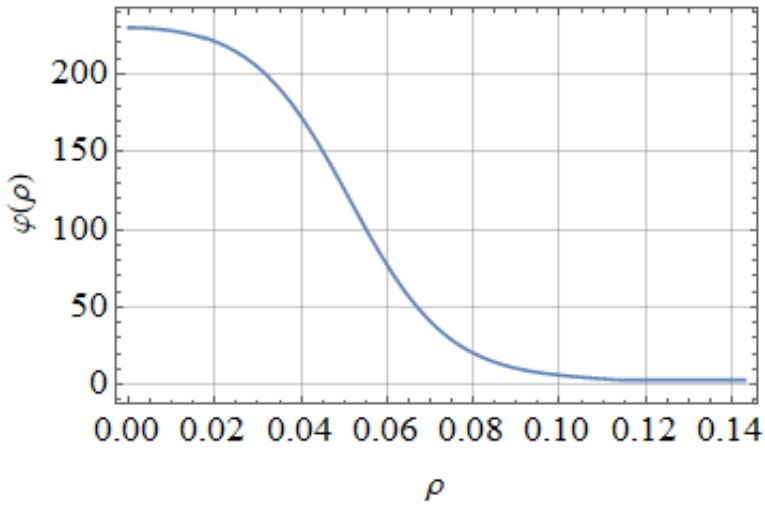

Figure 8: Bounce profile. As can be seen, both boundary conditions in Eq. (2.36) are satisfied. Furthermore, the bounce profile starts at the initial point (think of the mountain) and evolves to be zero at larger ρ, thus going from true to false vacuum.

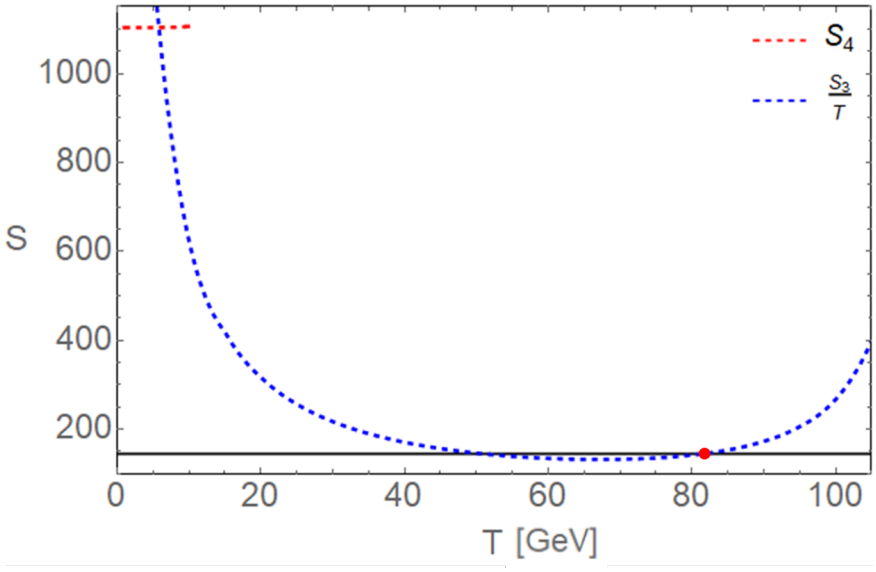

Figure 9: Example of bounce action S_4 and S_3/T. S_4 is smaller for low temperatures, but S_3/T quickly decreases at larger temperatures, making it smaller than S_4. The black line illustrates the nucleation condition in Eq. (2.44). The intersection, given by the red dot, marks the temperature at which this condition is first satisfied as the Universe expands and cools, yielding the nucleation temperature.

The above formulas allow one to compute various quantities related to the creation of bubbles during phase transitions. One can now wonder how these bubbles expand compared to the expansion rate of the Universe. The main question that arises is if the bubbles expand fast enough to convert the whole Universe from false to true vacuum. A key parameter in this analysis is the Hubble parameter $H(t)$ and is given by

$$H(t) = \frac{\dot{a}}{a}, \tag{2.38}$$

where $a(t)$ is the the scale factor, parameterizing the relative expansion of the Universe [4]. The Hubble parameter obeys the so-called Friedmann equation, which in the case of radiation and vacuum domination reads:

$$H^2(T) = \frac{1}{3M_p^2}\left(\frac{T^4}{\xi^2} + \Delta V\right), \tag{2.39}$$

where $M_p = 2.435 \times 10^{18}$ GeV is the Planck mass and $\xi^2 = \frac{30}{\pi^2 g_\star(T)}$ [45]. $g_\star(T)$ is the effective number of relativistic degrees of freedom, given by

$$g_\star(T) = \sum_{i=\text{bosons}} g_i \left(\frac{T_i}{T}\right)^4 + \frac{7}{8}\sum_{i=\text{fermions}} g_i \left(\frac{T_i}{T}\right)^4, \tag{2.40}$$

where g_i is the number of spin or helicity states of the i-th species, T_i its temperature and T is the photon temperature T_γ. Furthermore, ΔV is the difference of the zero-temperature potential evaluated at the false vacuum and the true vacuum. The above definitions allow one to define the bubble nucleation rate inside a Hubble volume $H(t)^{-3}$ as $(\Gamma/V)H(t)^{-3}$. Requiring the number of bubbles that nucleated from time $t = 0$ to $t = t_\star$ to be of $\mathcal{O}(1)$ yields the time $t_\star$ at which the phase transition happened:

$$\int_0^{t_\star} \mathrm{d}t \, \frac{\Gamma}{VH^3(t)} = \mathcal{O}(1). \tag{2.41}$$

As the temperature $T \propto 1/a$, where a is the scale factor as previously introduced, one finds that $\frac{dT}{T} = -H dt$. This can be intuitively understood as follows: the bigger the scale of the Universe, the colder it will be. Using this, one can convert the integral over time to one over temperature, yielding the nucleation temperature $T_\star$:

$$\int_{T_\star}^{T_c} \frac{dT}{T}\frac{\Gamma}{VH^4} = \mathcal{O}(1). \tag{2.42}$$

However, this integral will be dominated by its value at $T_\star$. Thus, to a good approximation, the nucleation temperature is the temperature at which

$$\frac{S_3(T)}{T} \approx 4\log\left(\frac{T}{H}\right) \tag{2.43}$$

holds, where Eq. (2.27) was used [46]. As an example, this can be computed for transitions occurring at the electroweak scale, in which case $g_\star \simeq 106$. The electroweak scale,

roughly 100 GeV, is chosen as the scale entering the Hubble parameter. Indeed, the presence of M_p in $H(T)$ requires the specification of a scale. This yields

$$\frac{S_3(T_\star)}{T_\star} \simeq 4 \ln\left(\frac{M_{\rm p}}{T_\star}\right) - 11.4, \tag{2.44}$$

which, when assuming $T_\star = 100$ GeV, reads $S_3(T_\star)/T_\star \simeq 145$. This is illustrated in Fig. 9 by the black line. The temperature at which the bounce action and the black line intersect is the nucleation temperature $T_\star$. To be precise, there are two intersection points. However, the highest temperature is the relevant one, as this is the first temperature for which the nucleation condition is satisfied when coming from high temperatures.

Apart from the nucleation temperature $T_\star$ defined above, there are two other parameters characterizing the phase transition that will be of importance when considering the generation of gravitational waves. Let $\eta(T)$ be the expectation value at the true vacuum of the effective potential at temperature T. Then, the vacuum energy density of the transition is

$$\rho_\star = \left(-V(\eta(T),T) + T\frac{d}{dT}V(\eta(T),T)\right)\Big|_{T=T_\star}. \tag{2.45}$$

Assuming the transition takes place in the radiation dominated epoch, this quantity is normalized to the radiation energy density, yielding

$$\alpha = \frac{30\rho_\star}{\pi^2 g_\star(T_\star)T_\star^4}, \tag{2.46}$$

which stands for the strength of the phase transition [14]. A second parameter that will be important is the ratio $\beta/H_\star$ and is defined as

$$\frac{\beta}{H_\star} = T_\star \frac{d}{dT}\left(\frac{S_3(T)}{T}\right)\Big|_{T=T_\star}, \tag{2.47}$$

where $H_\star = H(T_\star)$, the Hubble parameter evaluated at the nucleation temperature. This quantity characterizes the inverse of the duration of the phase transition (in Hubble units). Depending on the model, $\beta/H_\star$ ranges from $\mathcal{O}(10)$ to $\mathcal{O}(10^3)$. Furthermore, these parameters usually display a correlation: as α increases, $\beta/H_\star$ and $T_\star$ decrease.

For small values of $\beta/H_\star$, one needs to be more careful with the analysis. Requiring that the number of bubbles per Hubble volume is $\mathcal{O}(1)$, might not be enough to guarantee that the whole Universe will be converted from false to true vacuum. This is where the concept of percolation comes in. It will guarantee that the evolution of the Universe and the bubbles is such, that these bubbles merge and fill the whole Universe, completing the phase transition. Using the decay rate Γ/V, one defines the probability for a point to still be in the false vacuum as

$$P(T) = e^{-I(T)}, \tag{2.48}$$

where

$$I(T) = \frac{4\pi}{3} \int_T^{T_c} \frac{dT'}{T'} \frac{\Gamma(T')}{T'^4 H(T')} \left(\int_T^{T'} \frac{v_w d\widetilde{T}}{H(\widetilde{T})} \right)^3 \tag{2.49}$$

and v_w is the velocity of the bubble wall [47, 48]. The percolation temperature is then defined as the temperature at which this probability is $P(T_p) = 1/e$ or equivalently $I(T_p) = 1$. In other words, the probability of being in the true vacuum at the percolation temperature is roughly 74%. This is not enough to guarantee the completion of the phase transition, especially for cases where vacuum energy dominates. Indeed, one needs to verify that the probability $P(t)$ decreases faster than the increase of the expanding volume under consideration. This can be expressed by the following condition:

$$\frac{1}{\mathcal{V}_{\text{false}}} \frac{d\mathcal{V}_{\text{false}}}{dt}\bigg|_{t=t_p} = H(T) \left(3 + T \frac{dI(T)}{dT} \right) \bigg|_{T=T_p} < 0, \tag{2.50}$$

where $\mathcal{V}_{\text{false}}$ is the physical volume of the false vacuum. Expressed in words, this means that the bubble needs to expand at least as fast as the expansion rate of the volume in which it resides [49]. For large values of $\beta/H_\star$, the value of the percolation temperature T_p and the nucleation temperature $T_\star$ will be roughly equal. On the other hand, when $\beta/H_\star$ is small, the two temperature will generally differ and the percolation temperature T_p should be computed to make sure the phase transition completes.

The above concepts constitute the necessary ingredients to compute the gravitational wave signal associated with a first order phase transition. This will be discussed in the following subsection.

2.2.3 Gravitational waves from first order phase transitions

The three essential parameters describing the phase transition were just introduced, namely α, $\beta/H_\star$ and the nucleation temperature $T_\star$. Before going into the details of the generation of gravitational waves from phase transitions, it is important to stress that these parameters constitute the only necessary ingredients to be able to write down the gravitational wave spectrum. Once these parameters are computed, they can be plugged into the relevant formulas that will be given below and the gravitational wave spectrum follows. Although the parameters above are the only values needed to compute the gravitational wave signal associated with the phase transition, the spectrum might look different depending on the underlying mechanism responsible for the generation of the gravitational waves. These various cases will be the topic of the remainder of this section.

When considering the expansion of bubbles in space, two scenarios come to mind: one where the bubbles expand in vacuum and thus, do not interact with the cosmic fluid, and one where these interactions can not be neglected [14]. In the former case, the bubble will keep expanding until the velocity of its wall reaches the speed of light. As the bubble expands, more and more volume is converted from the false to the true vacuum. The energy gain associated with this transition is converted into kinetic energy of the

bubble wall. Thus, these walls will become more energetic, but at the same time they become thinner due to Lorentz contraction, resulting in an enormous increase in energy density of the bubble walls. As soon as two bubbles collide, the spherical symmetry is broken, allowing gravitational waves to be generated. Asymmetry is needed because the gravitational wave signal is proportional to the second derivative of the quadrupole moment, which measures the shape of the system [4]. A non-zero quadrupole moment is only ensured if the system does not display spherical symmetry. Thus, gravitational waves can only be generated when the system displays some asymmetry.
The more realistic case where bubbles interact with the cosmic fluid is more complex, as the interaction will cause the bubble dynamics to change. Furthermore, the bubble itself will cause turbulence and acoustic waves in the fluid. Concretely, three processes contribute to the generation of gravitational waves:

$$h^2\Omega_{\rm GW} \simeq h^2\Omega_\phi + h^2\Omega_{\rm sw} + h^2\Omega_{\rm turb}, \tag{2.51}$$

where the first term represents contributions from bubble collisions, the second term from sound waves developing in the plasma and the last term from magnetic turbulence. The gravitational signal caused by each of these will be covered in the remainder of this section based on [50].

First, consider the collision of bubbles as a source of gravitational waves. The results are well approximated by the so-called envelope approximation. In this approximation, it is assumed that the energy of the bubbles is stored in the walls, which are thin. The energy then quickly disperses after the collision of two bubbles in such a way that the energy is mostly stored in the uncollided part of the bubbles. Using this approximation, the evolution and collision of bubbles can be numerically simulated, together with the associated gravitational wave spectrum. This yields the following gravitational wave signal

$$h^2\Omega_{\rm env}(f) = 1.67\times10^{-5}\left(\frac{H_\star}{\beta}\right)^2\left(\frac{\kappa\alpha}{1+\alpha}\right)^2\left(\frac{100}{g_\star}\right)^{1/3}\left(\frac{0.11v_w^3}{0.42+v_w^2}\right)S_{\rm env}(f), \tag{2.52}$$

where the spectral shape of the GW radiation is parametrized by $S_{\rm env}(f)$. In this expression, v_w is the velocity of the bubble walls, κ the latent heat converted into kinetic energy of the bubble walls and α and $\beta/H_\star$ are the parameters describing the phase transition as seen in the previous subsection. A fit of the simulated data of bubble collisions and the associated gravitational wave signal gives

$$S_{\rm env}(f) = \frac{3.8(f/f_{\rm env})^{2.8}}{1+2.8(f/f_{\rm env})^{3.8}}. \tag{2.53}$$

The peak frequency of the GW spectrum at time $t = t_\star$ is computed as follows:

$$\frac{f_\star}{\beta} = \left(\frac{0.62}{1.8-0.1v_w+v_w^2}\right), \tag{2.54}$$

which, when red-shifted, corresponds to a peak frequency today of

$$f_{\rm env} = 16.5 \times 10^{-3}{\rm mHz} \left(\frac{f_\star}{\beta}\right) \left(\frac{\beta}{H_\star}\right) \left(\frac{T_\star}{100{\rm GeV}}\right) \left(\frac{g_\star}{100}\right)^{1/6}. \tag{2.55}$$

Secondly, the collision of bubbles can produce bulk motion in the fluid, i.e. acoustic waves. Numerical results are fitted by

$$h^2\Omega_{\rm sw}(f) = 2.65 \times 10^{-6} \left(\frac{H_\star}{\beta}\right) \left(\frac{\kappa_v \alpha}{1+\alpha}\right)^2 \left(\frac{100}{g_\star}\right)^{1/3} v_w S_{\rm sw}(f), \tag{2.56}$$

where the spectral shape is determined by

$$S_{\rm sw}(f) = (f/f_{\rm sw})^3 \left(\frac{7}{4+3(f/f_{\rm sw})^2}\right)^{7/2} \tag{2.57}$$

and the peak frequency, red-shifted to today's value is given by

$$f_{\rm sw} = 1.9 \times 10^{-2}{\rm mHz} \frac{1}{v_w} \left(\frac{\beta}{H_\star}\right) \left(\frac{T_\star}{100{\rm GeV}}\right) \left(\frac{g_\star}{100}\right)^{1/6}. \tag{2.58}$$

Now κ_v stands for the fraction of latent heat converted into sound waves and admits the following form

$$\kappa_v = \begin{cases} \alpha(0.73 + 0.083\sqrt{\alpha} + \alpha)^{-1} & v_w \sim 1 \\ v_w^{5/6} 6.9\alpha(1.36 - 0.037\sqrt{\alpha} + \alpha)^{-1} & v_w \lesssim 0.1. \end{cases} \tag{2.59}$$

Lastly, one needs to take into account the magnetic turbulence developing in the plasma due to the collision of bubbles. Indeed, magnetic fields are created during the phase transition and magnetohydrodynamic turbulence develops, since the plasma is fully ionized. Numerically, one finds

$$h^2\Omega_{\rm turb}(f) = 3.35 \times 10^{-4} \left(\frac{H_\star}{\beta}\right) \left(\frac{\kappa_{\rm turb}\alpha}{1+\alpha}\right)^{3/2} \left(\frac{100}{g_\star}\right)^{1/3} v_w S_{\rm turb}(f), \tag{2.60}$$

where $\kappa_{\rm turb}$ stands for the fraction of latent heat converted into magnetic turbulence. The spectral shape of the GW contribution from sound waves is best fitted by

$$S_{\rm turb}(f) = \frac{(f/f_{\rm turb})^3}{(1+(f/f_{\rm turb}))^{11/3}(1+8\pi f/h_\star)}, \tag{2.61}$$

where $h_\star$ is the value of the inverse Hubble time at production of GW red-shifted to today:

$$h_\star = 16.5 \times 10^{-3}{\rm mHz} \left(\frac{T_\star}{100{\rm GeV}}\right) \left(\frac{g_\star}{100}\right)^{1/6}. \tag{2.62}$$

The peak frequency is well-fitted by

$$f_{\rm turb} = 2.7 \times 10^{-2}{\rm mHz}\frac{1}{v_w}\left(\frac{\beta}{H_\star}\right)\left(\frac{T_\star}{100{\rm GeV}}\right)\left(\frac{g_\star}{100}\right)^{1/6}. \tag{2.63}$$

The previous equations introduced the various contributions to the gravitational wave signal associated with first order phase transitions. In these equations, one notices the introduction of v_w, the bubble wall velocity. This is in general a difficult quantity to determine. Particles in the plasma are transmitted or reflected from the bubble wall, inducing different amounts of friction. The reflected particles will also heat the surrounding plasma with their interactions, further affecting the phase space distribution around the bubble wall and hence the frictional force. This has been studied using various approximations for a number of models [51–55]. In the rest of this thesis, it will be assumed that $v_w = 1$, which has been shown to occur in many phase transitions strong enough to also lead to large GW signals. A detailed examination of the frictional forces which allow a determination of v_w in the context of the models studied below is left for future work. Nevertheless, a criterion of interest that will be checked, is that of Bodeker and Moore [56]:

$$\begin{aligned} &V(\phi_T, T = T_\star) - V(\phi_F, T = T_\star) \\ &+ \frac{T^2}{24}\left(\sum_{\rm bosons}\left(m_b^2(\phi_T) - m_b^2(\phi_F)\right) + \frac{1}{2}\sum_{\rm fermions}\left(m_f^2(\phi_T) - m_f^2(\phi_F)\right)\right) < 0. \end{aligned} \tag{2.64}$$

The first part represents the pressure driving the expansion of the bubble, whereas the second term is the retarding pressure on the wall in the limit of an ultra-relativistic wall. If the above expression is negative, this entails that the first term dominates, causing the expansion to accelerate to an even larger Lorentz factor γ_w, provided the initial friction is small enough to allow relativistic velocities to be reached in the first place. In other words the possibility of having $v_w \simeq 1$ is certainly open in such a phase transition, although not certain. The bubble wall with every increasing γ_w is said to be in the so-called runaway regime. Note that the growth of γ_w may eventually be stopped by higher-order effects before the walls collide [57].

As an illustration of what typical gravitational wave signals generated in phase transitions could look like, a spectrum is plotted together with some experiments for $\alpha = 0.1$ and $\beta/H_\star = 100$ for various temperature scales. This is shown in Fig. 10. From the equations above, it is clear that the peak frequency is partly determined by the temperature $T_\star$ and thus, by the scale of this temperature. This shows that lower scales are favored, as these will give rise to signals that are within sensitivity reach of the experiments.

Remark on errors

To conclude, a comment on the various errors related to the analysis of gravitational waves is made. It is important to note that the above formulas for gravitational wave

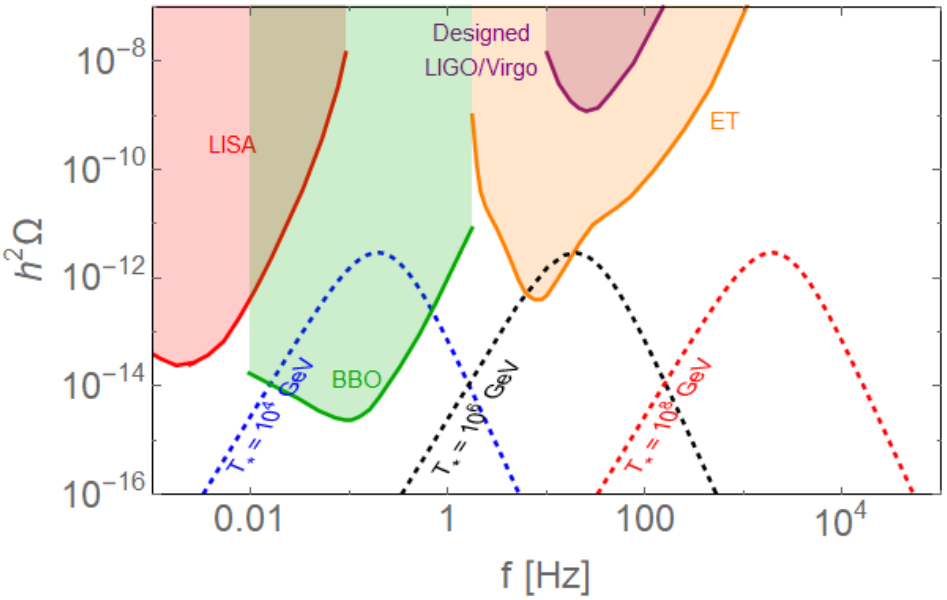

Figure 10: Example of a gravitational wave signals generated by a phase transition for which $\alpha = 0.1$, $\beta/H_\star = 100$ and various values of $T_\star$, i.e. $T_\star = 10^4$ GeV (blue), 10^6 GeV (black) and 10^8 GeV (red), together with the experiments in that range [22, 24, 35, 58].

signals are the result of numerical simulations and still form ongoing research. Therefore, these expressions and thus, the resulting signal, might still be subject to change. As an example, [59, 60] recently suggested that an extra suppression term should be included for the sound wave contribution, due to earlier onset of turbulence, which would further weaken the signal for $\beta/H_\star \ll 1$. Nonetheless, the prediction for the gravitational wave signal used by the LISA working group will be used in this work, i.e. the formulas that were given above [50].

Furthermore, the following remark should be taken into account. The amplitude of the typically dominant sound wave source scales as α^4 for $\alpha \ll 1$ before saturating at $\alpha \sim 1$, following also partly from the hydrodynamical arguments of [61], for the scaling of κ_v. Numerical simulations for the sound wave source had been performed only up to $\alpha = 0.1$ [62], at the time of [50]. The formulas therefore rely on an extrapolation which constitutes another possible source of error. Indeed, subsequent simulations up to $\alpha = 0.67$, showed a suppression from the naive expectation for some transitions with subsonic wall velocities [63].

As most gravitational wave experiments used in this work have not been built yet, the exact errors involved with the sensitivity curves is not known. However, for comparison, the sensitivity curve of LIGO-Virgo is briefly discussed. The sensitivity curve for LIGO-Virgo in Fig. 10 represents the designed sensitivity of the detector. It is such that a stochastic background whose spectrum lies tangent to this curve is detectable with 2σ

significance. Furthermore, these sensitivity curves are determined by assuming that the underlying gravitational wave signal obeys a simple power law. However, the spectra that will be considered in Section 5 are not simple power laws, as opposed to a background from binary black hole or neutron star mergers. Nevertheless, comparing them to the sensitivity curves derived for power law spectra allows to obtain an estimate on whether a detection could be possible or not. As an example, the power-law sensitivity curve for LISA is derived in Appendix D.

This section established the necessary ingredients to describe first order phase transitions and the possible gravitational wave spectrum generated from them. Before considering some specific models and exploring the possibility of such a spectrum, the Strong CP Problem and the axion are discussed in the following section.

3 The Strong CP problem and axions

Besides gravitational waves generated from first order phase transitions, the Strong CP problem and its possible solutions, with an emphasis on the axion, are also considered in this work. This is the topic of this section. Starting from the $U(1)_A$ problem, instantons are reviewed and will play an essential role here. The presence of instantons will eventually lead to the Strong CP problem. The axion solution to this problem and its phenomenology conclude this section.

3.1 The $U(1)_A$ problem

The first part of this section will be dedicated to the $U(1)_A$ problem, as it will introduce some essential concepts such as anomalies and instantons. To this end, consider the QCD Lagrangian for N_f flavors

$$\mathcal{L}_{\text{QCD}} = -\frac{1}{4} G^a_{\mu\nu} G^{a\mu\nu} + \sum_f \bar{q}_f (i\not{D} - m_f) q_f, \tag{3.1}$$

where $G^{\mu\nu}$ is the gluon field strength, q_f the quarks and m_f their mass [64]. Note that for vanishing quark masses, the QCD Lagrangian is symmetric under $U(N_f)_V \times U(N_f)_A$. These transformations denote the vector and axial transformations respectively. To make this more concrete, consider the case $N_f = 1$. These transformations then act on the quarks q as follows:

$$\begin{aligned} U(1)_V &: q \to e^{i\alpha} q, \qquad \bar{q} \to e^{-i\alpha} \bar{q} \\ U(1)_A &: q \to e^{i\alpha\gamma^5} q, \qquad \bar{q} \to \bar{q} e^{i\alpha\gamma^5}. \end{aligned} \tag{3.2}$$

Since $m_u, m_d \ll \Lambda_{\text{QCD}}$, one would expect $U(2)_V \times U(2)_A$ to be an approximate symmetry of the strong interactions. Experimentally, it is found to be true for the vector symmetry, which corresponds to isospin times baryon number ($U(2)_V = SU(2)_V \times U(1)_V$). However, the story is different for the axial symmetry. In this case quark condensates form, i.e. $\langle u\bar{u}\rangle = \langle d\bar{d}\rangle \neq 0$, spontaneously breaking the axial symmetry. Because of this

spontaneous symmetry breaking, one expects four pseudo-Goldstone bosons with small masses (since the symmetry is only approximate for $m_u, m_d \approx 0$). Three of these pseudo-Goldstone bosons are found to be the pions with $m_\pi \approx 0$, but the fourth one seems to be missing as $m_\eta^2 \gg m_\pi^2$. The absence of another light state in the hadronic spectrum is called the $U(1)_A$ problem and suggests that it is not a symmetry of the strong interactions after all [65].

The solution to the $U(1)_A$ problem can be found by looking at the anomaly associated with the axial transformation. Such a transformation acts on the quarks as in Eq. (3.2) and the Noether current associated to this transformation takes the form

$$j_5^\mu = \sum_q \bar{q}\gamma^\mu\gamma^5 q. \tag{3.3}$$

Classically, one would argue that the Noether current is conserved for $m_q \to 0$, since

$$\partial_\mu j_5^\mu = -2i \sum_q m_q \bar{q}\gamma^5 q \to 0. \tag{3.4}$$

However, Adler, Bell and Jackiw showed that the axial symmetry is anomalous, meaning that there is an extra contribution to Eq. (3.4) induced by higher order loops [66, 67]. Indeed, the triangle graph given in Fig. 11 will contribute to the divergence of the current, even in the massless quark limit:

$$\partial_\mu j_5^\mu = \frac{g^2 N_f}{32\pi^2} G^a_{\mu\nu} \widetilde{G}^{a\mu\nu}, \tag{3.5}$$

where N_f represents the number of quark flavors and $\widetilde{G}^{\mu\nu}$ the dual of the field strength defined as

$$\widetilde{G}^{\mu\nu} = \frac{1}{2}\varepsilon^{\mu\nu\rho\sigma} G_{\rho\sigma}. \tag{3.6}$$

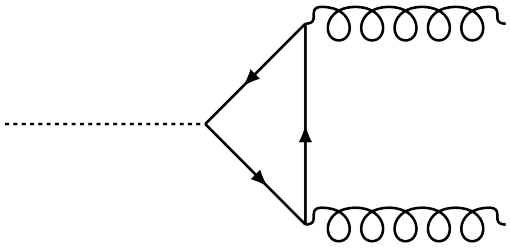

Figure 11: Adler-Bell-Jackiw anomaly.

Since the divergence of the axial current does not vanish, it was just shown that the axial transformation is actually not a symmetry of the Lagrangian, even in the massless case. This means that not finding four light pseudo-Goldstone bosons is not a problem,

because the approximate axial symmetry was never a real symmetry to begin with. However, one soon realizes that the new contribution to the divergence of the current can be written as a total divergence [68]:

$$G^a_{\mu\nu}\widetilde{G}^{a\mu\nu} = \partial_\mu K^\mu, \tag{3.7}$$

where

$$K^\mu = \varepsilon^{\mu\nu\alpha\beta} A_{a\nu}\left(G_{a\alpha\beta} - \frac{g}{3} f_{abc} A_{b\alpha} A_{c\beta}\right). \tag{3.8}$$

Thus, the contribution from the anomaly to the action reads

$$\delta S \propto \int \mathrm{d}^4x \partial_\mu j^\mu_5 = \int \mathrm{d}^4x\ G^a_{\mu\nu}\widetilde{G}^{a\mu\nu} = \int \mathrm{d}^4x\ \partial_\mu K^\mu = \int \mathrm{d}S_\mu K^\mu, \tag{3.9}$$

where Gauss's theorem was used in the last step to convert the integral over the volume into one over the surface. From this it is clear that if the boundary conditions for the gauge fields at infinity are taken to be zero, then the above term does not contribute. This would mean that the anomaly is zero after all and thus, the axial transformation should be a symmetry of nature. Nevertheless, the naive gauge choice that was just mentioned is not the only possibility. To achieve finiteness of the action, it is enough to require that the gauge fields are pure gauge at infinity, i.e. a gauge transform of zero [69]. These non-vanishing gauge configurations are called instantons and will contribute to δS. This means that the presence of instantons contribute to the anomaly. This results in a non-conserved Noether current and thus, no axial symmetry of the Lagrangian.

Instantons

The gauge instanton configurations and their contribution to the action are now considered in more detail. As was just mentioned, it is enough to require the gauge fields to be pure gauge if one wants to realize a finite Euclidean action. This means that

$$A_\mu = \frac{i}{g} M(\Omega)\partial_\mu M^{-1}(\Omega) + \mathcal{O}(r^{-2}), \tag{3.10}$$

where M is a function of the angular variables from four-space to the elements of the gauge group. This assignment is not gauge invariant, since under a gauge transformation $h(x)$, A_μ will transform according to [70]:

$$A_\mu \to \frac{i}{g} h(x)\partial_\mu h^{-1}(x) + h(x) A_\mu h^{-1}(x). \tag{3.11}$$

Thus, for the case of finite action, one gets

$$M \to hM + \mathcal{O}(r^{-2}). \tag{3.12}$$

If it were possible to have h equal M^{-1}, then M could be eliminated from Eq. (3.10) by a gauge transformation and one would only have trivial gauge field configurations, i.e. only gauge configurations of the form $\mathcal{O}(r^{-2})$. However, this can generally not be achieved,

because h must be continuous throughout $\mathbb{R}^4$ and not just on the hypersphere at infinity. To ensure continuity, h must be independent of the angular variables at the origin, i.e. a constant function. Thus, h at infinity is obtained by a continuous deformation from a constant function. Concretely, this means that $M(x)$ can be transformed into any mapping homotopic to $M(x)$, but it cannot be transformed into a function in another homotopy class. Indeed, a function f is said to be homotopic to g, from a space X to a space Y, if and only if there is a map

$$\begin{aligned} &F : X \times [0,1] \to Y \text{ such that} \\ &F(x,0) = f(x) \text{ and } F(x,1) = g(x), \end{aligned}$$

where F is called a homotopy between f and g. In other words, it is a continuous deformation of one function to another [71]. A homotopy class is defined as consisting of all functions that are connected by a homotopy. It turns out that these functions M can be classified in homotopy classes with one integer label, the winding number ν, given by:

$$\nu = \frac{1}{24\pi^2} \int d\theta_1 d\theta_2 d\theta_3 \mathrm{Tr}(\varepsilon^{ijk} M\partial_i M^{-1} M\partial_j M^{-1} M\partial_k M^{-1}), \tag{3.13}$$

where the three θ angles parametrize S^3 and the derivatives are taken with respect to the θ's. A proof will not be given, but can be found in [70]. Furthermore, by applying Eq. (3.10) to Eq. (3.9) and comparing it to Eq (3.13), one can see that

$$\int \mathrm{d}^4x (\varepsilon^{\mu\nu\rho\sigma} G^a_{\mu\nu} G^a_{\rho\sigma}) = \frac{32\pi^2\nu}{g^2}. \tag{3.14}$$

Thus, an integer, called the winding number ν, can be assigned to every finite Euclidean action gauge field. If $\nu = 0$, this corresponds to trivial gauge fields that can be gauged as $\mathcal{O}(r^{-2})$ as $r \to \infty$, whereas $\nu \neq 0$ corresponds to a non-trivial potential that cannot be gauged to zero.

θ-vacua

The above instanton configurations were discussed in a bit more detail, because they provide another way to understand the presence of a θ-term in the Lagrangian. The vacuum structure of a non-abelian gauge theory is richer than one might expect. It turns out that the vacuum states of a non-abelian gauge theory can be divided into different homotopy classes, labeled by a winding number analogous to Eq. (3.13), yielding a multiplicity of vacuum states $|n\rangle$, called winding number vacua [70]. Furthermore, it can be shown that an instanton with winding number ν connects two winding number vacua, m (at $t_E = \infty$) and n (at $t_E = -\infty$), which differ exactly by $\nu = m - n$. For more details one can look at [70, 72].

The true vacuum of the theory, called the θ-vacuum, is constructed as a linear combination of the winding number vacua:

$$|\theta\rangle = \sum_n e^{in\theta} |n\rangle . \tag{3.15}$$

The reason that the winding number vacua cannot be used as true vacuum states, is because in general $\langle m|n\rangle \neq 0$, exactly because of the instanton contributions that connect the different winding number vacua. Thus, the winding number vacua overlap, which is something one does not want for the vacuum states. For two different θ-vacua, one obtains [73]:

$$\langle \theta'|\theta\rangle = \sum_{m,n} e^{-im\theta'} e^{in\theta} \langle m|n\rangle = \sum_{m,n} e^{im(\theta-\theta')} e^{-i(m-n)\theta} \langle m|n\rangle \,, \tag{3.16}$$

where the sum over m will yield a delta function $\delta(\theta - \theta')$ (up to a factor 2π), showing that θ-vacua do not overlap. Furthermore, the vacuum to vacuum transition amplitude can be computed as follows [74]:

$$\begin{aligned}\langle \theta|\theta\rangle &= \sum_{m,n} e^{i\theta(n-m)} \langle m|n\rangle = \sum_{-\nu,n} e^{-i\theta\nu} \langle n+\nu|n\rangle = \sum_{\nu} \int \mathcal{D}[A_\mu]_\nu e^{i(S-\theta\nu)} \\ &= \sum_{\nu} \int \mathcal{D}[A_\mu]_\nu \exp\left[i\left(S + \frac{\theta g^2}{32\pi^2}\int d^4x (\varepsilon^{\mu\nu\rho\sigma} G^a_{\mu\nu} G^a_{\rho\sigma})\right)\right]\end{aligned} \tag{3.17}$$

In this computation, the explicit expression for $|\theta\rangle$, given by Eq. (3.15), was substituted and the path integral formalism was used to express $\langle n+\nu|n\rangle$. The index ν means that the path integral is taken over the fields with instanton number ν. Note that these instanton configurations are exactly the ones connecting the two winding number vacua $|n\rangle$ at $t_E = -\infty$ and $|n+\nu\rangle$ at $t_E = \infty$, as mentioned previously.
From the computation above, it can be seen that choosing the correct θ-vacuum, corresponds to introducing an effective Lagrangian:

$$\mathcal{L}_{\text{eff}} = \mathcal{L} + \frac{\theta g^2}{32\pi^2} (\varepsilon^{\mu\nu\rho\sigma} G^a_{\mu\nu} G^a_{\rho\sigma}). \tag{3.18}$$

Thus, whether one looks at it from the point of view of the anomaly or the one of choosing the correct θ-vacuum, the conclusion is the same: a θ-term needs to be included in the QCD Lagrangian. The properties of this new term as well as its consequences are discussed in the next subsection.

3.2 The Strong CP problem

From the previous subsection, it is clear that an extra term needs to be added to the Lagrangian and this, whether one looks at it from the perspective of the anomaly and instantons or choosing the correct θ-vacuum. This is the term that will eventually lead to the Strong CP problem and is the topic of this section. The new term is added to the Lagrangian as follows:

$$\mathcal{L} \supseteq \frac{\theta_0}{32\pi^2} G_{\mu\nu} \widetilde{G}^{\mu\nu}. \tag{3.19}$$

Furthermore, this new term is consistent with the symmetries of the Lagrangian and has dimension$\leq$4, ensuring renormalizability. Under parity, this new term transforms as

$$\varepsilon^{\mu\nu\rho\sigma} G_{\mu\nu} G_{\rho\sigma} \xrightarrow{P} \varepsilon^{\mu\nu\rho\sigma} (-1)^\mu (-1)^\nu (-1)^\rho (-1)^\sigma G_{\mu\nu} G_{\rho\sigma} = -\varepsilon^{\mu\nu\rho\sigma} G_{\mu\nu} G_{\rho\sigma}. \tag{3.20}$$

where a shorthand notation was used: $(-1)^\mu = 1$ for $\mu = 0$ and -1 for the other indices [64]. Since the field strength and its dual are both even under charge conjugation, the newly added θ-term violates CP. This will be crucial to formulate the Strong CP problem later in this subsection.

One could now wonder if the anomaly described in the previous subsection can not be used to get rid of this new term. Indeed, one could redefine the quarks by using an axial transformation, resulting in an extra term due to the anomaly. This could be done in such a way that it cancels with the θ-term. However, using the axial anomaly of the quarks will result in an extra contribution coming from their mass matrix. This results in an effective θ-angle that can not be rotated away using the anomaly

$$\theta = \theta_0 - \arg\det M, \tag{3.21}$$

where M is the mass matrix of the quarks. Indeed, under anomalous field redefinition $q \to e^{i\alpha\gamma_5}q$, the mass term transforms as:

$$\bar{q}_L M q_R + h.c. \to \bar{q}_L M e^{2i\alpha} q_R + h.c., \tag{3.22}$$

such that $\arg\det M \to \arg\det M + 2\alpha$, explaining the extra contribution in Eq. (3.21) [7]. Nevertheless, if one of the quarks would be massless, the second term in the expression above for the effective θ-angle vanishes. Via field redefinition of the quarks $q \to e^{i\gamma_5\alpha}q$, one would generate an extra θ-like term due to the anomaly. α can then be chosen such that it cancels the θ_0-term in the Lagrangian, thus rotating the θ-term away.

Low energy QCD: the theory of the pions

Before formulating the Strong CP problem and attempting to solve it, a detour is made by considering low energy QCD. This part will show similarities with the beginning of the section, but will explain some aspects in more detail. This will provide essential insights, which can then be applied to the theory of the Strong CP problem and axions. The same approach as the one used in the review on the problem in [75] will be used. Consider the following Lagrangian, representing QCD with two light flavors:

$$\mathcal{L} \supset \frac{\theta g^2}{32\pi^2} G\widetilde{G} + qM\bar{q}, \tag{3.23}$$

where q and $\bar{q}$ are Weyl fermions standing for $q = (u\ d)$ and $\bar{q} = (\bar{u}\ \bar{d})$ and the gluon fields A^a_μ are contained in the field strength G and its dual $\widetilde{G}$. As Dirac fermions were used up until now, a brief explanation about Weyl fermions is given. This is easiest when considering a concrete example, namely the QCD Lagrangian in terms of Dirac fermions in Eq. (3.1) will be written in terms of Weyl fermions [76]. Starting from the Lagrangian expressed in terms of Dirac fermions:

$$\mathcal{L} = \sum_{n=u,d,s,\ldots} \bar{\Psi}_n (i\not{D} - m_n)\Psi_n, \tag{3.24}$$

where D_μ is the $SU(3)_c$ covariant derivative, one can write the Dirac fermions Ψ_n in terms of Weyl spinors. The Dirac fermions contain both left-handed (LH) and right-handed (RH) components. Nevertheless, it could be written in terms of two-component Weyl spinors, i.e. in terms of LH quark fields ψ_n and anti-LH quark fields ϕ_n. The Dirac fermion can then be written as

$$\Psi_n = \begin{pmatrix} -\sigma_2 \phi_n^\dagger \\ \psi_n \end{pmatrix}, \tag{3.25}$$

where ψ_n transforms as a 3 under $SU(3)_c$ and ϕ_n as $\bar{3}$. The Lagrangian now takes the form:

$$\mathcal{L} = \sum_{n=u,d,s,\ldots} i\psi_n^\dagger D_\mu \sigma^\mu \psi_n + i\phi_n^\dagger D_\mu \sigma^\mu \phi_n + m\left(\psi_n \sigma_2 \phi_n + h.c.\right), \tag{3.26}$$

where the notation $\sigma^\mu = \{\mathbb{1}, -\vec{\sigma}\}$ is used, with $\vec{\sigma}$ the Pauli matrices. This brief example illustrates how one can work with Weyl fermions instead of Dirac fermions, as will be done in the remainder of this section.

Since the theory at low energies is strongly coupled, one loses grip on what is going on. However, one can still write down an effective theory of the pions. The above Lagrangian possesses the following symmetry: $SU(2)_L \times SU(2)_R \times U(1)_B \times U(1)_A$. As QCD confines, more particularly $\langle q\bar{q} \rangle \neq 0$, this will break $SU(2)_L \times SU(2)_R$ to its diagonal $SU(2)_D$ and will also break the $U(1)_A$. This spontaneous symmetry breaking will generate Goldstone-bosons. These can be parametrized as

$$U = \exp\left(\frac{i\Pi^a \sigma^a}{\sqrt{2} f_\pi}\right), \tag{3.27}$$

where the σ^i with $i \in \{1,2,3\}$ are the Pauli matrices and $\sigma^0 = \mathbb{1}$. The pion fields are represented by Π^i for $i \in \{1,2,3\}$, while Π^0 is the η' boson associated with the breaking of the $U(1)_A$. It is important to note something about the axial symmetry $U(1)_A$, which is that it is actually not a good symmetry of nature. This was already mentioned at the beginning of this section. Indeed, recall that an axial transformation $q \to e^{i\alpha} q$ and $\bar{q} \to e^{i\alpha} \bar{q}$ will add a term to the Lagrangian as follows:

$$\mathcal{L} \supset \frac{\alpha g^2}{16\pi^2} G\widetilde{G}. \tag{3.28}$$

However, one notices that by shifting θ by -2α in Eq (3.23), one is able to remove the term due to the anomaly. This is what is called a spurion. The idea is that one pretends that a parameter, in this case θ, is actually a field that transforms in such a way that the symmetry is maintained. This can then be used to construct invariant operators, e.g. as will be done when constructing the chiral Lagrangian of the theory. At the end of the computation, the spurion field is set to its constant value. Using this new concept, the anomalous symmetry reads

$$u \to e^{i\alpha} u \qquad d \to e^{i\alpha} d \qquad \theta \to \theta - 2\alpha. \tag{3.29}$$

Note that as these are now Weyl spinors, the γ_5 matrix is not included in the axial transformation rule given by Eq. (3.2). Taking into account that $q \to e^{i\alpha}q$ and that $U \propto q\bar{q}$, the anomalous symmetry can be formulated as

$$U \to e^{i\alpha}U \qquad \theta \to \theta - 2\alpha \qquad M \to e^{-i\alpha}M. \tag{3.30}$$

From the transformation of U, one can read off the anomalous symmetry for the η' boson: $\eta' \to \eta' + \sqrt{2}f_{\eta'}$. With this in mind, the Lagrangian can be written down including the leading-order operators that respect the symmetries, yielding

$$\mathcal{L} = f_\pi^2 \ \mathrm{Tr}\ \partial_\mu U \partial^\mu U^\dagger + a f_\pi^3 \mathrm{Tr} MU + b f_\pi^4 \det U + \mathrm{h.c.}. \tag{3.31}$$

Note that this Lagrangian is invariant under $SU(2)_L \times SU(2)_R \times U(1)_B$, but not $U(1)_A$. This is fine, because $U(1)_A$ was never a true symmetry of nature to start with. The coefficient b can be written as $b = |b|e^{i\theta}$. Indeed, from the properties of determinants and the anomalous symmetry transformation of U, it follows that $\det U \to e^{2i\alpha} \det U$. However, this $e^{2i\alpha}$ can be compensated by the anomalous symmetry of θ in b. From the transformation rule of θ, one finds $b \to be^{i\theta}e^{-2i\alpha}$ which gets rid of the exponent from the transformation of $\det U$. This illustrates how the invariance under the spurious symmetry in Eq. (3.29) is used to dictate the form of the effective Lagrangian in Eq. (3.31) and in particular of the last term in that Lagrangian. It is possible to retrieve the mass term of the η' boson from Eq. (3.31) by expanding it and reads

$$\mathcal{L} \supset \frac{1}{2} m_{\eta'}^2 \left(\eta' - \frac{\theta f_{\eta'}}{\sqrt{2}} \right)^2. \tag{3.32}$$

This expectation value can be plugged in the expression for U, yielding

$$U = e^{i\theta/2} \exp\left(\frac{i\pi^a \sigma^a}{\sqrt{2} f_\pi} \right), \tag{3.33}$$

where the π^a now only stand for the pion fields. The neutral pion π^0 is assumed to get a vacuum expectation value $\langle \pi^0 \rangle = \sqrt{2}\phi f_\pi$, whereas the charged pions will not have a vacuum expectation value. Plugging this back into the previous equation, one finds

$$U = \begin{pmatrix} e^{i\phi + i\theta/2} & 0 \\ 0 & e^{-i\phi + i\theta/2} \end{pmatrix}. \tag{3.34}$$

From Eq. (3.31), one can read off the part that will give rise to the potential for the pions:

$$\begin{aligned} V &= -a f_\pi^3 \mathrm{Tr}\left(\begin{pmatrix} m_u e^{i\theta_u} & 0 \\ 0 & m_d e^{i\theta_d} \end{pmatrix} U \right) + \mathrm{h.c.} \\ &= -2a f_\pi^3 \left(m_u \cos\left(\phi + \frac{\bar{\theta}}{2} \right) + m_d \cos\left(\phi - \frac{\bar{\theta}}{2} \right) \right), \end{aligned} \tag{3.35}$$

where $\bar{\theta} = \theta + \theta_u + \theta_d$. This result was obtained by shifting the ϕ angle as $\phi \to \phi - \frac{\theta_u}{2} + \frac{\theta_d}{2}$. The above potential can be minimized with respect to ϕ, resulting in

$$\frac{\partial V}{\partial \phi} = 2af_\pi^3 \left(m_u \sin\left(\phi + \frac{\bar{\theta}}{2}\right) + m_d \sin\left(\phi - \frac{\bar{\theta}}{2}\right)\right) = 0, \tag{3.36}$$

from which one obtains that

$$\tan\phi = \frac{m_d - m_u}{m_d + m_u} \tan\frac{\bar{\theta}}{2}. \tag{3.37}$$

The sum and difference formulas for cosines can be applied to Eq. (3.35), yielding

$$V = -2af_\pi^3 \left(m_u \left(\cos\phi\cos\frac{\bar{\theta}}{2} - \sin\phi\sin\frac{\bar{\theta}}{2}\right) + m_d \left(\cos\phi\cos\frac{\bar{\theta}}{2} + \sin\phi\sin\frac{\bar{\theta}}{2}\right)\right). \tag{3.38}$$

Using the expression for $\tan\phi$, given by Eq. (3.37), together with the fact that

$$\sin\left(\tan^{-1}(x)\right) = \frac{x}{\sqrt{1+x^2}} \qquad \text{and} \qquad \cos\left(\tan^{-1}(x)\right) = \frac{1}{\sqrt{1+x^2}}, \tag{3.39}$$

one eventually gets

$$V = -2af_\pi^3(m_u + m_d)\sqrt{1 - \frac{4m_u m_d}{(m_u+m_d)^2}\sin^2\frac{\bar{\theta}}{2}}. \tag{3.40}$$

Even though it was derived as the potential for the pions, it will come in handy when considering the axion later on, as it will also act as the potential for the axion.

The Strong CP problem

The introduction of the theory of pions above was two-fold. On one hand, it provides essential insights that will be re-used when considering the axion. On the other hand, this theory allows one to write down the Lagrangian for nucleons, i.e. protons and neutrons, since these consist of three quarks. Indeed, one can write a nucleus field as:

$$N = qqq = \begin{pmatrix} p \\ n \end{pmatrix}, \tag{3.41}$$

where N transforms as a doublet under $SU(2)_L$. Writing down the Lagrangian containing leading-order terms, yields

$$\begin{aligned} \mathcal{L} = &-m_N N U^\dagger N^c - c_1 N M N^c - c_2 N U^\dagger M^\dagger U^\dagger N^c \\ &-\frac{i}{2}(g_A - 1)\left(N^\dagger \sigma^\mu U \partial_\mu U^\dagger N + N^{c\dagger}\sigma^\mu U^\dagger \partial\mu U N^c\right), \end{aligned} \tag{3.42}$$

where arbitrary coefficients were used and $N^c = q^c q^c q^c$, transforming as a doublet under $SU(2)_R$. Expanding U in the pion fields and integrating by parts, the leading CP preserving and CP violating terms are found to be

$$\mathcal{L} = -\bar{\theta}\frac{c_+ \mu}{f_\pi}\pi^a N \tau^a N^c - i\frac{g_A m_N}{f_\pi}\pi^a N \tau^a N^c, \tag{3.43}$$

where $\tau^a = \frac{1}{2}\sigma_a$, $\mu = \frac{m_u m_d}{m_u + m_d}$ and $c_+ = c_1 + c_2$. From experiments, c_+ is determined to be approximately 1.7 and $g_A \approx 1.27$ [75]. From this Lagrangian, one can then compute the Feynman diagram leading to the neutron electric dipole moment (eDM) [77]. Indeed, the $\bar{\theta}$-term will contribute to the neutron eDM. Although this diagram will not be computed explicitly here, the diagram is depicted in Fig. 12 for completeness. The neutron eDM d_n will be related to $\bar{\theta}$. However, a strong bound exists on the neutron electric dipole moment. The neutron's eDM obeys: $|d_n| < 3 \times 10^{-26}$ e cm [5], requiring the $\bar{\theta}$-angle to be less than 10^{-9}. Recall that the parameters entering the only other source of CP violation in the SM can be found in the CKM matrix and are all $\mathcal{O}(1)$ [6]. The reason as to why the newly introduced $\bar{\theta}$-angle is so small, especially compared to the ones in the CKM matrix, is known as the strong CP problem.

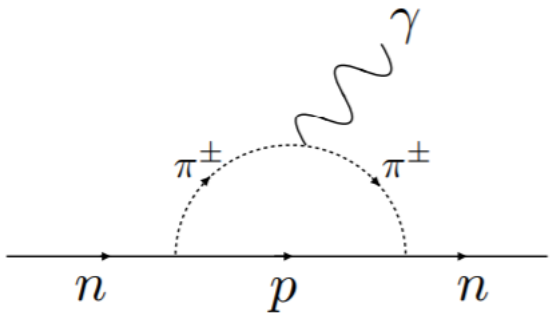

Figure 12: Feynman diagram contributing to the neutron eDM at leading order [75].

Various solutions have been proposed as an attempt to solve the Strong CP problem. One of these solutions is the axion and will be the focus in this work. Nevertheless, two other solutions are mentioned briefly for completeness. The first type of solution assumes that the theory is CP invariant in the UV limit, such that the CKM angles and the θ-angle vanish. This means that somehow CP needs to be broken, since CP is observed to be broken in nature. The challenge here is to find a mechanism such that CP breaking generates the angles present in the CKM matrix, but without reintroducing a physical θ-term. Such a solution is typically referred to as the Nelson Barr model [78, 79].
Another solution to the Strong CP problem would be a massless up quark, as was already hinted at after the introduction of the effective θ-angle in Eq. (3.21). In that case, $\arg\det M = 0$ in Eq. (3.21), which means that the the anomaly can be used to rotate away the CP violating θ-angle, making it unphysical. However, this solution has been ruled out by lattice simulations [80, 81].
The last type of solution consists of adding an extra anomalous U(1) symmetry to the SM, called the Peccei-Quinn symmetry [7,8]. The spontaneous breaking of this symmetry will introduce a new field, the axion. Using this axion solution, it can be shown that its potential is minimized for $\bar{\theta} = 0$, thus solving the Strong CP problem. This solution is the topic of the following subsection.

3.3 Axion solution to the Strong CP problem

As mentioned at the end of the previous subsection, another type of solution consists of introducing a new global anomalous U(1) symmetry, called the Peccei-Quinn symmetry $\mathrm{U}(1)_{PQ}$. This symmetry will eventually be spontaneously broken, resulting in a Goldstone boson: the axion. This new field enters the Lagrangian in the following way:

$$\mathcal{L} \supseteq \frac{1}{2}\partial_\mu a \partial^\mu a + \frac{1}{32\pi^2}\left(\frac{a}{f_a} + \bar{\theta}\right) G_{\mu\nu}\widetilde{G}^{\mu\nu}, \tag{3.44}$$

where a is the axion field [7]. The first term is simply the kinetic term of the axion, whereas the other two terms come from the anomaly. Indeed, recall that the newly added U(1) symmetry is anomalous, thus coupling to the gluon field strength. This can be seen to arise from the anomalous field redefinition $q \to e^{ia/f_a}q$. Indeed, the anomaly will take care of making the axion appear in front of $G\widetilde{G}$. The last term is the usual θ-term. Furthermore, one notices the introduction of f_a, the decay constant of the axion, or in other words, the vacuum expectation value of the field breaking the $\mathrm{U}(1)_{PQ}$. The introduction of the axion means that the static $\bar{\theta}$-angle is promoted to a dynamical variable $\theta(x)$, which now includes the axion field:

$$\theta(x) = \frac{a(x)}{f_a} + \bar{\theta}. \tag{3.45}$$

The potential for the axion can be found by using the following trick: as the θ-angle was promoted to a dynamical variable including the axion, one just substitutes this new dynamical θ-angle in the pion potential in Eq. (3.40), yielding

$$V = -m_\pi^2 f_\pi^2 \sqrt{1 - \frac{4m_u m_d}{(m_u + m_d)^2}\sin^2\left(\frac{a}{2f_a} + \frac{\bar{\theta}}{2}\right)}. \tag{3.46}$$

The above potential is minimized when $\langle a \rangle = -f_a\bar{\theta}$. This implies that $\langle \theta(x) \rangle = 0$, solving the Strong CP Problem. Indeed, if $\theta(x)$ is not zero to begin with, the above arguments show that it will quickly relax to zero.

Furthermore, this potential can be expanded around its minimum, after which the mass term of the axion will appear and its mass can be read off:

$$m_a^2 \approx \frac{m_u m_d}{(m_u + m_d)^2}\frac{m_\pi^2 f_\pi^2}{f_a^2}. \tag{3.47}$$

The values of the various masses in the previous equation can be filled in [82], after which one finds

$$m_a \approx 5.691 \left(\frac{10^9 \mathrm{GeV}}{f_a}\right) \mathrm{meV}. \tag{3.48}$$

It was just shown that the above mechanism provides a way for the neutron electric dipole moment to agree with current experimental constraints, thus solving the Strong CP problem. Different realizations of the $\mathrm{U}(1)_{PQ}$ symmetry are discussed in the remainder of this subsection.

Axion models: the DFSZ and KSVZ model

Various axion models implementing this new $\mathrm{U}(1)_{PQ}$ symmetry exist, two of which are the DFSZ model and the KSVZ model. Concerning the former, although no computations will be performed with this particular realization of the axion and the Peccei-Quinn symmetry breaking, this model is briefly mentioned for completeness [83,84]. The DFSZ model assumes two Higgs doublets, together with a new complex scalar. The two Higgs doublets give mass to the up-type and down-type quarks respectively. Furthermore, it is assumed that the quarks, as well as both Higgs doublets and the new scalar field are charged under $\mathrm{U}(1)_{PQ}$, while the rest of the SM is uncharged under this group. Concretely, the charges are assigned as follows:

$$\begin{aligned} \Phi &\to e^{i\alpha}\Phi, \\ H_d &\to e^{iX_d\alpha}H_d, \\ H_u &\to e^{-iX_u\alpha}H_u, \\ d_i &\to e^{-iX_d\alpha}d_i, \\ u_i &\to e^{-iX_u\alpha}u_i, \end{aligned} \tag{3.49}$$

where Φ is the complex scalar, H_d and H_u are the Higgs doublets giving mass to the down-type and up-type quarks respectively. The Yukawa interactions

$$\mathcal{L}_Y = Y_{ij}\bar{q}_i H_d d_j + \Gamma_{ij}\bar{q}_i \widetilde{H}_u u_j + h.c., \tag{3.50}$$

where $\widetilde{H} = \epsilon H^*$, as well as the potential

$$V(\Phi) = -\mu^2|\Phi|^2 + \lambda|\Phi|^4 + \lambda_3 H_d^\dagger H_u \Phi^2 \tag{3.51}$$

are invariant under $\mathrm{U}(1)_{PQ}$, provided that $X_u + X_d = 2$. After electroweak symmetry breaking, both Higgs doublets will acquire a vacuum expectation value v_d and v_u, giving the usual $v = \sqrt{v_d^2 + v_u^2} \approx 246$ GeV [6]. After PQ symmetry breaking, happening at a scale $f_a \gg v$, the field Φ acquires a vacuum expectation value f_a. After both symmetry breakings, the fields can be parametrized as

$$\begin{aligned} H_d^0(x) &= \frac{v_d + h_d(x)}{\sqrt{2}} \exp\left(i\left(\frac{\zeta(x)}{v} + X_d\frac{a(x)}{f_a}\right)\right) \\ H_u^0(x) &= \frac{v_u + h_u(x)}{\sqrt{2}} \exp\left(i\left(\frac{\zeta(x)}{v} - X_u\frac{a(x)}{f_a}\right)\right) \\ \Phi(x) &= \frac{f_a + \rho(x)}{\sqrt{2}} \exp\left(i\frac{a(x)}{f_a}\right), \end{aligned} \tag{3.52}$$

where the radial modes h_d and h_u are the two physical Higgs fields and ρ the physical scalar singlet. The exponents contain the Goldstone bosons, where one notices the appearance of $a(x)$, the axion field. The fields described above constitute the necessary building blocks for the DFSZ models. However, the focus in this work will be on a different type of model, namely the KSVZ axion model and extensions thereof.

The KSVZ model is one of the simplest axion models, named after Kim, Shifman, Vainshtein and Zakharov [85, 86]. In this model, the SM is extended by introducing a new complex scalar field Φ and a triplet of fermions Q under $\mathrm{SU}(3)_c$. Under $\mathrm{U}(1)_{PQ}$, these transform as follows

$$Q \to e^{-i\alpha/2} Q, \qquad \bar{Q} \to e^{-i\alpha/2} \bar{Q}, \qquad \Phi \to e^{i\alpha} \Phi. \tag{3.53}$$

In the case of the DFSZ model, parts of the SM were charged under $\mathrm{U}(1)_{PQ}$, whereas in the KSVZ model, the SM content remains uncharged. The new contributions to the SM are captured in the following Lagrangian,

$$\mathcal{L} = |\partial \Phi|^2 + \bar{Q} i \not{D} Q + y \Phi \bar{Q} Q + \text{h.c.} - V\left(|\Phi|^2\right), \tag{3.54}$$

where the potential V has the usual Mexican hat shape that will spontaneously break the $\mathrm{U}(1)_{PQ}$ associated to Φ. After spontaneous symmetry breaking, the scalar field can be parameterized by

$$\Phi = \frac{f_a + \rho(x)}{\sqrt{2}} e^{ia(x)/f_a}, \tag{3.55}$$

where f_a is the vacuum expectation value and a the pseudo-Goldstone boson associated with the spontaneous symmetry breaking of the U(1), namely the axion.

Although the Peccei-Quinn mechanism, together with the axion, provides a solution to the Strong CP problem, it still comes with some problems of its own, one of which is the axion quality problem. To briefly illustrate this problem, one can consider the KSVZ model described above. The potential of the scalar field is given by

$$V = -m^2 \Phi \Phi^\dagger + \lambda (\Phi \Phi^\dagger)^2 + y \Phi Q \bar{Q} + h.c., \tag{3.56}$$

which as mentioned previously, is the usual Mexican hat potential. The first issue arises when considering the axion in the context of effective field theory (EFT) [75]. In EFTs, one writes down every coupling allowed by symmetries for a specific particle content. However, as the axion does not possess any symmetry properties, only an anomalous symmetry, one will not be able to prevent couplings as $\varepsilon Q \bar{Q}$ or $\varepsilon \Phi^2$, which break the $\mathrm{U}(1)_{\mathrm{PQ}}$ symmetry. The second problem comes from the fact that quantum gravity is believed to break all symmetries that are not gauged. As this is the case for the anomalous $\mathrm{U}(1)_{\mathrm{PQ}}$ symmetry, one can expect higher-dimensional operators of the form $V \sim \frac{\Phi^n}{M_p^{n-4}}$, where M_p is the Planck mass. Both issues will give extra contributions to the axion potential, shifting its minimum away from $\bar{\theta}$. As an illustration, taking $f_a = 10^{12}$ GeV, one would need to prevent the higher-dimensional operators up to $n > 14$ to guarantee that the minimum does not shift by more than 10^{-10}. This illustrates the severity of the problem and shows that if the $\mathrm{U}(1)_{PQ}$ is to remain a valid solution to the Strong CP problem, the quality problem needs to be addressed. Various solutions have been put forward, including theories where the new U(1) comes from 5D gauge theories or where the extra U(1) is an accidental symmetry. However, these solutions are only mentioned for completeness, but will not be discussed here.

3.4 Phenomenology of the axion

The previous part introduced the theory of the axion as an attempt to solve the Strong CP Problem. However, the axion has not been discovered experimentally yet. Nevertheless, various experiments are able to constrain the different parameters of axion models. Some of these experiments will be described briefly together with the constraints on the axion phase space. For a complete overview, the review [6] can be used.

One of the axion couplings that plays an important role in axion searches is the axion to two photon coupling. The term in the Lagrangian representing this interaction reads

$$\mathcal{L}_{a\gamma\gamma} = -\frac{g_{a\gamma\gamma}}{4} F_{\mu\nu}\widetilde{F}^{\mu\nu} a = g_{a\gamma\gamma}\mathbf{E}\cdot\mathbf{B}a, \tag{3.57}$$

where a is the axion, $F_{\mu\nu}$ the electromagnetic field strength and its dual given by $\widetilde{F}^{\mu\nu} = \frac{1}{2}\varepsilon^{\mu\nu\rho\sigma}F_{\rho\sigma}$ [87]. The coupling constant is given by

$$g_{a\gamma\gamma} = \frac{\alpha}{2\pi f_a}\left(\frac{E}{N} - 1.92\right), \tag{3.58}$$

where $\frac{E}{N} = 0$ for KSVZ models [85, 86] and $\frac{E}{N} = \frac{8}{3}$ for DFSZ models [83, 84]. Thus, even though the axion in the KSVZ model does not couple to photons directly, a photon coupling is achieved due to the mixing between the pions and the axion. The decay width of this process reads

$$\Gamma_{a\to\gamma\gamma} = \frac{g_{a\gamma\gamma}^2 m_a^3}{64\pi}. \tag{3.59}$$

Furthermore, the axion will also couple to nucleons due to its gluon coupling. This reads

$$\frac{\partial_\mu a}{2f_a} c_N \bar{N}\gamma^\mu\gamma_5 N, \tag{3.60}$$

where N represents a nucleon field and $c_p = -0.47$ and $c_n = -0.02$ for the KSVZ model. To illustrate how these couplings can be used to put constraints on the values of f_a and m_a, a non-exhaustive list of various experiments is given below.

A first experiment consists of shining light through a wall. A laser is shot through a region with a large magnetic field, followed by a wall and again another large magnetic field. The incident photon can be converted into an axion in the magnetic field. The axion travels through the wall, whereas the photon is stopped by it. In the region behind the wall, the magnetic field allows the axion to change back into a photon, which is then measured. As the probability of this happening is given by $\Gamma^2_{a\to\gamma\gamma}$, which scales as $\sim g^4_{a\gamma\gamma}$, one is able to obtain constraints on the coupling. The current constraint coming from this experiment was achieved by the OSQAR experiment (Optical Search for QED Vacuum Birefringence, Axions, and Photon Regeneration) and yields $|g_{a\gamma\gamma}| \lesssim 3.5\times10^{-8}$ GeV^{-1} for $m_a \lesssim 0.3$ meV [88].
A second type of experiment that exploits the axion to two photons conversion are helioscopes such as CAST (CERN Axion Solar Telescope). For mixing states, the oscillation

into each one of them is possible (think for example of neutrino oscillations). These helioscopes look for axions produced in the Sun, which then change into photons inside the magnetic field of the experiment. This experiment was able to put the following constraint on the coupling: $|g_{a\gamma\gamma}| < 6.6 \times 10^{-11}$ GeV^{-1} for $m_a < 0.02$ eV [89].
The production of low-mass and weakly interacting particles can take place in hot astrophysical plasmas and because of this, can transport energy out of stars. One can then use the observed lifetime of stars and energy-loss rates to constrain the coupling $g_{a\gamma\gamma}$, such that it does not conflict with observation. Applying this to stars on the horizontal branch (HB) gives $|g_{a\gamma\gamma}| < 6.6 \times 10^{-11}$ GeV^{-1} for $m_a < 0.2$eV [90]. In much the same way, supernovae can be used to constrain axions. The bounds come from requiring that in the process $N + N \to N + N + A$ the axions do not carry away energy equal to the total energy in neutrinos emitted by the supernova. This yields $f_a \gtrsim 4 \times 10^8$ GeV for $m_a \lesssim 0.16$ meV, as illustrated in Fig. 13. However, due to the limited knowledge about supernovae, it is important to look at these constraints as indications rather than sharp bounds [91].

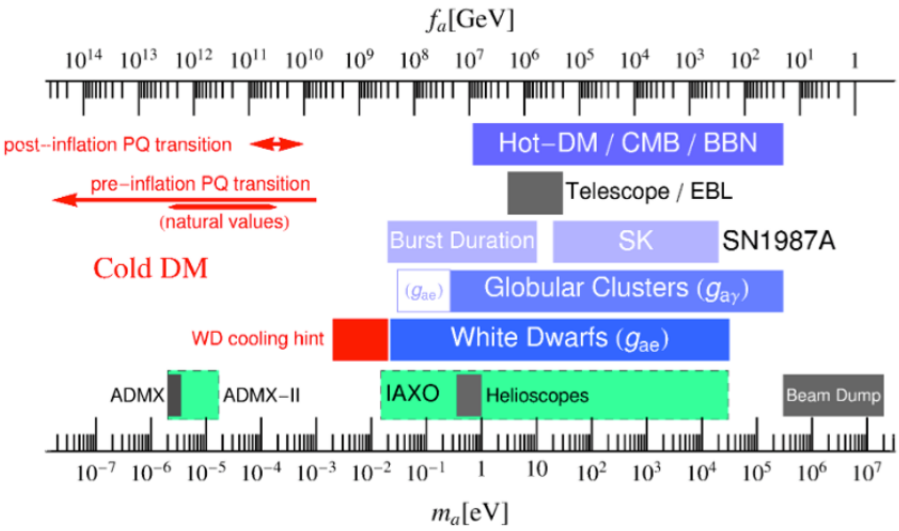

Figure 13: Cosmological and astrophysical constraints on the axion mass m_a and the vacuum expectation value f_a [92].

The coupling to photons and nucleons was discussed in a bit more detail as an example. Nevertheless, various other couplings can be constrained in a similar way, e.g. the coupling to the electron g_{ae}. However, these couplings are model dependent. The focus will be on the couplings of the KSVZ model since only this model, together with extensions of it, will be considered in Section 5. Thus, the only constraints from Fig. 13 one needs to take into account are the ones coming from the supernovae and burst duration. Displayed on this figure is the corresponding a limit on the axion decay constant: $f_a \gtrsim 4 \times 10^8$ GeV [92]. However, a more recent and thorough analysis in [93] obtains a slightly weaker constraint, namely $f_a \gtrsim 2 \times 10^8$ GeV. The latter will be used throughout

the rest of this work. Once again, one needs to remember that these constraints should be regarded as indications rather than sharp bounds. Furthermore, it is important to keep in mind that the final goal is to generate a gravitational wave spectrum from a first order phase transition associated with the potential of the axion. One recalls from the previous section, e.g. Fig. 10, that the lowest scales are favored to generate a signal observable in the frequency range of upcoming detectors. At higher scales, the signal may escape detection.

The question arises if somehow it is not possible to evade the constraints on the axion decay constant f_a and be able to reach lower scales, thus increasing the probability of being within reach of the various experiments. One recalls that the constraints discussed above assume the relation between mass and f_a typical of the QCD axion as in Eq. (3.47). However, this can be modified in more extended theories leading to different phenomenological constraints. In particular, the bound on the decay constant f_a can be significantly weaker. This strategy will not be used in this thesis. Nevertheless, a possible model building strategy to achieve this goal is reported in Appendix B.

With the theory of the axion explained, one might be tempted to jump straight to building models and exploring the generation of gravitational wave spectra. However, a preliminary case study is considered first: the SM with a slightly modified Higgs potential. By doing so, various skills pertaining to the analysis of phase transitions and gravitational wave spectra can be developed. These skills can then readily be applied to axion models.

4 Preliminary case study: the EW phase transition in the SM and beyond

Before considering realizations of models with a Peccei-Quinn symmetry, another model is considered. This sidetrack is taken to develop the necessary skill set that applies to the analysis of first order phase transitions. Concretely, this includes determining the bounce trajectory, followed by calculating the bounce action, as well as the parameters α and $\beta/H_\star$, which will be used to determine the gravitational wave spectrum resulting from this phase transition. To this end, phase transitions are reviewed in the context of the Standard Model, after which a modified Higgs potential is considered.

4.1 Phase transitions in the Standard Model

Before exploring a slight modification of the Higgs potential to achieve a first order phase transition, phase transitions are described in the Standard Model itself. To this end, consider the tree-level Higgs potential, which takes the form

$$V_0(\phi) = \frac{\lambda}{4}(\phi^2 - v^2)^2, \tag{4.1}$$

where the Higgs boson mass is given by $m_h^2 = 2\lambda v^2$, with v the vacuum expectation value, measured to be $v \approx 246$ GeV [6]. As explained in Section 2, the one-loop and thermal contribution need to be taken into account, yielding the effective potential. Using the high-temperature expansion given by Eq. (2.16) and Eq. (2.17), one finds that the effective potential for the Standard Model Higgs can be written as [94]

$$V(\phi, T) = D(T^2 - T_2^2)\phi^2 - ET\phi^3 + \frac{1}{4}\lambda_T \phi^4, \tag{4.2}$$

where

$$\begin{aligned} D &= \frac{1}{24}\left(6\left(\frac{m_W}{v}\right)^2 + 3\left(\frac{m_Z}{v}\right)^2 + 6\left(\frac{m_t}{v}\right)^2\right), \\ E &= \frac{1}{12\pi}\left(6\left(\frac{m_W}{v}\right)^3 + 3\left(\frac{m_Z}{v}\right)^3\right), \\ \lambda_T &= \lambda - \sum_B g_B \frac{m_B^4}{16\pi^2 v^4}\log\left(\frac{m_B^2(v)}{c_B T^2}\right) + \sum_F g_F \frac{m_F^4}{16\pi^2 v^4}\log\left(\frac{m_F^2(v)}{c_F T^2}\right), \end{aligned} \tag{4.3}$$

with $m_{W,Z,T}$ the W-boson, Z-boson and top quark masses. The Higgs mass now takes the form $m_h^2 = (2\lambda + 12B)v^2$, where B is given by

$$B = \frac{1}{64\pi^2 v^4}\left(6m_W^4 + 3m_Z^4 - 12m_t^4\right). \tag{4.4}$$

The temperature T_2 appearing in the effective potential in Eq. (4.2) reads

$$T_2^2 = \frac{m_h^2 - 8Bv^2}{4D}. \tag{4.5}$$

Thinking about the two types of phase transitions described in Section 2, one sees that the effective potential given by Eq. (4.2) has the correct form to allow for first order phase transitions. As can be seen, the ϕ^3 term is present, as in the toy model considered in the above-mentioned section. From this analysis, a weak first order phase transition is found, which would not lead to a strong gravitational wave signal. Moreover, the above result is obtained using a perturbative analysis and a high temperature expansion, which might lead to inaccuracies. For small gauge couplings lattice studies fail to reproduce the small barrier predicted with the perturbative analysis, showing that for $m_h > 80$ GeV no first order phase transition occurs in the Standard Model [95–97]. For stronger phase transitions, the perturbative results agree more closely with the lattice simulations. This is because the perturbative expansion requires small λ/g^2 for the analysis of the phase transition to be accurate, on top of small coupling λ and small gauge coupling g [1]. Since $\lambda/g^2 \sim m_h^2/m_W^2$, the requirement for the perturbative analysis to be accurate reads $m_h^2 \ll m_W^2$. As the mass of the Higgs boson is measured to be $m_h \approx 125$ GeV [6], the Standard Model Higgs potential is unable to display first order phase transitions.

Nevertheless, it is possible to achieve strong first order phase transitions by modifying the Higgs potential slightly. This will be done in the following subsection by adding a cubic term to the tree-level potential.

4.2 Modified Higgs potential

Since a first order phase transition does not occur in the Standard Model as it is, a cubic term is added to the tree-level potential of the Higgs boson. The toy model of a non-linearly realized electroweak gauge symmetry under consideration is based on [98] and computations therein will be reproduced.

The idea is to consider a different realization of the $\mathrm{SU}(2)_L \times \mathrm{U}(1)_Y$ and an alternative representation for the Higgs boson. Here, the electroweak gauge invariance is realized non-linearly by a triplet of the would-be Goldstone bosons, denoted π^i. These parameterize $\mathrm{SU}(2)_L \times \mathrm{U}(1)_Y / \mathrm{U}(1)_{\mathrm{QED}}$ [99]. The Higgs field can reside in the $\mathrm{SU}(2)_L \times \mathrm{U}(1)_Y$ singlet field ρ, since it does not have to form the electroweak doublet irreducible representation. This allows for new interactions, e.g. a cubic self-interaction for the Higgs leading to a cubic term in the tree-level potential, which may cause the electroweak phase transition to be strongly first order. In this case, the standard Higgs doublet can be formed as

$$H(x) = \frac{\rho(x)}{\sqrt{2}} e^{\frac{i}{2}\pi^i(x)T^i} \begin{pmatrix} 0 \\ 1 \end{pmatrix}, \qquad i \in \{1,2,3\}, \tag{4.6}$$

where the three would-be Goldstone bosons are denoted by the π^i fields, $T^i = \sigma^i - \delta^{i3}\mathbb{1}$ are the three broken generators and σ^i the Pauli matrices. The physical Higgs field corresponds to the fluctuation of ρ around the electroweak vacuum expectation value $v = 246$ GeV, i.e. $\rho = v + h$. The tree-level potential, including the extra cubic term, now reads

$$V^{(0)}(\rho) = -\frac{\mu^2}{2}\rho^2 + \frac{\kappa}{3}\rho^3 + \frac{\lambda}{4}\rho^4. \tag{4.7}$$

This potential depends on three different parameters, namely μ, κ and λ. Nevertheless, this dependence can be boiled down to only one parameter by using

$$\left.\frac{dV}{d\rho}\right|_{\rho=v} = 0 \qquad \text{and} \qquad \left.\frac{d^2V}{d\rho^2}\right|_{\rho=v} = m_h^2 \approx (125\mathrm{GeV})^2, \tag{4.8}$$

yielding

$$\mu^2 = \frac{1}{2}(m_h^2 + v\kappa) \qquad \text{and} \qquad \lambda = \frac{1}{2v^2}(m_h^2 - v\kappa). \tag{4.9}$$

In other words, the only free parameter of the model is chosen to be κ. One can then explore various values of κ, as was done in the original paper. However, as the main purpose of this section is to get acquainted with the various methods that pertain to the analysis, rather than the model itself, only one value of κ is chosen. The case $\kappa = -1.82 m_h^2/v$ is used to illustrate the various steps of the analysis of the phase transition.
The tree-level potential is displayed in Fig. 14. Note that a barrier is already present at tree-level. This is because of the presence of the added cubic term. Indeed, for small field values, the ρ^2 term dominates. For increasing values, the negative ρ^3 term becomes larger, causing the potential to go down. For even larger values the potential rises again because of the positive ρ^4 contribution. This barrier is exactly what is needed for a first

order phase transition.

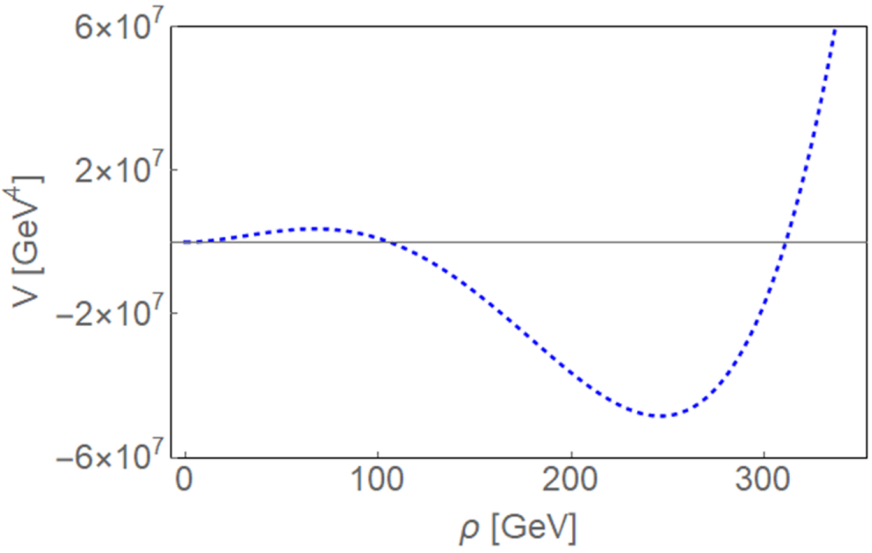

Figure 14: Tree-level potential for $\kappa = -1.82 m_h^2/v$. Due to the added cubic term, the potential already displays a barrier at tree-level.

On top of the tree-level potential, the one-loop and thermal contributions are added. The renormalization scheme where the vacuum expectation value and the tree-level mass are not altered by the one-loop contribution will be used. To this end, Eq. (2.14) is used, as the masses of the particles entering the sum are at most quadratic in the field ρ. This sum ranges over the following particles: W- and Z-boson, top quark and Higgs boson itself. The thermal contribution is added as well, where the Daisy corrections are also taken into account. These are displayed in the appendix of [98]. After adding these corrections to the tree-level potential, the bounce action can be computed. For every temperature in a certain range, the bounce trajectory associated to the effective potential under consideration is calculated. This is done by using the under/overshooting method outlined in Section 2. Once the bounce trajectory is computed, the bounce action can be determined. The result is displayed in Fig. 15. Both S_4 and S_3/T are plotted, to illustrate what was mentioned in Section 2. As can be seen, both actions can coexist, but S_3/T will quickly be lower than S_4. Because of this, the former will dominate in the decay rate.
The following step is to determine the nucleation temperature. This can be done by using the approximation discussed towards the end of Section 2 and finding the temperature where $S_3(T)/T \simeq 145$. Doing this yields a value $T_\star = 81.8$ GeV. The last thing that remains to be done consists of computing the gravitational wave spectrum associated with this phase transition. To this end, α and $\beta/H_\star$ need to be calculated.

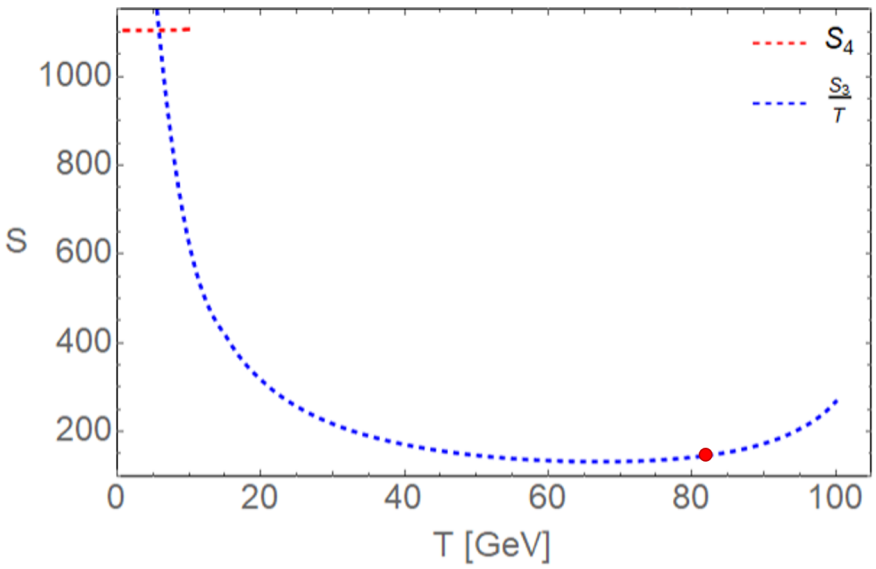

Figure 15: Temperature dependence of the bounce action for $\kappa = -1.82 m_h^2/v$. Both S_4 (red) and S_3/T (blue) are plotted. The red dot denotes the nucleation temperature $T_\star$.

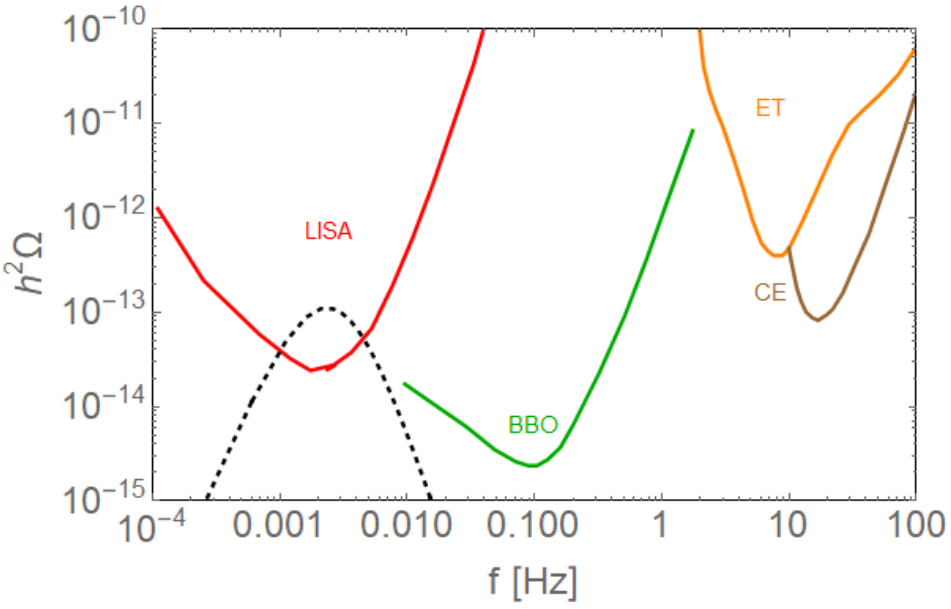

Figure 16: *Dashed*: Gravitational wave spectrum associated with the phase transition for $\kappa = -1.82 m_h^2/v$ and parameter values $\alpha = 0.046$, $\beta/H_\star = 146$ and $T_\star = 81.8$ GeV. *Solid*: sensitivity curves of different experiments, including LISA [22], BBO [58], the Einstein Telescope (ET) [100] and Cosmic Explorer (CE) [101].

Evaluating Eq. (2.46) and (2.47) yields $\alpha = 0.046$ and $\beta/H_\star = 146$. These values can then be plugged into Eq. (2.52), (2.56) and (2.60), giving the total gravitational wave spectrum. However, this spectrum is dominated by the sound wave contribution, such that only this contribution is plotted in Fig. 16. As can be seen, this signal falls in the range of the future LISA detector. From Section 2 it was to be expected that the spectrum would be in the lower frequency range. Indeed, there it was seen that lower scales result in spectra shifted towards lower frequencies. This is the case for the current nucleation temperature $T_\star$, which is of the order of the electroweak scale, i.e. $\mathcal{O}(100\text{ GeV})$.z

By having computed the effective potential, the bounce action, α, $\beta/H_\star$ and $T_\star$, this toy model constitutes the perfect practice for the models under consideration in the next section. Indeed, although the potential might look different depending on the model, the steps that need to be taken to get the gravitational wave spectrum remain identical. In what follows, different realizations of axion models are explored, together with their gravitational wave spectra.

5 $\cancel{\text{U(1)}}_{PQ}$: KSVZ model and its extensions

With the concepts of phase transitions and gravitational waves associated to them in the back of our mind, it is time to come back to where Section 3 was ended: the axion solution to the Strong CP problem. In what follows, original work on axion models will be discussed. A detailed study of the various models will provide a better understanding of whether a first order phase transition associated with the breaking of the Peccei-Quinn symmetry can occur. Furthermore, it will be examined whether a detectable gravitational wave spectrum can be generated from this transition. To be observable, the amplitude should be high enough and the frequency low enough for the terrestrial detectors at a minimum. However, the supernova constraint, which was discussed in Section 3, limits f_a from below and therefore favors higher $T_\star$ and gravitational wave frequencies. We will see whether parameter points can be found returning suitable peak frequencies, while remaining consistent with the supernova constraint. The analysis of the various models in this section constitutes original work. Similar types of models together with the investigation of a gravitational wave signal have only been covered in [9–11].Reference [11] studies the Peccei-Quinn phase transition for cases where supercooling occurs. Supercooling implies that the bubble collision takes place in the vacuum and increases the phase transition duration, causing the gravitational wave signal to be enhanced. In [10], the focus lies on the DFSZ axion model. It is shown that for a range of parameter values the associated gravitational wave signal can be detected by LIGO and the Einstein Telescope. Finally, in [9], axion-like particles, i.e. not addressing the Strong CP problem, are studied together with the possible generation of a stochastic background from first order phase transitions.

5.1 Minimal KSVZ model

The minimal KSVZ model was introduced in Section 3 as the Standard Model together with an extra fermion Q and a scalar Φ of which the axion is the phase. The Lagrangian for this model reads

$$\mathcal{L} = |\partial\Phi|^2 + \bar{Q}i\not{D}Q + y\Phi\bar{Q}Q + \text{h.c.} - V\left(|\Phi|^2\right), \tag{5.1}$$

where the potential V for the complex Peccei-Quinn scalar Φ, takes the form

$$V(\Phi) = -m^2|\Phi|^2 + \lambda|\Phi|^4. \tag{5.2}$$

One recalls that after symmetry-breaking, the Peccei-Quinn scalar Φ can be parameterized as

$$\Phi = \frac{\rho}{\sqrt{2}}e^{ia/f_a}, \tag{5.3}$$

where ρ is the radial mode, a is the Goldstone boson associated with the breaking of the $\mathrm{U}(1)_{PQ}$. Using this parameterization, the tree-level potential takes the form:

$$V_0(\rho) = -\frac{m^2}{2}\rho^2 + \frac{\lambda}{4}\rho^4, \tag{5.4}$$

where $m^2 = \lambda f_a^2$.

Being one of the simplest realizations of the axion, we begin with it in the exploration of gravitational waves in the context of the Peccei-Quinn phase transition. However, it is important to note the following about the thermal contributions in this model. By looking at the high temperature expansion of the thermal contribution in Eq. (2.15), one sees that, in Eq. (2.17), $J_B \sim \rho^3$, because the mass of the scalar scales as $m^2 \sim \rho^2$. The mass squared of the fermion, $m_Q^2 = \frac{y^2}{2}\rho^2$, displays the same ρ^2 dependence, but no ρ^3 is contained in the high-temperature expansion of the fermionic contribution. Recalling the toy model describing first order phase transitions in Eq. (2.23), one realizes that these ρ^3 contributions are precisely the ones giving rise to a barrier, and thus, a first order phase transition. After exploring the parameter space for this model, no barrier was found and thus, no gravitational wave signal. This is not surprising because of the lack of a ρ^3 term from the fermionic corrections. The effect of $J_B \sim \rho^3$ from the single scalar degree of freedom and its self coupling is negligible compared to the fermionic corrections. The scalar self-coupling is anyway known to not lead to a strong first order phase transition in the parameter regime in which the perturbative expansion is under control [1].

5.2 Extension of the minimal KSVZ model

As the regular KSVZ model with only one fermion did not yield first order phase transitions, a logical extension is to add another fermion, with the objective that this would allow for a first order phase transition and a gravitational wave signal. Adding a fermion

would allow for a more complicated mass dependence on ρ (one would now be dealing with a 2×2 mass matrix). Furthermore, it is possible that along the field ρ, one could go from a region where the high-temperature expansion holds to one where it does not, yielding more complicated expressions than Eq. (2.16). This might allow for a barrier to form because of the thermal contributions. Indeed, non-linear mass dependencies on ρ have previously been shown to be able to generate a thermal barrier [102–104]. In that case, the high-temperature expansion $J_F \sim \frac{m^2}{T^2}$ can have a cubic dependence on ρ, leading to a barrier.

In this model, the Lagrangian retains the form of Eq. (3.54), but the coupling to the fermions now changes to:

$$\mathcal{L} \supset y_Q \Phi Q \bar{Q} + m'(\bar{Q}' Q' + Q \bar{Q}') + y_{Q'} \Phi Q' \bar{Q}, \tag{5.5}$$

where Φ is the Peccei-Quinn scalar and Q and Q' are the fermions[2]. Equivalently, this can be written as

$$\mathcal{L} \supset \begin{pmatrix} \bar{Q} & \bar{Q}' \end{pmatrix} M \begin{pmatrix} Q \\ Q' \end{pmatrix}, \tag{5.6}$$

where the mass matrix M now reads:

$$M = \begin{pmatrix} y_Q \Phi & y_{Q'} \Phi \\ m' & m' \end{pmatrix}. \tag{5.7}$$

The Yukawa couplings are parameterized in the following way:

$$y_Q = y \cos\theta \qquad \text{and} \qquad y_{Q'} = y \sin\theta \tag{5.8}$$

Diagonalizing $M^\dagger M$ then yields the square of the mass eigenstates of the fermions [64].

The different charges of the particles in this extension of the minimal KSVZ model are summarized in Table 1. As a pair of vector-like fermions is added to the minimal KSVZ model, i.e. Q' and $\bar{Q}'$, these do not contribute to the anomaly of $U(1)_{PQ}$ under QCD. Thus, the anomaly is only given by the $Q\bar{Q}$ and is 1 as in the minimal KSVZ model.

	Q	$\bar{Q}$	Q'	$\bar{Q}'$	Φ
$U(1)_{PQ}$	$-\frac{1}{2}$	$-\frac{1}{2}$	$-\frac{1}{2}$	$\frac{1}{2}$	1
$SU(3)$	3	$\bar{3}$	3	$\bar{3}$	1

Table 1: $U(1)_{PQ}$ and $SU(3)$ charges associated with the various fields.

As in the KSVZ model, the tree-level potential of the Peccei-Quinn scalar Φ is given by

[2]Note that the two masses m' are chosen to be equal for simplicity, but could be chosen differently.

Eq. (5.2). As previously seen, after symmetry-breaking, this scalar can be parametrized as

$$\Phi = \frac{\rho}{\sqrt{2}} e^{ia/f_a}, \tag{5.9}$$

where ρ is the radial mode and a is the Goldstone boson associated with the breaking of the $U(1)_{PQ}$, namely the axion. Thus, the tree-level potential retains the form:

$$V_0(\rho) = -\frac{m^2}{2}\rho^2 + \frac{\lambda}{4}\rho^4, \tag{5.10}$$

where $m^2 = \lambda f_a^2$. Furthermore, the mass eigenvalues can now be computed. As an example, these are given as a function of ρ for a specific parameter choice, namely $y = 1.1$, $m' = 30$ and $\theta = \frac{7\pi}{8}$, in Fig. 17. For the moment, only the ratio of the dimensionful parameters is relevant, which is why units are not specified.

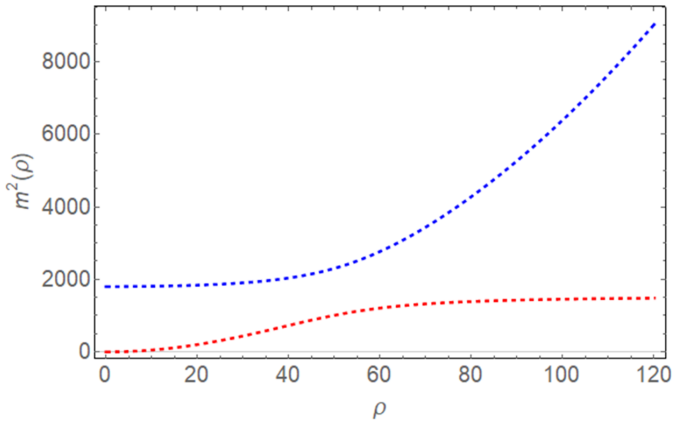

Figure 17: Mass eigenvalues for $y = 1.1$, $m' = 30$ and $\theta = \frac{7\pi}{8}$, where the units have not been specified as only dimensionless ratios of the various parameters matter for now.

On top of the tree-level potential, the effective potential will contain the one-loop and thermal contributions, where the thermal contribution is given by Eq. (2.15) and runs over the two fermions and the scalar. The one-loop correction will be discussed in the remainder of this subsection.

In Section 2, a renormalization scheme was introduced where the quantum contributions did not affect the vacuum expectation value and the mass. This led to Eq. (2.14). However, the validity of this expression is limited to cases where the various masses are of the form $m^2(\rho) = m_0^2 + \lambda\rho^2$. One notices that the mass eigenvalues of Eq. (5.7) will not be of this form. In general, one should start from the $\overline{\text{MS}}$ renormalization scheme given by Eq. (2.11) and impose the conditions such that the quantum contributions do not alter the tree-level vacuum expectation value and the tree-level mass. By doing so, one would find a general formula that differs from Eq. (2.14). In simple cases, where

the mass dependence is quadratic in the field, one recovers Eq. (2.14) [105]. This computation is outlined in Appendix A. However, in the present case, the formula is more complicated. After the correct implementation of the one-loop contribution, thermal effects are investigated. Although the eigenvalues of the mass matrix present a non-trivial dependence on the scalar field, the phase transition still turns out to be second order. The absence of a barrier can be attributed to the fact that the mass eigenvalues only increase. Indeed, from Fig. 17, it can be seen that the first eigenvalue m_1 increases for small field values, after which m_2 takes over for larger field values. From the point of view of the thermal correction, it seems like there is only a single mass increasing and thus, there is no barrier. A mass eigenvalue that increases for small field values and then returns to zero at larger field values would be able to thermally generate a barrier. This can be seen from the leading order term in the high-temperature expansion of the thermal contribution, which scales as m^2/T^2.
The above arguments lead us to conclude that this simple extension of the minimal KSVZ model does not succeed in generating first order phase transitions, and thus, no gravitational wave signal associated with this phase transition.

This simple extension of the KSVZ model fails in displaying first order phase transitions. Nevertheless, it is not excluded that making the mass matrix more complicated, and thus, the eigenvalues, would generate a barrier. As an example, three fermions could have been considered as an extension of the minimal KSVZ model. In that case, a 3×3 mass matrix would have been obtained. However, this model was not considered here due to the large amount of free parameters.

5.3 KSVZ model with dimension 6 operator

As a first order phase transition could not be achieved in the previous two models, a new strategy is adopted. The minimal KSVZ model, i.e. with one scalar and only one fermion added to the Standard Model, will be considered again. However, the tree-level potential of the scalar will now include a dimension 6 operator. Such higher-dimensional operators can be achieved in the context of effective field theory (EFT). For example, this operator $\left(HH^\dagger\right)^3$ for the Higgs boson in the SM can be realized by adding an extra scalar doublet, whose mass is much larger than the Higgs vev, i.e. $m^2 \gg v^2$ [106]. For a more detailed explanation, see Appendix C.
The modification to the electroweak phase transition induced by the presence of a dimension 6 operator has been extensively studied in [39, 107]. There it was found that the addition of such a term allows for first order phase transitions, which would generate a gravitational wave signal detectable by LISA or BBO, another second-generation space-based laser interferometer [108]. Here, the same idea is applied for the first time to the study of the PQ phase transition with a dimension 6 operator.

Armed with the fact that such dimension 6 operators can arise in the potential, one

writes the tree-level potential of the complex Peccei-Quinn scalar Φ as

$$V(\Phi) = m^2|\Phi|^2 + \lambda|\Phi|^4 + \frac{1}{\Lambda^2}|\Phi|^6, \tag{5.11}$$

where Λ is the high-energy cut-off scale of the EFT. This is the scale at which the new physics responsible for the dimension 6 operator starts to become relevant. The EFT is valid as long as the vacuum expectation value of the scalar and its mass are smaller than this scale Λ. After the breaking of the Peccei-Quinn symmetry, the field Φ is parameterized as

$$\Phi = \frac{\rho}{\sqrt{2}} e^{ia/f_a}, \tag{5.12}$$

where the axion field is represented by a and ρ is the radial mode. The tree-level potential now reads

$$V(\rho) = \frac{m^2}{2}\rho^2 + \frac{\lambda}{4}\rho^4 + \frac{1}{8\Lambda^2}\rho^6. \tag{5.13}$$

The mass of the scalar and the fermion are respectively given by

$$m_\rho^2(\rho) = m^2 + 3\lambda\rho^2 + \frac{15}{4\Lambda^2}\rho^4 \qquad \text{and} \qquad m_f^2(\rho) = \frac{y^2}{2}\rho^2, \tag{5.14}$$

where y is the Yukawa coupling of the fermion. The free parameters of the model are m, λ, Λ, y and μ which enters in the $\overline{\text{MS}}$ renormalization scheme, which will be used for the one-loop contribution (see Eq. (2.11)). Furthermore, a comment needs to be made about the thermal contributions. From Section 2, one recalls that the potential also receives other contributions on top of the thermal potential, namely the so-called Daisy corrections. These were introduced to deal with the IR divergences. Since only bosons need such corrections, this will only have to be taken into account for the scalar. These corrections could be parametrized by a shift in the mass term in the thermal potential, which in this case is given by

$$m_\rho^2 \to m_\rho^2 + \frac{T^2}{2f_a^2}m_f^2 - \frac{3T^2}{4}\frac{f_a^2}{\Lambda^2}, \tag{5.15}$$

where f_a is the vacuum expectation value of the field ρ [39]. However, as these contributions constitute only very small corrections, these were not included in the various scans that will be displayed later in this section. Nevertheless, to show the tiny effect of including these contributions, they will be included when considering some benchmark points for comparison.

Remark on units

Before exploring the parameter space, a note is made on the choice of units. It is found that the shape of the potential does not depend on the choice of units, but rather on the dimensionless ratio of the mass scales of the problem. This is the reason why dimensionful parameters will be parameterized with pure numbers in the following, having in mind that the appropriate mass unit will be reinstated afterwards. The first instance

a scale needs to be specified, is during the computation of the nucleation temperature $T_\star$. Indeed, one recalls from Section 2 that the Planck mass appears in the nucleation condition given by Eq. (2.43), requiring the specification of a scale.
One remembers from Section 3 that several constraints exist on the axion parameter space. The most important one for the KSVZ-type models comes from supernovae and reads: $f_a \gtrsim 2 \times 10^8$ GeV [93]. Thus, when specifying the units, one needs to make sure that the vacuum expectation value satisfies this condition. At the same time, one wants to have the scale of the temperature as low as possible to be within reach of the sensitivity of the gravitational wave detectors. Indeed, the position of the peak of the gravitational spectrum is partly determined by the nucleation temperature $T_\star$, favoring lower scales (see Fig. 10).
Various scales will be considered when studying different benchmark points. The units of the dimensionful parameters will be chosen such that $f_a = 10^8$ GeV, $f_a \sim 2 \times 10^8$ GeV and $f_a = 10^9$ GeV. This corresponds to a case where one is outside the allowed region coming from axion constraints, one right at the border and one well inside the allowed region. The various computations will be described in detail only for one of the scales above, whereas the others will simply be summarized. For instance, to give an example, the scale under consideration for the detailed studies will be $f_a \sim 2 \times 10^8$ GeV. To this end, the units are set to 4.08×10^6 GeV. For example, if a dimensionless temperature T_1 is quoted, the physical temperature would then correspond to $T_1 \times 4.08 \times 10^6$ GeV. Similarly, this applies to all other dimensionful parameters.

5.3.1 Analysis of the phase transition

In the previous subsection, a new model was introduced consisting of the minimal KSVZ model supplemented with a dimension 6 operator. The aim of this subsection is to explore the parameter space of this model and analyze the phase transition, together with the generation of a gravitational wave signal.

It is important to already note that this model exhibits a barrier, whereas the previous models that were considered failed in exactly this aspect. As an example, $m = 2, \lambda = -0.25$ and $\Lambda = 100$ were chosen to illustrate the presence of such a barrier, even at tree-level. For the dimensionful parameters m and Λ, only the ratio is important for the moment as mentioned above, which is why units are not specified. The tree-level potential is displayed in Fig. 18. This tree-level barrier will then be enhanced due to the thermal contributions. Therefore, the KSVZ fermion can still play a crucial role in obtaining a strong first order phase transition. This is because the thermal fermionic contribution to the potential, scaling as $\sim y^2 \rho^2 T^2$, together with the tree-level $-\lambda \rho^4$ can combine to form a large barrier far in excess of the tree-level one.

One can now start exploring the parameter space and computing the values of the parameters needed for the gravitational wave signal. Various scans will be performed, which will display the values of α, $\beta/H_\star$ and the nucleation temperature $T_\star$. The specifics of how these quantities are computed will be addressed by considering various benchmark

points later in this section. However, this will be very similar to the computation done in Section 4.

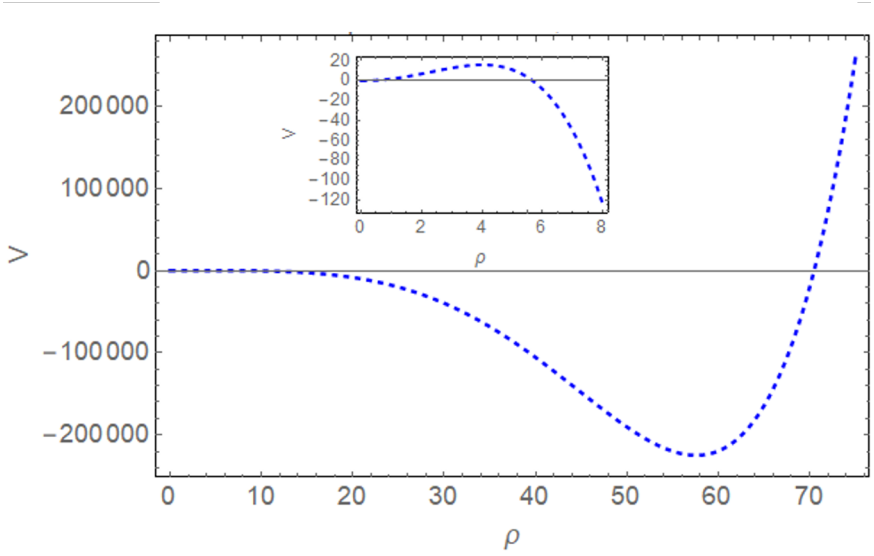

Figure 18: Tree-level potential for $m = 2, \lambda = -0.25$ and $\Lambda = 100$, where units have not been specified as only the dimensionless ratio is important for now. As can be seen, a tree-level barrier is present for this choice of parameters.

Scan over the parameter space

A scan over different values of m and λ is considered first. This entails that the other parameters are kept fixed during the computation: $y = 1.05$ and $\Lambda = \mu = 100$.[3] The results are shown in Fig. 19. At first glance, one notices that α and $\beta/H_\star$ are correlated, as previously mentioned. Indeed, as α increases, $\beta/H_\star$ and the nucleation temperature $T_\star$ decrease.

Furthermore, one also notices that the value of α increases (or that $\beta/H_\star$ decreases) as one gets closer to the region where no nucleation occurs. The highest values for α, which are the interesting ones from a gravitational wave point of view, can be found for the lower parameter values in this scan, close to the no-nucleation region. This can be understood by considering the expression for $\beta/H_\star$, given by Eq. (2.47), and realizing that the nucleation condition, Eq. (2.43), can be approximated by simply asking that the bounce action equals a constant, depending on the scale (this was shown for the SM and the electroweak scale in Section 2). Analogously, one can write this down for typical scales involved in the Peccei-Quinn phase transition. Starting from

$$\frac{S_3(T_\star)}{T_\star} \approx 4 \log \frac{T_\star}{H(T_\star)}, \tag{5.16}$$

[3]The renormalization scale μ is chosen always equal to the EFT scale Λ for concreteness. It was checked that the results do not change qualitatively by varying it.

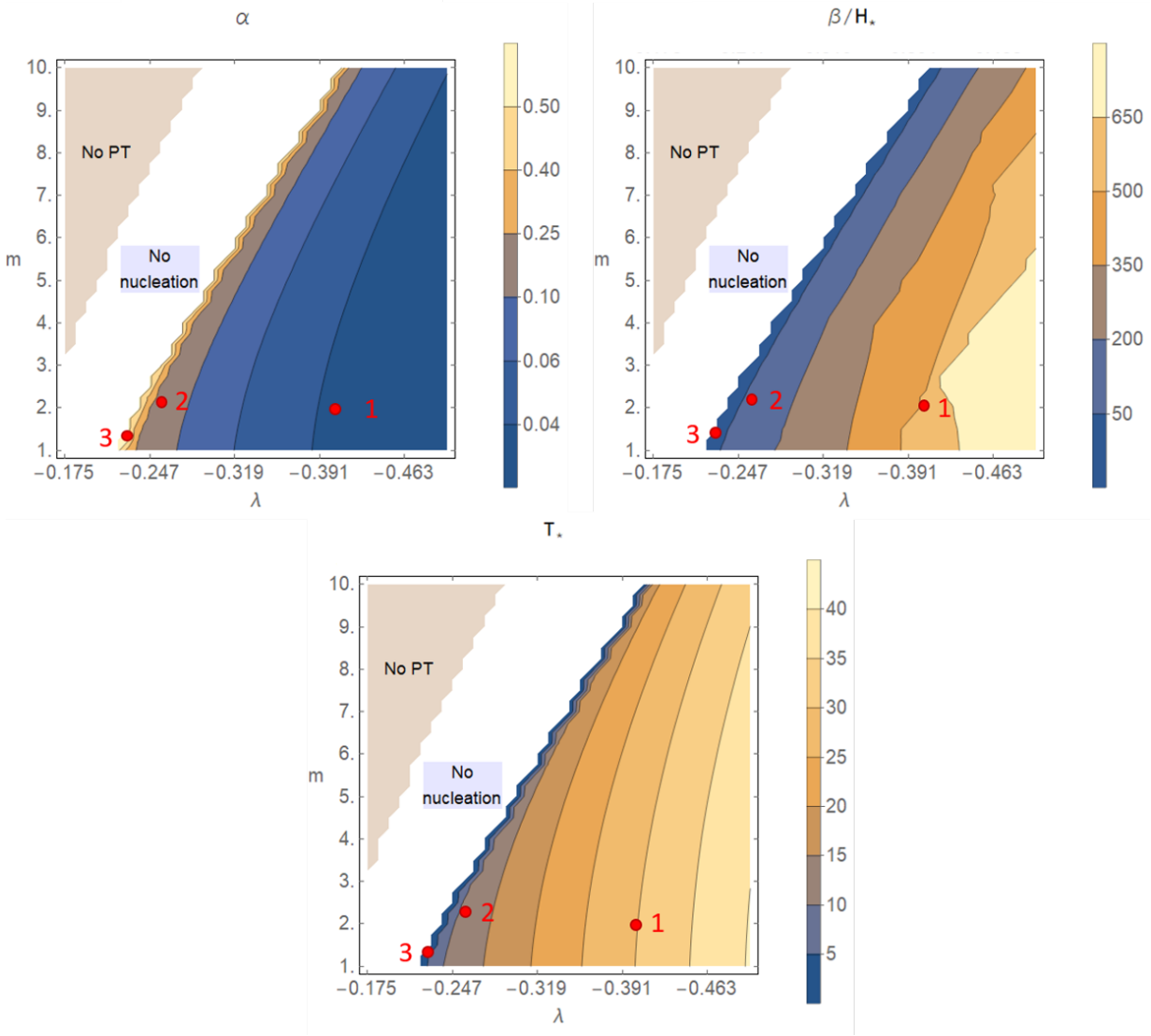

Figure 19: α, $\beta/H_\star$ and $T_\star$ for different values of λ and m, with $y = 1.05$ and $\Lambda = \mu = 100$. The appropriate units for the dimensionful parameters can be restored by multiplying by 4.08×10^6 GeV.

one can use $T_\star = \mathcal{O}(10^8)$ GeV and $g_\star = 106.75 + 12\frac{7}{8} + 2$, coming from the SM content, the fermionic contribution and the complex scalar. Filling in the value of the Planck mass $M_p = 2.435 \times 10^{18}$ GeV, one finds that $H(T_\star) = \mathcal{O}(10^{-2})$ GeV, such that $S_3(T_\star)/T_\star \approx 90$. This is illustrated in Fig. 20 by the black line. Concretely, this means that nucleation happens when the bounce action intersects the black line. As $\beta/H_\star$ is partly determined by the derivative of the bounce action, it will be large for the blue line, because the bounce action is fairly steep around the intersection with the black line. On the other

hand, on the border of the no-nucleation zone, e.g. the red line, the bounce action will barely touch the black line. Its derivative will be small, as the bounce action is almost flat there, yielding a small $\beta/H_\star$. This illustrates why $\beta/H_\star$ is smaller closer to the no-nucleation zone in the above scans.

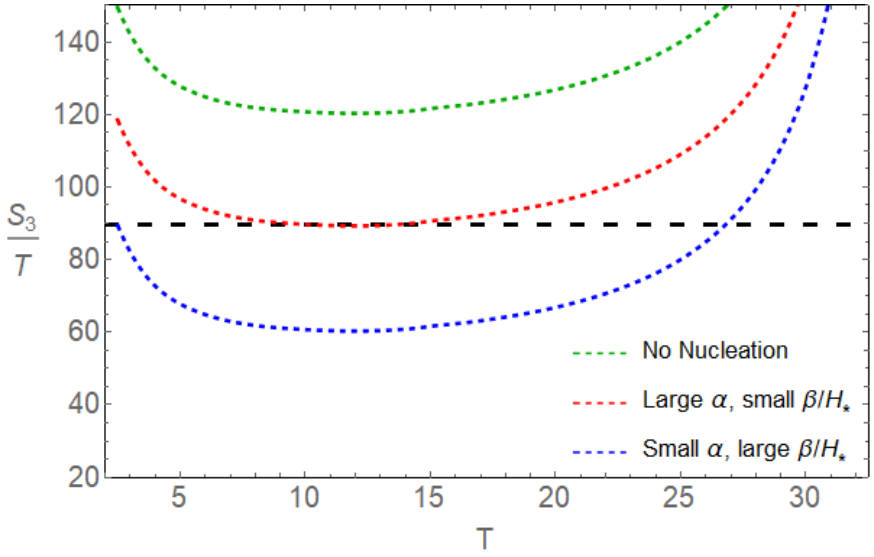

Figure 20: Various bounce actions as an illustration of why α is larger and $\beta/H_\star$ smaller close to the no-nucleation region. Three different cases are shown: no nucleation (green), large α and small $\beta/H_\star$ (red), and finally, small α and large $\beta/H_\star$ (blue). The appropriate units for the dimensionful parameters can be restored by multiplying by 4.08×10^6 GeV.

The next scan of the parameter space consists of varying the quartic coupling λ and the Yukawa coupling y, while keeping the other parameters fixed: $m = 2$, $\Lambda = \mu = 100$. This scan is displayed in Fig. 21. As with the previous scan, one notices that the values of α and $\beta/H_\star$ are correlated. The lowest values of α are found in the bottom right corner of the scan, i.e. for larger λ and low values of the Yukawa coupling. Once again, it is clear that the value of α increases, or $\beta/H_\star$ decreases, as one gets closer to the no nucleation zone. This happens because of the same reason that was given for the previous scan. The red dot in Fig. 21 indicates the point in this scan with highest α and lowest $\beta/H_\star$. It will be treated in more detail later on in this section.

Benchmark point analysis

The above scans give an overview of the general behavior as the various parameters of the model are varied. A few benchmark points will now be chosen from the scans in Fig. 19 and Fig. 21, to illustrate the various steps that lead to the spectrum of the gravitational wave associated with the phase transition. The benchmarks are listed in Table 2 and are given by the red dots in the above-mentioned scans. These are chosen to demonstrate how the value of α and $\beta/H_\star$ influences the gravitational wave spectrum obtained from

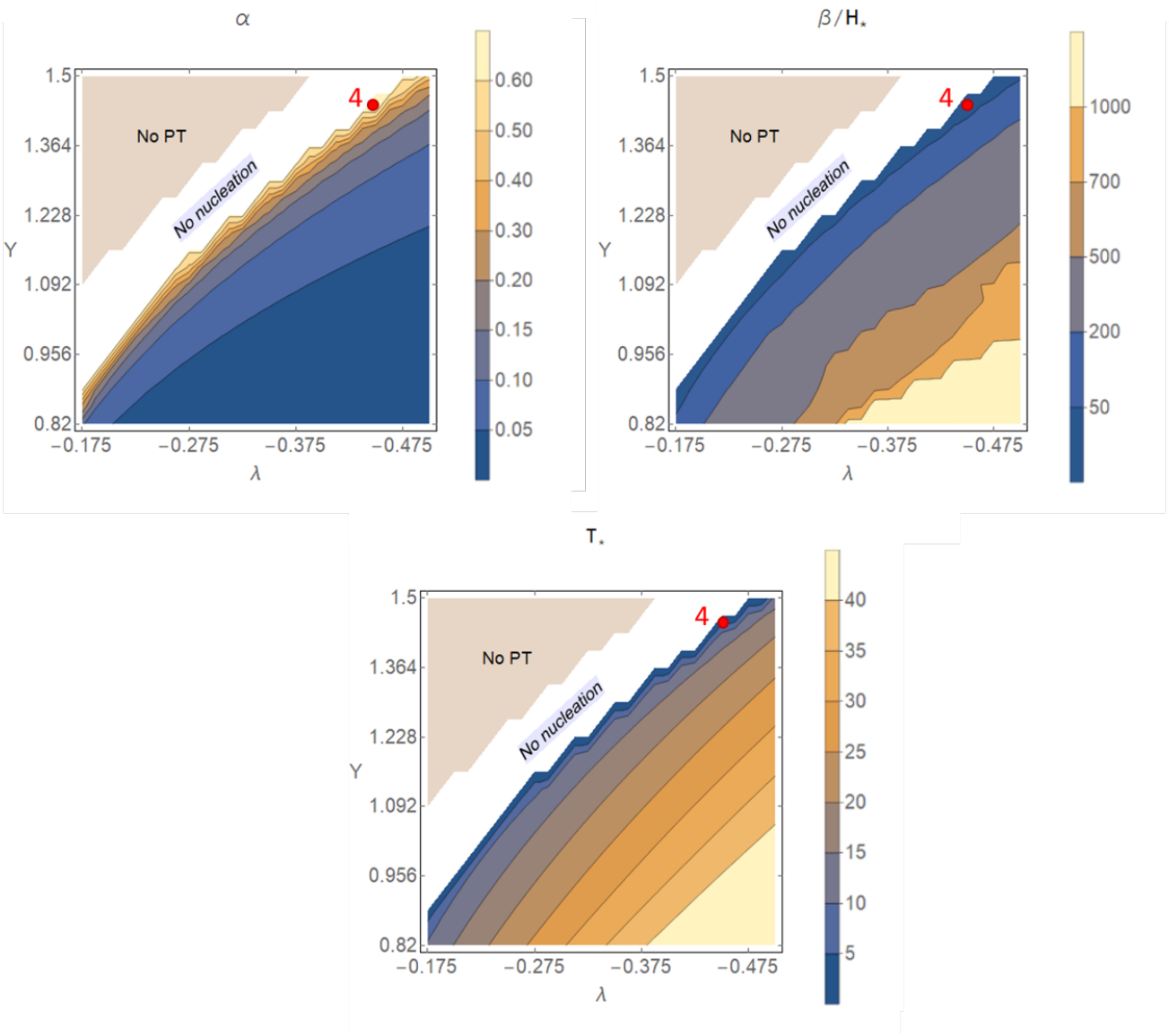

Figure 21: α and $\beta/H_\star$ for different values of λ and y, with $m = 2$ and $\Lambda = \mu = 100$. The appropriate units for the dimensionful parameters can be restored by multiplying by 4.08×10^6 GeV.

a first order phase transition. For these benchmark points, the Bodeker-Moore criterion given, by Eq. (2.64), was checked and was found to be satisfied. Because of this, the bubble wall velocity was set to $v_w = 1$ in the computation of the gravitational wave spectra for the various benchmarks.

	λ	m	y	Λ	μ
Benchmark point 1	-0.4	2	1.05	100	100
Benchmark point 2	-0.256	2.25	1.05	100	100
Benchmark point 3	-0.229	1.3	1.05	100	100
Benchmark point 4	-0.45	2	1.432	100	100

Table 2: Various benchmark points from the scans used for a more detailed analysis of the phase transition and the gravitational wave spectrum. The appropriate units will be restored when necessary.

Benchmark point 1

Consider the first benchmark point with parameter values $\lambda = -0.4$, $m = 2$, $y = 1.05$, and $\Lambda = \mu = 100$. The first step consists of determining the critical temperature T_c. This temperature is computed to be 35.58. The following step is to compute the bounce action for different temperatures below T_c. Indeed, as the true minimum only appears for temperatures below T_c, tunneling will only start below this temperature. The resulting bounce action is depicted in Fig. 22.

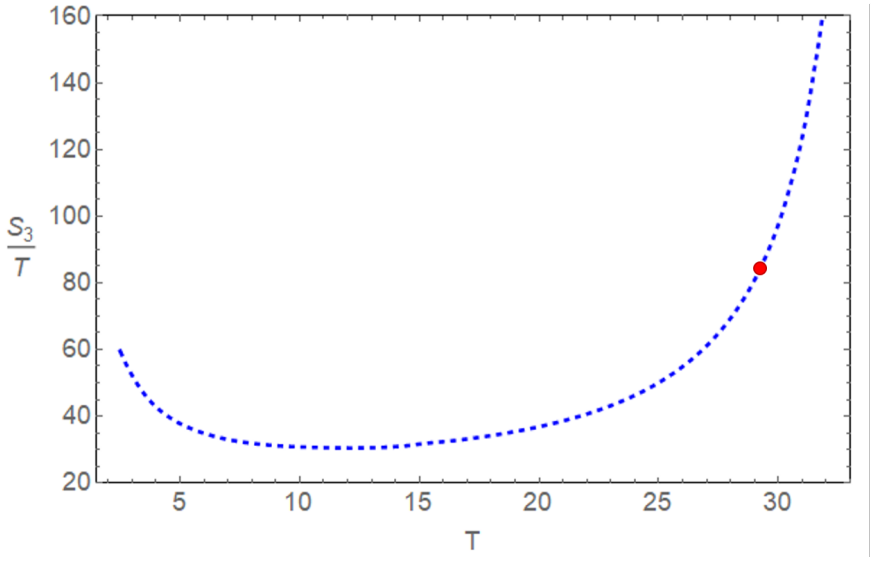

Figure 22: Bounce action for parameter values $\lambda = -0.4$, $m = 2$, $y = 1.05$, and $\Lambda = \mu = 100$. The red dot denotes the nucleation temperature $T_\star$. The appropriate units for the dimensionful parameters can be restored by multiplying by 4.08×10^6 GeV.

With the bounce action computed, the remaining task is to determine α, $\beta/H_\star$ and

$T_\star$. To find the nucleation temperature $T_\star$, Eq. (2.43) needs to be solved. Note that this is the first time that an energy scale needs to be specified in the model, whereas before the physics only depended on the dimensionless ratio of the mass scales of the problem. As mentioned previously, various scales are considered, namely $f_a = 10^8$ GeV, $f_a \sim 2 \times 10^8$ GeV and $f_a = 10^9$ GeV. However, only the scale where $f_a \sim 2 \times 10^8$ GeV will be described in detail here. The results for the other scales will be summarized at the end of the computations for each benchmark point. For this choice of parameters, a vacuum expectation value of 2.86×10^8 GeV is found, which is right at the border of the allowed region for f_a, as mentioned previously. This corresponds to choosing the units to be 4.08×10^6 GeV. Solving Eq. (2.43) yields $T_\star = 1.21 \times 10^8$ GeV. This temperature can then be used to compute α and $\beta/H_\star$ by using Eq. (2.46) and Eq. (2.47), yielding $\alpha = 0.038$ and $\beta/H_\star = 498$. For completeness, the percolation temperature T_p will be computed as well. However, it is expected that it will be comparable to the nucleation temperature $T_\star$, as $\beta/H_\star$ is fairly large. Recall from Section 2 that percolation ensures that the phase transition completes, by checking that the bubbles expand at least as fast as the expansion rate of the volume they reside in. Eq. (2.49) is computed such that $I(T_p) = 1$ holds and the temperature for which Eq. (2.50) is satisfied is determined as well. The percolation temperature T_p is then the minimum of the two, i.e. the temperature for which both conditions hold. These two conditions are illustrated in Fig. 23. The percolation temperature is determined to be $T_p = 1.16 \times 10^8$ GeV for the chosen units. As was expected, this is close to the nucleation temperature $T_\star$.

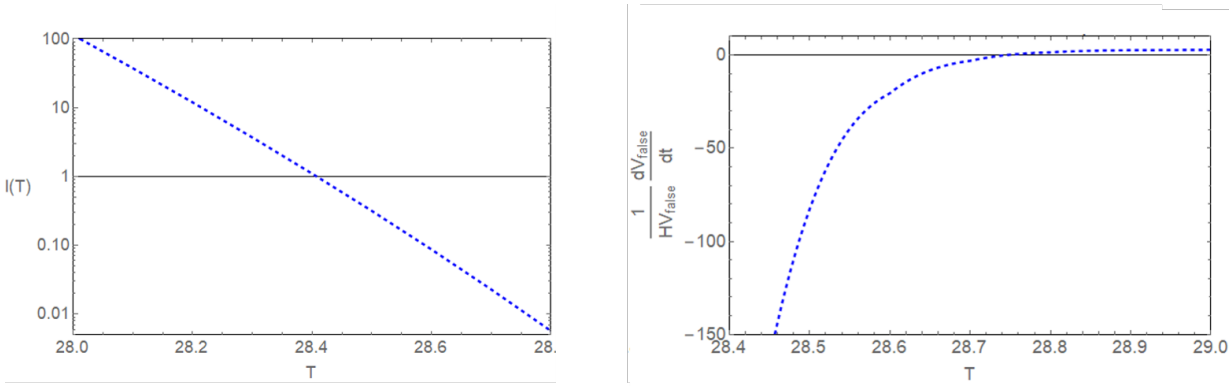

Figure 23: Conditions to obtain the percolation temperature T_p. Left: requiring that about 74% of the volume is in the true vacuum. Right: requiring that the expansion rate of the bubble is at least as fast as the one of the volume it resides in. The appropriate units for the dimensionful parameters can be restored by multiplying by 4.08×10^6 GeV.

With the parameters that were computed above, all the necessary ingredients are now available to consider the gravitational wave spectrum. In principle, this signal is made up of three contribution listed at the end of Section 2. However, the sound wave contribution will dominate, as was mentioned in Section 4. Thus, the spectrum is well approximated by taking only that contribution into account. The resulting gravitational wave signal

can be found in Fig. 24. As mentioned at the beginning of this analysis, various scales were considered. The figure also includes the signals for the other two scales. Finally, the parameters for the three different scales are summarized in Table 3.

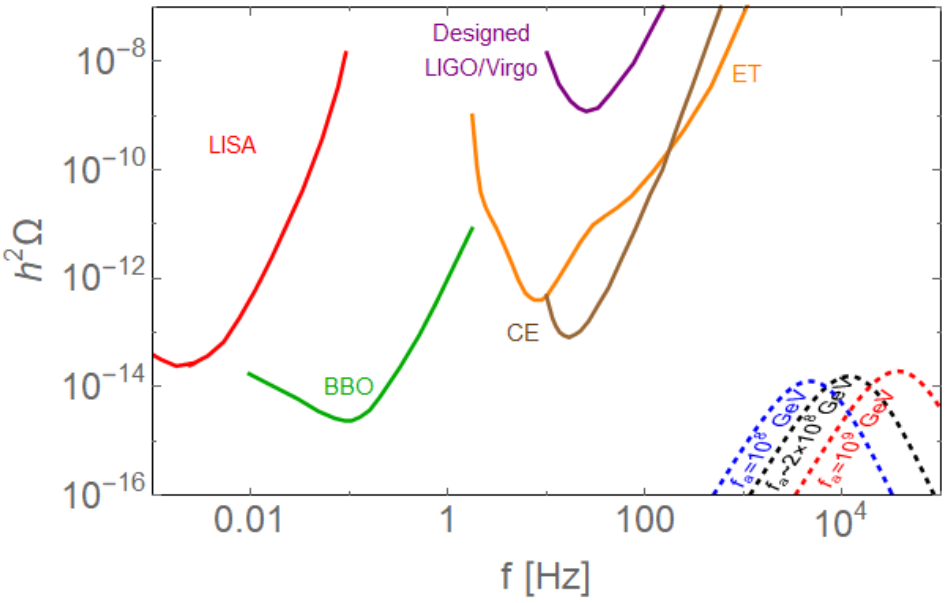

Figure 24: Gravitational wave signal from first order phase transition associated with the potential with parameters $\lambda = -0.4$, $m = 2$, $y = 1.05$, and $\Lambda = \mu = 100$. The parameters describing the phase transition are listed in Table 3 for the various scales. The appropriate units for the dimensionful parameters can be restored by multiplying by the last line in that table.

Benchmark Point 1			
f_a (10^8GeV)	1	2.86	10
α	0.037	0.038	0.039
$\beta/H_\star$	561	498	448
$T_\star$ (10^7GeV)	4.26	12.1	41.8
T_p (10^7GeV)	4.1	11.6	39.9
Units (10^6 GeV)	1.43	4.08	14.3

Table 3: Quantities pertaining to the analysis of the gravitational spectrum for various scales for the benchmark $\lambda = -0.4$, $m = 2$, $y = 1.05$, and $\Lambda = \mu = 100$. The appropriate units for the dimensionful parameters can be restored by multiplying by the last line in this table.

As was mentioned earlier, the exact analysis of these points should include the so-called Daisy corrections in Eq. (5.15). However, it was argued that the effect of adding such corrections is negligible. To illustrate this, the above computations are repeated with the Daisy correction terms included. The results are summarized in Table 4. One can see that the addition of such corrections barely affects the value of the parameters. Therefore, choosing to not include these contributions in the scans is reasonable.

Benchmark Point 1		
Daisy	No	Yes
α	0.038	0.038
$\beta/H_\star$	498	496
$T_\star$ (10^7GeV)	12.1	12.1

Table 4: Comparison with Daisy correction terms of the quantities pertaining to the analysis of the gravitational spectrum for the benchmark $\lambda = -0.4$, $m = 2$, $y = 1.05$, and $\Lambda = \mu = 100$. The appropriate units for the dimensionful parameters can be restored by multiplying by 4.08×10^6 GeV.

Benchmark point 2

The previous benchmark point illustrates how a low values of α and large $\beta/H_\star$ result in a weaker gravitational wave spectrum, escaping detection. However, the model under consideration also has larger values for α as can be seen from the scan in Fig. 19. The second benchmark point is chosen such that the values of the parameters are situated between the maximum and minimum value of each parameter. This benchmark point can be seen as an average point in the scan, neither extremely high values, nor extremely low. Concretely, the parameter point with values $\lambda = -0.256$, $m = 2.25$, $y = 1.05$, and $\Lambda = \mu = 100$ is chosen. Following the same steps as with the previous benchmark, the critical temperature T_c is determined to be $T_c = 19.7$. The computation of the bounce action (see Fig. 25) is followed by the choice of the same units as were chosen for the previous benchmark, namely 4.08×10^6 GeV.

The nucleation temperature is obtained by solving Eq. (2.43), yielding $T_\star = 4.47 \times 10^7$ GeV in the chosen units. With the nucleation temperature at hand, α and $\beta/H_\star$ are determined to be 0.187 and 72.4 respectively. Subsequently, the percolation temperature T_p is determined. Both conditions for percolation are illustrated in Fig. 26. The percolation temperature is computed to be $T_p = 3.84 \times 10^7$ GeV.

For the gravitational wave signal, only the sound wave contribution is taken into account again, as this one will dominate. The spectrum is displayed in Fig. 27, together with the spectra for the other scales. The values describing the phase transition for the

various scales are given in Table 5.

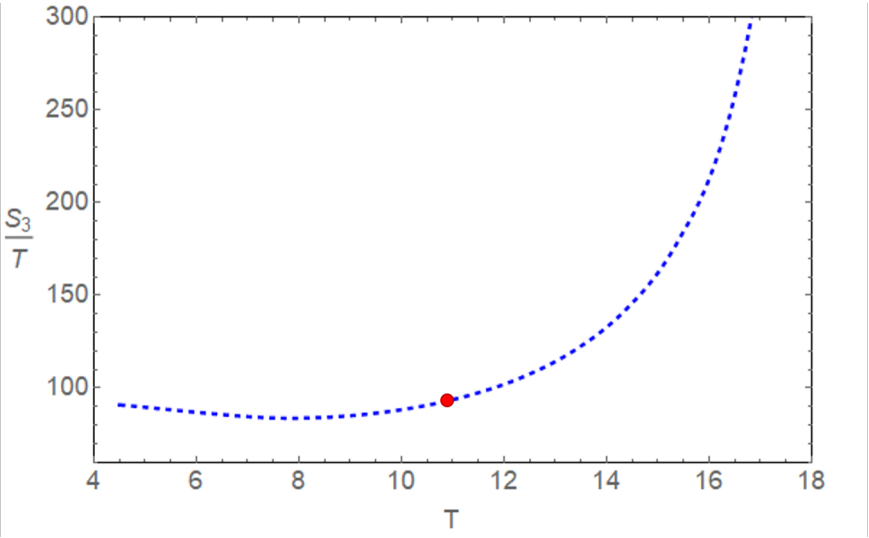

Figure 25: Bounce action for parameter values $\lambda = -0.256$, $m = 2.25$, $y = 1.05$, and $\Lambda = \mu = 100$. The red dot denotes the nucleation temperature $T_\star$. The appropriate units for the dimensionful parameters can be restored by multiplying by 4.08×10^6 GeV.

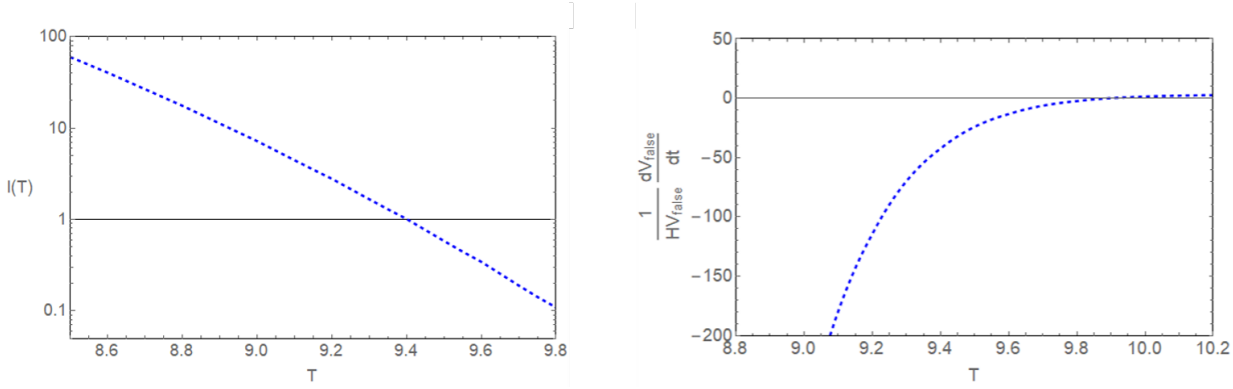

Figure 26: Conditions to obtain the percolation temperature T_p. Left: requiring that about 74% of the volume is in the true vacuum. Right: requiring that the expansion rate of the bubble is at least as fast as the one of the volume it resides in. The appropriate units for the dimensionful parameters can be restored by multiplying by 4.08×10^6 GeV.

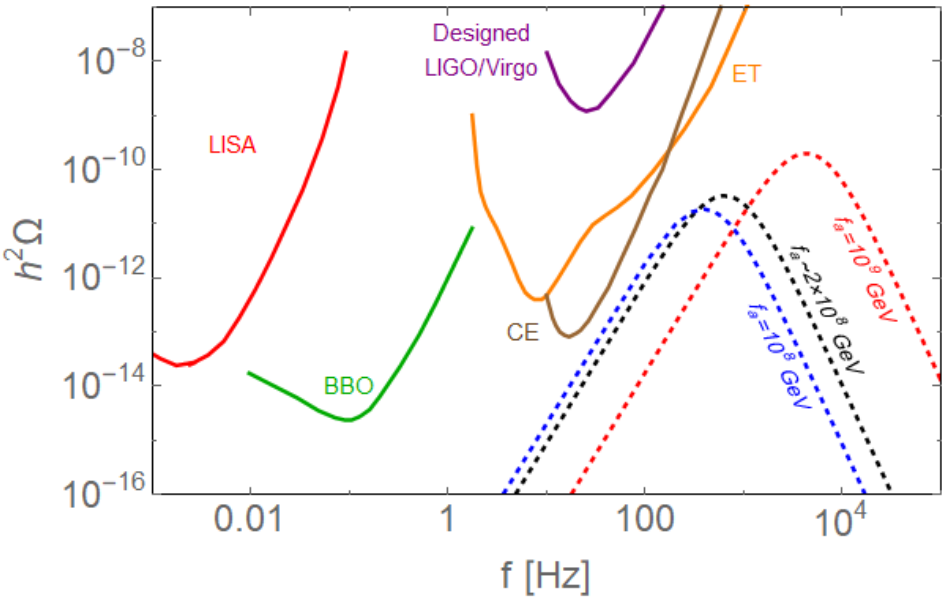

Figure 27: Gravitational wave signals from first order phase transition associated with the potential with parameters $\lambda = -0.256,\ m = 2.25,\ y = 1.05,$ and $\Lambda = \mu = 100$. The parameters describing the phase transition are listed in Table 5 for the various scales. The appropriate units for the dimensionful parameters can be restored by multiplying by the last line in that table.

Benchmark Point 2			
f_a (10^8GeV)	1	2.06	10
α	0.17	0.19	0.27
$\beta/H_\star$	88.3	72.4	37.3
$T_\star$ (10^7GeV)	2.25	4.47	19.3
T_p (10^7GeV)	1.96	3.84	16.6
Units (10^6 GeV)	1.98	4.08	19.8

Table 5: Quantities pertaining to the analysis of the gravitational spectrum for various scales for the benchmark $\lambda = -0.256,\ m = 2.25,\ y = 1.05,$ and $\Lambda = \mu = 100$. The appropriate units for the dimensionful parameters can be restored by multiplying by the last line in this table.

Benchmark point 3

In contrast with the previous benchmarks, one with large α and small $\beta/H_\star$ is now chosen. Hence, the parameter point $\lambda = -0.229,\ m = 1.35,\ y = 1.05,$ and $\Lambda = \mu = 100$ is

considered. The various steps leading to the gravitational wave spectrum are completely analogous to the steps that were followed for the previous benchmarks. The critical temperature is determined to be $T_c = 16.86$, after which the bounce action is computed. This is depicted in Fig. 28. One notices that the bounce action is a bit larger than in the previous case, which already suggests a lower $\beta/H_\star$ and thus, a larger α (see argument around Fig. 20).

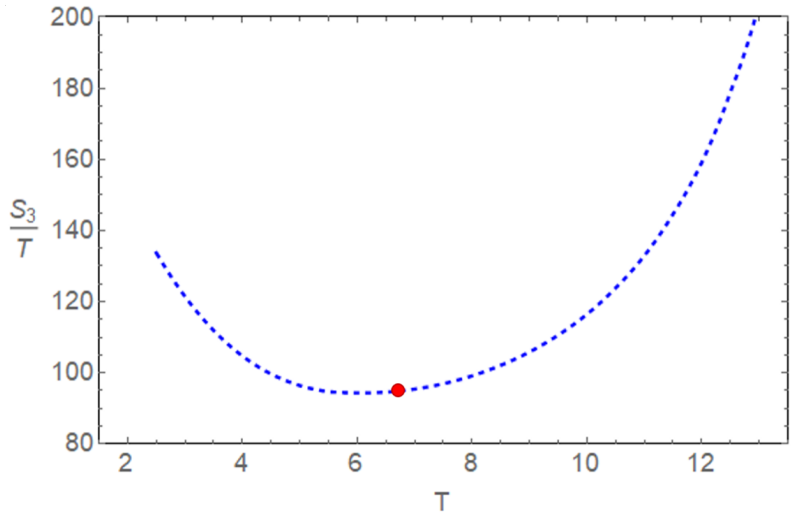

Figure 28: Bounce action for parameter values $\lambda = -0.229$, $m = 1.35$, $y = 1.05$, and $\Lambda = \mu = 100$. The red dot denotes the nucleation temperature $T_\star$. The appropriate units for the dimensionful parameters can be restored by multiplying by 4.08×10^6 GeV.

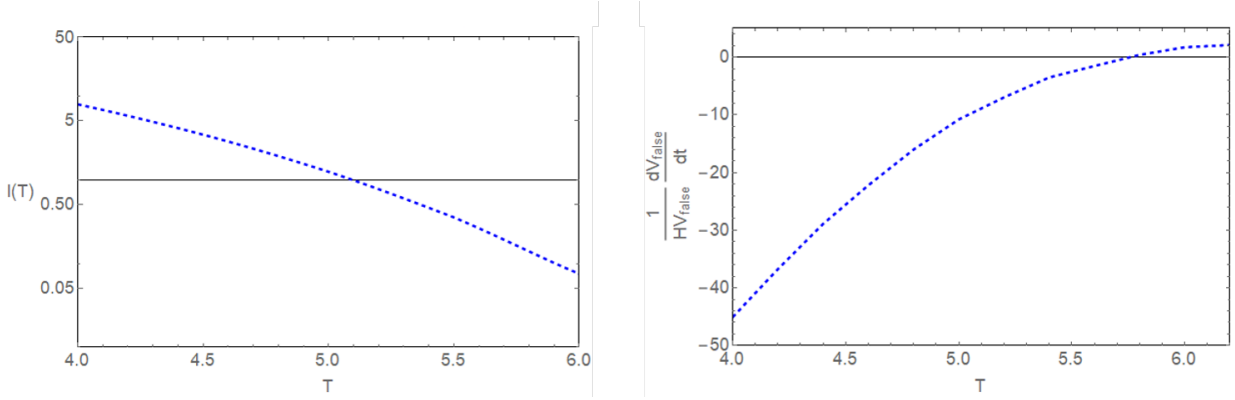

Figure 29: Conditions to obtain the percolation temperature T_p. Left: requiring that about 74% of the volume is in the true vacuum. Right: requiring that the expansion rate of the bubble is at least as fast as the one of the volume it resides in. The appropriate units for the dimensionful parameters can be restored by multiplying by 4.08×10^6 GeV.

One then proceeds to compute the nucleation temperature $T_\star$. The same units are used as for the previous benchmarks, i.e. 4.08×10^6 GeV, now yielding $f_a = 1.88 \times 10^8$ GeV for this benchmark point. After solving Eq. (2.43), one finds $T_\star = 2.73 \times 10^7$ GeV. Subsequently, α and $\beta/H_\star$ are computed, yielding $\alpha = 0.61$ and $\beta/H_\star = 10.4$. As for the previous benchmarks, the percolation temperature T_p is computed. Both conditions for percolation are illustrated in Fig. 29. Taking the minimum of the two temperatures satisfying the percolation conditions results in $T_p = 2.08 \times 10^7$ GeV expressed in the chosen units.

With the value of α, $\beta/H_\star$ and $T_\star$ at hand, the gravitational wave spectrum can be computed. Only the sound wave contribution will be taken into account, as was done with the previous benchmark points. The gravitational wave signal from the first order phase transition is displayed in Fig. 30, together with the signals obtained at other scales. The parameters are given in Table 6 for the other scales. It is important to note that in this case, no nucleation occurs at the scale where $f_a = 10^9$ GeV.

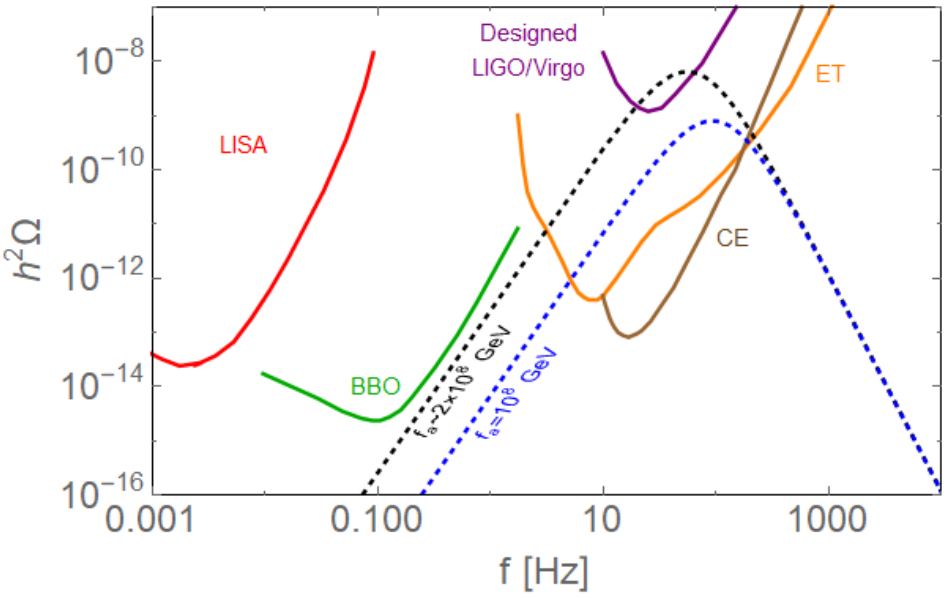

Figure 30: Gravitational wave signal from first order phase transition associated with the potential with parameters $\lambda = -0.229$, $m = 1.3$, $y = 1.05$ and $\Lambda = \mu = 100$. The parameters describing the phase transition are listed in Table 6 for the various scales. The appropriate units for the dimensionful parameters can be restored by multiplying by the last line in that table.

From Fig. 30, it is clear that higher values α and lower $\beta/H_\star$ result in a stronger signal, allowing it to be detected by LIGO-Virgo once their designed sensitivity is reached. Furthermore, these signals will also be well within reach of the future Einstein Telescope. This in contrast to the first benchmark point, where low α and large $\beta/H_\star$ resulted in es-

caping detection. It should also be noted that from Section 2, more particularly Fig. 10, one expects that a lower scale results in a spectrum shifted towards lower frequencies. However, this is not the case here. Indeed, the position of the peak of the spectrum depends on the product of $\beta/H_\star$ and $T_\star$, as given by Eq. (2.58), such that one finds that the frequency where the spectrum peaks is larger for the lower scale.

Benchmark Point 3			
f_a (10^8GeV)	1	1.88	10
α	0.40	0.61	-
$\beta/H_\star$	29.1	10.4	-
$T_\star$ (10^7GeV)	1.64	2.73	-
T_p (10^7GeV)	1.3	2.08	-
Units (10^6GeV)	2.17	4.08	21.7

Table 6: Quantities pertaining to the analysis of the gravitational spectrum for various scales for the benchmark $\lambda = -0.229,\ m = 1.3,\ y = 1.05$, and $\Lambda = \mu = 100$. The appropriate units for the dimensionful parameters can be restored by multiplying by the last line in this table.

Benchmark point 4

As a last detailed study, the parameter point with highest α and lowest $\beta/H_\star$ from Fig. 21 will be considered, i.e. the red dot in that figure. This point is given by $\lambda = -0.45,\ m = 2,\ y = 1.432$, and $\Lambda = \mu = 100$. As with the previous points, the same scales will be considered. As the computations are similar to the treatment of the previous benchmarks, only the results will be stated in Table 7 and the gravitational wave spectrum will be given in Fig. 31 for the various scales. Similarly to benchmark point 3, nucleation does not occur for $f_a \sim 10^9$ GeV for this point. Since the values of α and $\beta/H_\star$ are similar to the third benchmark point (see Table 6), the signals look fairly similar to each other. However, the nucleation temperature is slightly higher for the current point, resulting in a shift of the spectrum towards higher frequencies compared to the previous benchmark. Because of this, the point under consideration escapes detection by LIGO-Virgo. Nevertheless, it remains within reach of the sensitivity of the Einstein Telescope.

The previous benchmark points illustrate how α, $\beta/H_\star$ and $T_\star$ influence the position and amplitude of the peak of the gravitational wave spectrum. High α and low $\beta/H_\star$ are favored to achieve a higher amplitude. Lower $T_\star$ will result in the spectrum being centered around lower frequencies, increasing the chance of being within reach of the gravitational wave detectors.

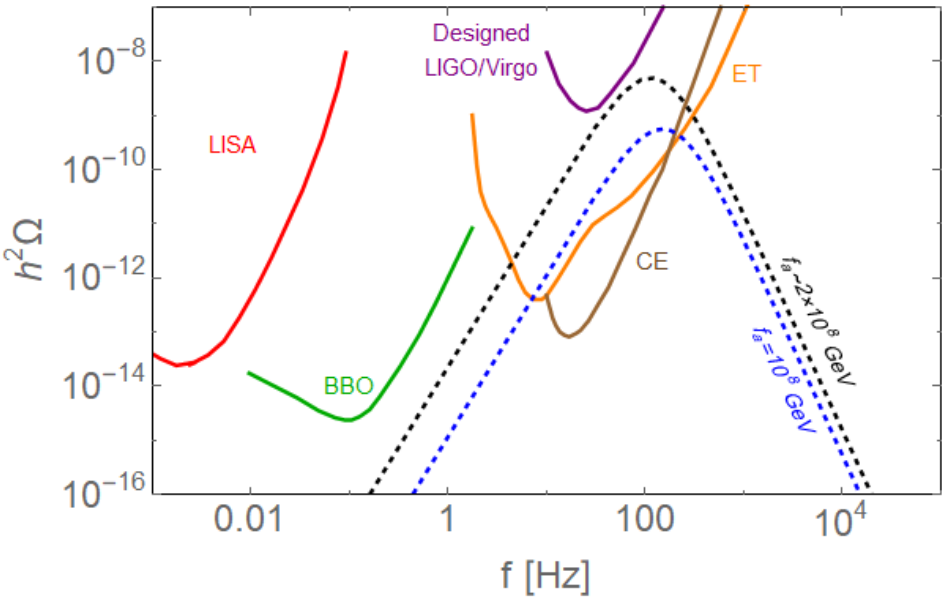

Figure 31: Gravitational wave signal from first order phase transition associated with the potential with parameters $\lambda = -0.45$, $m = 2$, $y = 1.432$, and $\Lambda = \mu = 100$. The parameters describing the phase transition are listed in Table 7 for the various scales. The appropriate units for the dimensionful parameters can be restored by multiplying by the last line in that table.

Benchmark Point 4			
f_a (10^8GeV)	1	2.61	10
α	0.40	0.61	-
$\beta/H_\star$	41.3	13.6	-
$T_\star$ (10^7GeV)	1.83	4.20	-
T_p (10^7GeV)	1.49	3.16	-
Units (10^6GeV)	1.56	4.08	15.6

Table 7: Quantities pertaining to the analysis of the gravitational spectrum for various scales for the benchmark $\lambda = -0.45$, $m = 2$, $y = 1.432$, and $\Lambda = \mu = 100$. The appropriate units for the dimensionful parameters can be restored by multiplying by the last line in this table.

5.3.2 Approximating the model

The previous subsection was dedicated to the numerical analysis of the Peccei-Quinn phase transition in the minimal KSVZ model including a dimension 6 operator. This

included the computation of the important quantities related to phase transition and the gravitational wave spectrum. However, it would be preferable to have analytic expressions for these quantities to get a better understanding of their scaling with the parameters of the model. In the next subsections, various approximations are considered in this Peccei-Quinn model including a dimension 6 operator. This allows one to obtain analytic results for the bounce action as well as the parameters α and $\beta/H_\star$, determining the gravitational wave spectrum, as functions of the coupling and mass scales of the scalar potential. The results in this subsection also comprise of original work for the thesis.

The objective is to write the potential in such a way that it only depends on one parameter, say δ, instead of the various coefficients that were originally present in the potential. This will be achieved via a field redefinition. The new parameter δ itself will be a function of the original coefficients. This idea is based on [109], where this was achieved for a quartic potential. The generalization to a potential including a dimension 6 operator is original work. The trick is that the bounce action can be computed for various values of δ, after which these data points can be fitted. This yields a function that can be used to determine the bounce action for any value of δ, without having to compute the bounce action each time. To achieve this, some terms in the potential will be neglected. Nonetheless, it will be shown that the absence of such terms can be corrected by a small variation of other parameters in the model.

The potential under consideration contains not only the tree-level contribution, but also the one-loop and thermal corrections, both coming from the scalar field and the fermion. This is where the first approximation comes in: the scalar contribution will be neglected. Nevertheless, an example demonstrates that this approximation can be compensated by shifting one of the parameters. Indeed, lowering the Yukawa coupling in the case of the approximation will yield similar results as the ones obtained with the full potential. This can be seen in Fig. 32, where the bounce action is used to illustrate this. It is important to stress that this approximation, although not exact, can still be very useful. Getting an intuition of how the bounce action behaves when varying various parameters can be achieved by considering this approximation with a re-scaled Yukawa.

Before continuing, it might be interesting to give more thought to why this approximation can be compensated by the lowering of the Yukawa coupling. For this, consider the one-loop corrections given in Fig. 33. As the scalar loop has two vertices, coming from the quartic interaction with coupling λ, this diagram will contribute as $\sim \lambda^2$. On the other hand, the fermion loop has four insertions of the Yukawa coupling, resulting in a $\sim y^4$ contribution. However, as the latter is a fermion loop, it will carry a minus sign, differing from the positive scalar one-loop contribution. When considering the full theory, an effective one-loop correction $\sim \lambda^2 - y^4$ is present. However, when neglecting the scalar loop contribution, this correction will only contain a term $\sim -y^4$. It is clear that the quartic coupling λ makes the effective one-loop correction less negative, which

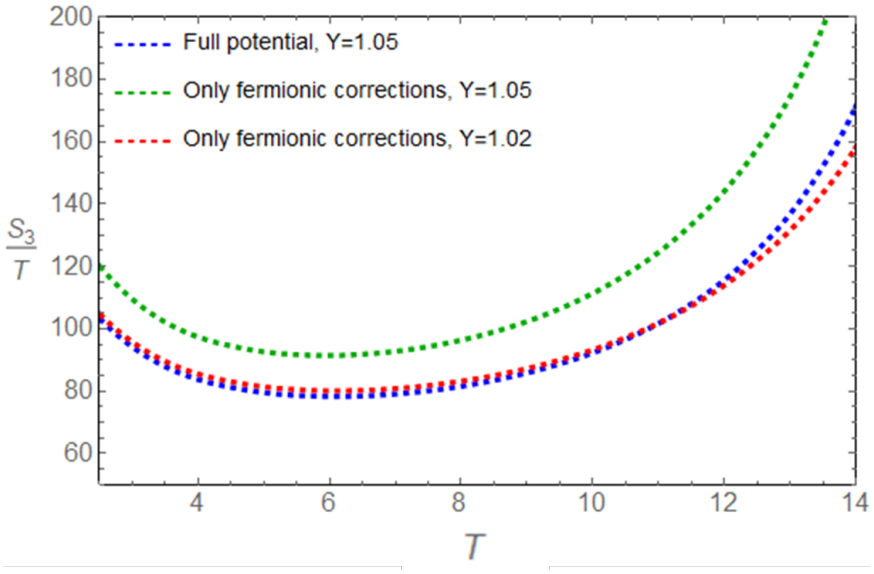

Figure 32: Bounce action computed with the full potential (blue), the approximation with only fermions with the same Yukawa coupling (green) and with a lower coupling (red). As can be seen, the approximation with a lower Yukawa coupling matches the bounce action of the full potential. The units of the dimensionful parameters did not need to be specified as only the dimensionless ratio mattered for this computation.

can also be achieved by simply lowering the Yukawa coupling in the case where the scalar is not considered. This is only an estimate in which the pre-factors are not computed exactly, but it already shows conceptually why lowering the Yukawa coupling helps to get closer to the result obtained by using the full theory.

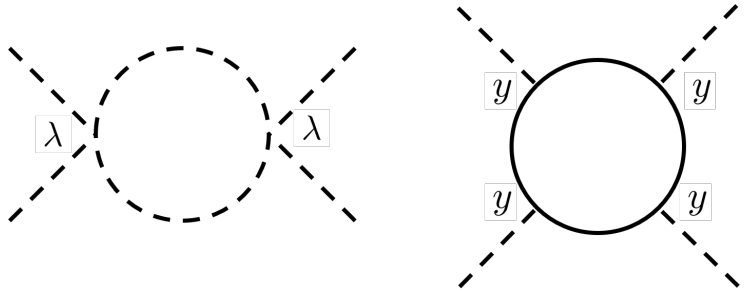

Figure 33: Two diagrams contributing to the quartic scalar interaction at one-loop.

One recalls that the goal is to be able to write the potential as a function of one parameter only. To this end, another approximation is made. Instead of using the exact expression in the computation of the thermal contribution of the fermion given by Eq. (2.15), the high-temperature expansion will be used, i.e. Eq. (2.16). Again, this effect can be com-

pensated by lowering the Yukawa coupling of the fermion. This is depicted in Fig. 34, where the full potential is compared to the approximated one with the same and lower Yukawa coupling for a specific point in parameter space.

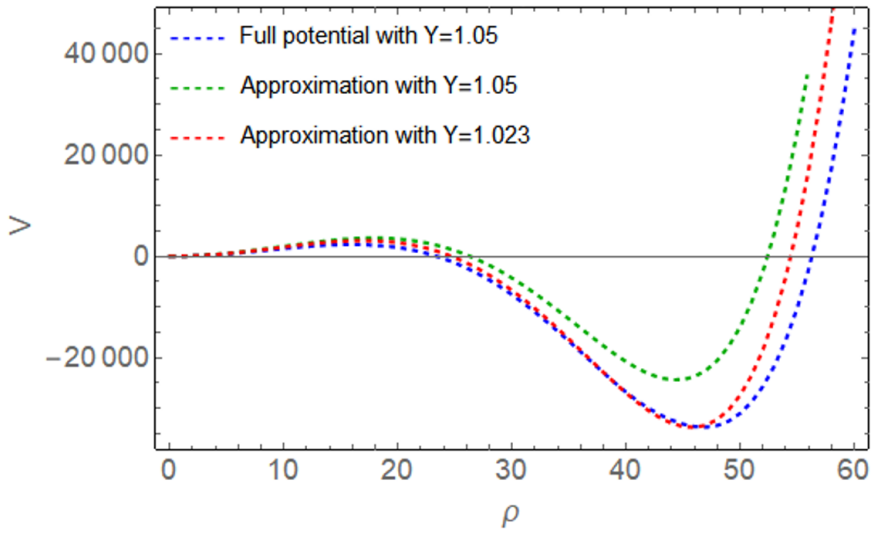

Figure 34: Comparison between the full potential with $y = 1.05$ (blue) and the approximation with only fermions for $y = 1.05$ (green) and $y = 1.023$ (red) for $\lambda = -0.24$, $m = 1$, $\mu = \Lambda = 100$ and temperature $T = 13$, where the units of the dimensionful parameters did not need to be specified as only the dimensionless ratio mattered for this computation.

Ignoring the scalar contribution to the one-loop correction yields

$$V_1(\phi) = -\frac{3y^4\phi^4}{64\pi^2}\left(\log\frac{y^2\phi^2}{2\mu^2} - \frac{3}{2}\right), \tag{5.17}$$

where the expression for the mass of the fermion given by Eq. (5.14) was filled in. Using the high-temperature expansion in Eq. (2.16), the fermionic thermal contribution to the potential reads

$$V_T(\phi, T) = -\frac{6T^4}{\pi^2}\left(\frac{7\pi^4}{360} - \frac{\pi^2}{48T^2}y^2\phi^2 - \frac{1}{128}\frac{y^4\phi^4}{T^4}\log\frac{y^2\phi^2}{2a_fT^2}\right), \tag{5.18}$$

where the expression for the mass was used again and $\log a_f = 2.6351$, as previously introduced [1]. Putting the above results together, one finds that the potential, including only fermionic corrections, takes the form

$$V(\rho) = \frac{1}{8\Lambda^2}\rho^6 + \left(\frac{\lambda}{4} + \frac{9}{128\pi^2}y^4 + \frac{3}{64\pi^2}y^4\log\left(\frac{\mu^2}{a_fT^2}\right)\right)\rho^4 + \left(\frac{1}{2}m^2 + \frac{T^2y^2}{8}\right)\rho^2, \tag{5.19}$$

such that the potential depends on the field ρ and essentially three parameters, i.e. the temperature-dependent coefficients in front of ρ^2, ρ^4 and ρ^6.

To summarize, the full potential was approximated by neglecting the scalar one-loop and thermal corrections and by approximating the fermionic thermal contribution by its high-temperature expansion. It was then illustrated that the result of the full theory could be recovered by changing the Yukawa coupling a few percent. As is made clear by the two graphs in Fig. 32 and Fig. 34, the final approximation with a lowered Yukawa coupling yields similar results to the full potential. Although these results are not identical, this can still be useful. For example, this approximation can be used to study behaviors as parameters are varied. Furthermore, it could be that this difference of a few percent in Yukawa coupling is irrelevant. Indeed, suppose that one wants to use a gravitational wave signal to obtain an indirect measurement of the parameters of the model. Using the approximated model to get the value of the Yukawa coupling from the gravitational wave signal, one knows there will be an error of a few percent because the approximation was used. However, this could be completely irrelevant in the sense that an error of a few percent would have been obtained from the exact model due to an error in the gravitational wave signal that was measured, e.g. due to detector noise. Thus, both approximated and exact model would yield an error, but using the approximated model to do the analysis will be simpler.

5.3.3 Semi-analytic understanding of the bounce action

The aim of this section is to obtain a semi-analytic result for the bounce action, as this would make the computation of the parameters describing the phase transition numerically more efficient. To this end, the potential needs to be rewritten in terms of a single parameter δ. It was just shown that by making some approximations, the potential can be written in the form

$$V = a\rho^6 - b\rho^4 + c\rho^2, \tag{5.20}$$

where these coefficients relate to the ones of Eq. (5.19) and are all positive. Indeed, the coefficient in front of the quartic in Eq. (5.19) is negative as we are working in the high temperature regime, such that there is a barrier present. As mentioned previously, the goal is to write this potential as a function of one single parameter, say δ. Hence, the following coordinate transformation is used

$$\rho = \sqrt{\frac{b}{6a}}\phi, \qquad r = \frac{\sqrt{6a}}{b}\xi. \tag{5.21}$$

This allows one to write the equation of motion

$$\frac{d^2\rho}{dr^2} + \frac{2}{r}\frac{d\rho}{dr} - \frac{\partial V}{\partial \rho}(\rho(r)) = 0 \tag{5.22}$$

as

$$\frac{d^2\phi}{d\xi^2} + \frac{2}{\xi}\frac{d\phi}{d\xi} - \frac{\partial \widetilde{V}}{\partial \phi}(\phi(\xi)) = 0, \tag{5.23}$$

where the potential now reads

$$\widetilde{V} = \frac{1}{6}\phi^6 - \phi^4 + \frac{\delta}{2}\phi^2. \tag{5.24}$$

Thus, it is possible to write the potential as a function of a single coefficient δ, which relates to the original coefficients as

$$\delta = \frac{12ac}{b^2}. \tag{5.25}$$

Computation of the bounce action

As will be clear later on, it is interesting to write the potential differently, by separating the part of the potential where the two minima are degenerate and a part that causes the asymmetry between the two minima. The potential now looks like

$$\widetilde{V}(\phi) = \frac{1}{6}\phi^2(\phi^2 - 3)^2 - \frac{\phi^2}{2}(3 - \delta) = V_0 + V_\varepsilon, \tag{5.26}$$

where V_0 represents the case when the two vacua are degenerate and V_ε causes the asymmetry between vacua. For $\delta = 0$, there is no barrier, whereas for values between 0 and 3 a barrier is present. The value $\delta = 3$ corresponds to the case where the two minima are degenerate and above this value, the minimum at the origin is the global minimum.

Recall that the objective is to compute the bounce action for various values of the parameter δ. Starting from the action S_3 given by

$$S_3 = 4\pi \int_0^\infty dr\ r^2 \left(\frac{1}{2} \left(\frac{d\rho}{dr} \right)^2 + V(\rho(r)) \right), \tag{5.27}$$

one can apply the coordinate transformations (5.21), yielding

$$S_3 = \frac{4\pi}{\sqrt{6a}} \int_0^\infty d\xi\ \xi^2 \left(\frac{1}{2} \left(\frac{d\phi}{d\xi} \right)^2 + \widetilde{V}(\phi(\xi)) \right) = \frac{4\pi}{\sqrt{6a}} B_3(\delta), \tag{5.28}$$

where B_N was just introduced as

$$B_N = \int_0^\infty d\xi\ \xi^{N-1} \left(\frac{1}{2} \left(\frac{d\phi}{d\xi} \right)^2 + \widetilde{V}(\phi(\xi)) \right), \tag{5.29}$$

where $N = 3$ or 4, depending on which action needs to be computed, i.e. S_3 or S_4 (see Section 2). The next step to obtain a semi-analytic expression for the bounce action is to numerically compute this function and fit it. However, to obtain a smoother function, one considers the ratio of the above quantity to the same quantity in the thin-wall limit of the bubble [40, 70, 110]. In this limit, it is assumed that the bubble radius R is big compared to its thickness. Concretely, this means that the region of the bubble profile

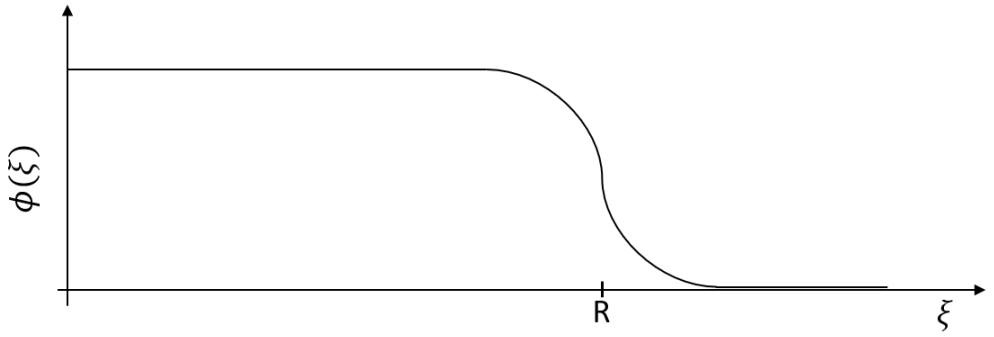

Figure 35: Illustration of the bounce profile in the thin-wall limit. As can be seen, the region where the field changes from true to false vacuum around $\xi \sim R$ is small compared to R.

$\phi(\xi)$ where the field ϕ changes from one vacuum to another at $\xi \sim R$ is small compared to R. This is illustrated in Fig. 35. In this thin-wall regime, one can split the above integral over three regions: $\xi < R$, $\xi \sim R$ and $\xi > R$. The last case corresponds to the region where the field ϕ sits in the false vacuum, where the potential is zero and $\frac{d\phi}{d\xi} = 0$. Thus, this region does not contribute to the integral in Eq. (5.29). For the case $\xi < R$, the field sits in the true vacuum, where $V(\phi_T) = -\varepsilon$ and $\frac{d\phi}{d\xi} = 0$. Therefore, this contribution reads

$$\int_0^R d\xi \; \xi^{N-1} \widetilde{V}(\phi_T) = -\frac{\varepsilon R^N}{N}. \tag{5.30}$$

The last contribution comes from the region where ϕ transitions from true to false vacuum over $\Delta\xi$ at $\xi \sim R$. Here, it is assumed that R is large enough such that $d\phi/d\xi$ can be neglected, yielding

$$\int_{\Delta\xi} d\xi \; \xi^{N-1} \left(\frac{1}{2} \left(\frac{d\phi}{d\xi} \right)^2 + \widetilde{V}(\phi(\xi)) \right) = R^{N-1} S_1, \tag{5.31}$$

where the dimensionless one-dimensional action S_1 was defined. In this case, it reads

$$S_1 = \int d\xi \; 2V_0(\phi) = \int_{\phi_F}^{\phi_T} d\phi \sqrt{2V_0}, \tag{5.32}$$

extending from false to true vacuum and with the assumption that $\widetilde{V} \approx V_0$. As this computation is performed in the case of almost degenerate vacua, this assumption is valid. The above result is obtained by using $d\xi = \frac{d\xi}{d\phi} d\phi$, together with the expression for $\frac{d\xi}{d\phi}$ obtained from the equation of motion. The above computations allow one to write B_N, given by Eq. (5.29), in the thin-wall limit as

$$B_{TW,N} = R^{N-1} S_1 - \frac{\varepsilon R^N}{N}. \tag{5.33}$$

However, the bubble radius R is still unspecified. Extremizing $B_{TW,N}$ with respect to R yields

$$R = (N-1)S_1/\varepsilon, \tag{5.34}$$

after which one obtains

$$B_{TW,N} = \frac{(N-1)^{N-1}}{N}\frac{S_1^N}{\varepsilon^{N-1}}. \tag{5.35}$$

Applying the above results to the potential that is considered here, one is able to read off from Eq. (5.26) that $\varepsilon = \frac{3}{2}(3-\delta)$. Using the same equation, the computation of S_1 gives

$$S_1 = \int_{\phi_F}^{\phi_T} d\phi\sqrt{2V_0} = \frac{1}{\sqrt{3}}\int_0^{\sqrt{3}} \phi(3-\phi^2)d\phi = \frac{9}{4\sqrt{3}}. \tag{5.36}$$

Putting this together in Eq. (5.35), one finds $B_{TW,N}$:

$$B_{TW,N} = \frac{(N-1)^{N-1}}{N}\frac{3^{N/2+1}}{(3-\delta)^{N-1}2^{N+1}}, \tag{5.37}$$

which for $N = 3$, since the quantity of interest will be S_3, takes the form:

$$B_{TW,3} = \frac{3^{3/2}}{4(3-\delta)^2}. \tag{5.38}$$

Going back to the original objective of fitting the action S_3, one defines the ratio $R_3(\delta)$ as the ratio of $B_3(\delta)$ to the thin-wall limit $B_{TW,3}$, given by Eq. (5.38), yielding

$$R_3(\delta) = \frac{B_3(\delta)}{B_{TW,3}} = \frac{4}{3^{3/2}}(3-\delta)^2 B_3(\delta). \tag{5.39}$$

The following step consists of the numerical computation of $R_3(\delta)$, and thus also $B_3(\delta)$, after which this function only needs to be fitted once. This function is reasonably fitted by

$$R_3(\delta) = \sqrt{\delta}\left(\gamma_0 + \gamma_1\delta + \gamma_2\delta^2 + \gamma_3\delta^3\right), \tag{5.40}$$

where $\gamma_0 = 2.4239$, $\gamma_1 = -0.4640$, $\gamma_2 = -0.1343$ and $\gamma_3 = 0.0284$. Using this expression together with Eq. (5.28) and (5.39), one is able to find a semi-analytic expression for S_3:

$$S_3 = \frac{3^{3/2}\pi}{\sqrt{6a}(3-\delta)^2}\sqrt{\delta}\left(\gamma_0 + \gamma_1\delta + \gamma_2\delta^2 + \gamma_3\delta^3\right). \tag{5.41}$$

It is important to stress the advantage of such an expression and how time-saving this is. Indeed, now for any combination of the original parameters of the model and for any temperature, the corresponding δ can be computed using Eq. (5.25), after which the result can be used to calculate the action S_3. Subsequently one divides S_3 by the temperature, yielding the value of the bounce action at that temperature. As an example, the exactly computed bounce action with the above approximations is displayed together with the semi-analytic approximation in Fig. 36.

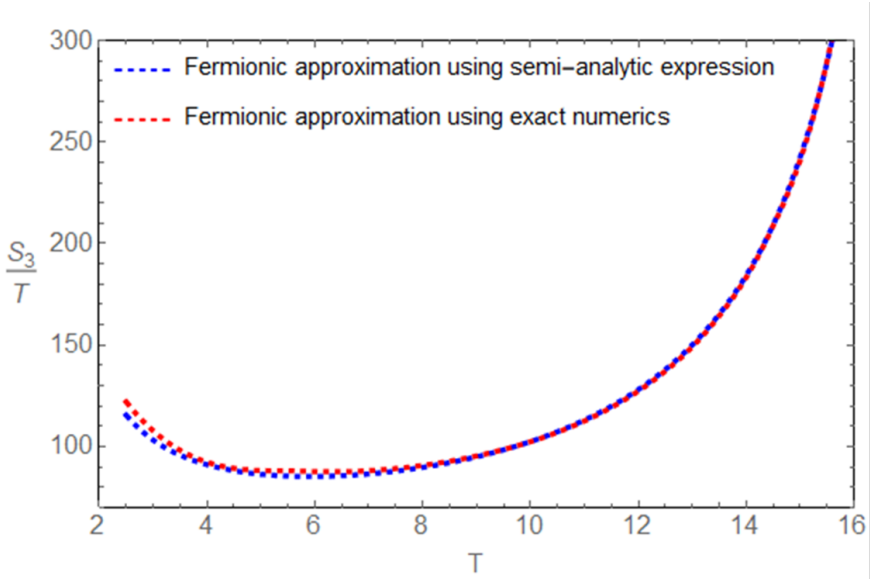

Figure 36: Bounce action for the approximation with only fermionic contributions computed using the semi-analytic approximation (blue) and using numerics only (red) for $\lambda = -0.24$, $m = 1$, $y = 1.02$ and $\Lambda = \mu = 100$, where the units of the dimensionful parameters did not need to be specified as only the dimensionless ratio mattered for this computation.

Parameters describing the phase transition

With this approximation, it is also possible to write an expression for the parameters describing the phase transition associated with the potential in Eq. (5.20), namely α and $\beta/H_\star$ for a given temperature. From a computation point of view, this saves a lot of time as the numerical work now just boils down to filling in some values in a formula. However, the nucleation temperature $T_\star$ still needs to be computed numerically and will serve as input for the other two parameters.

First, the computation of α is outlined. To compute α, one needs to determine the vacuum energy density given in Eq. (2.45). Recall that to this end, the vacuum expectation value of the potential needs to be determined as a function of the temperature. The vacuum of the potential in Eq. (5.20) is found by minimizing the potential and yields

$$\eta(T) = \sqrt{\frac{4b + \sqrt{16b^2 - 48ac}}{12a}}, \tag{5.42}$$

where, as in Eq. (2.45), $\eta(T)$ stands for the vacuum expectation value at temperature T. It is important to keep in mind that the parameters of the potential b and c are functions of the temperature. Indeed, a, b and c correspond to the coefficients of the approximated potential in Eq. (5.19). As the potential needs to be evaluated at the vacuum to determine the vacuum energy density, the above result is filled in the potential,

which now reads

$$V(\eta(T),T) = -\frac{b+\sqrt{b^2-3ac}}{27a^2}\left(-6ac + b\left(b+\sqrt{b^2-3ac}\right)\right). \tag{5.43}$$

The following ingredient that is necessary in the computation of the vacuum energy density is the derivative of the potential with respect to the temperature. This can be determined to be:

$$\frac{dV}{dT}(\eta(T),T) = \frac{8\pi^2 aT^2y^2\left(\sqrt{b^2-3ac}+b\right) - 2by^4\left(\sqrt{b^2-3ac}+b\right) + 3acy^4}{96\pi^2a^2T}, \tag{5.44}$$

where the explicit expression of the coefficients a, b and c and was used by comparing Eq. (5.20) to Eq. (5.19) to obtain the expression for the coefficients. Finally, α then takes the form

$$\alpha(T) = \frac{30}{\pi^2 g_\star T^4}\left(-V(\eta(T),T) + T\frac{dV}{dT}(\eta(T),T)\right), \tag{5.45}$$

where Eq. (5.43) and Eq. (5.44) can be plugged in and $g_\star$ is the number of relativistic degrees of freedom, as introduced in Section 2.

With an expression for α, one can now proceed to compute β/H. The expression for β/H follows directly from its definition. Indeed, now that a semi-analytic expression is available for the bounce action, namely Eq. (5.41), one can simply compute its derivative and multiply by T, yielding β/H at a specific temperature T:

$$\begin{aligned}\frac{\beta}{H}(T) = \frac{\pi 3^{3/2}}{\sqrt{6a}(3-\delta)^2}\Bigg(&\left(\gamma_0\delta^{1/2}+\gamma_1\delta^{3/2}+\gamma_2\delta^{5/2}+\gamma_3\delta^{7/2}\right)\left(\frac{2\delta'}{3-\delta}-\frac{1}{T}\right)\\ &+\delta'\left(\frac{1}{2\sqrt{\delta}}\gamma_0+\frac{3}{2}\gamma_1\delta^{1/2}+\frac{5}{2}\gamma_2\delta^{3/2}+\frac{7}{2}\gamma_3\delta^{5/2}\right)\Bigg),\end{aligned} \tag{5.46}$$

where

$$\delta' = \frac{12a}{b^4}\left(\frac{y^2b}{4}T - 3\frac{bcy^4}{16\pi^2T}\right) \tag{5.47}$$

and the coefficients γ_i are given above Eq. (5.41). This last quantity δ' is the derivative of δ with respect to the temperature. It can be computed by filling in the explicit expression of the coefficients a, b and c and compute their derivative, i.e. compare Eq. (5.20) to Eq. (5.19) to obtain the expression for the coefficients.

After the numerical computation of the nucleation temperature $T_\star$, both $\alpha(T)$ and $\beta/H(T)$ can be evaluated at that temperature to yield the parameters describing the phase transition. It is important to stress that these expressions are not approximate. These are the exact formulas for α and β/H, using the approximate potential given by Eq. (5.20).

Scan over the parameter space

With this semi-analytic computation, the scans in Fig. 19 can now be redone, i.e. computed with the approximate potential, and compare it with the full potential to see how accurate this approximation is. The result is shown in Fig. 37.

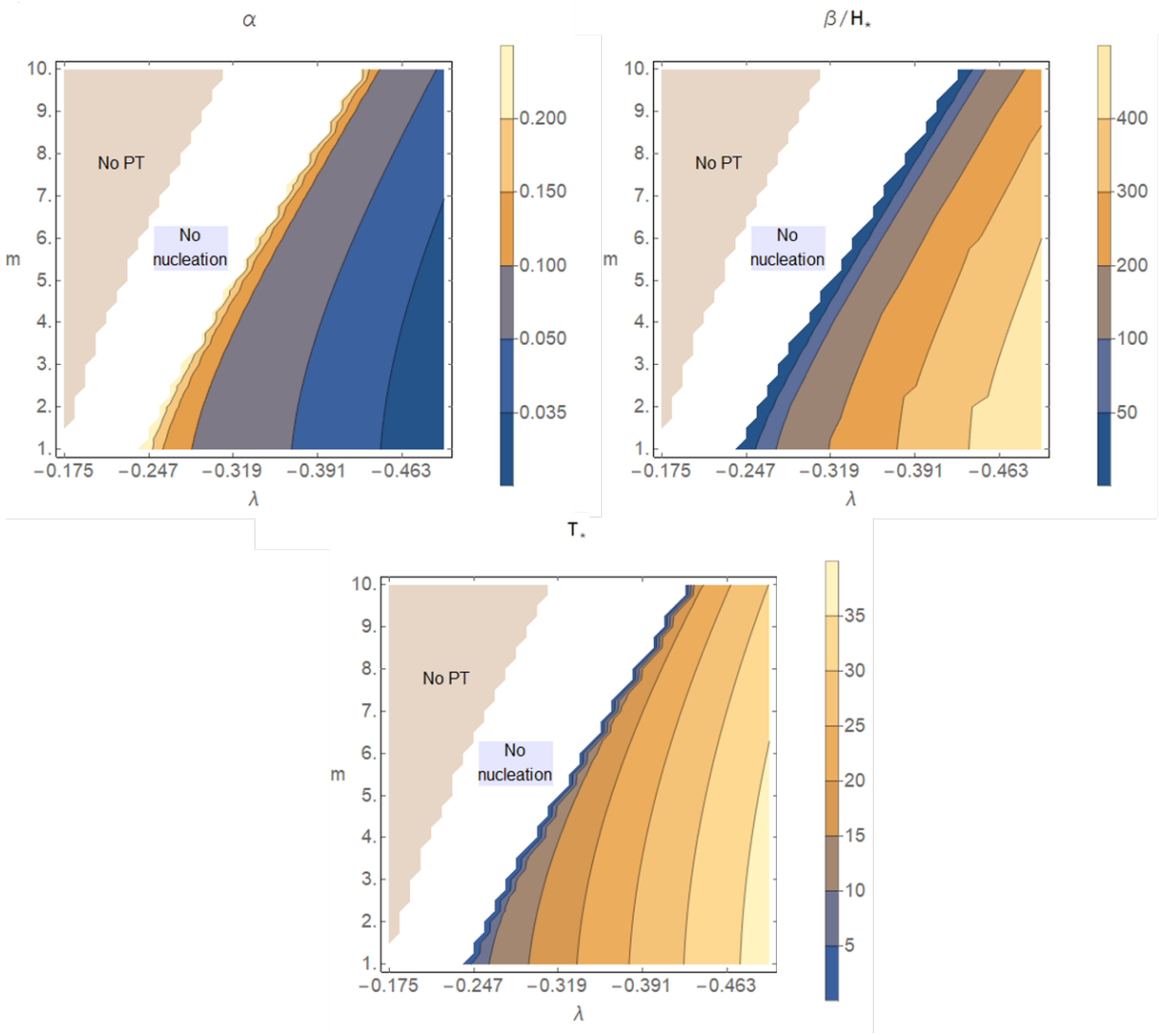

Figure 37: α, $\beta/H_\star$ and $T_\star$ for various values of λ and m, with $y = 1.05$ and $\mu = \Lambda = 100$ using the semi-analytic approximation with only fermionic contributions. The appropriate units for the dimensionful parameters can be restored by multiplying by 4.08×10^6 GeV.

A difference that stands out is that the region of no nucleation is substantially larger when the approximation is used. This was to be expected as it was seen that one of the consequences of approximating the model with only fermionic contributions was a

larger bounce action. Recall that the bounce action needs to go low enough to allow for the nucleation condition given by Eq. (2.43) to be satisfied. Thus, it makes sense that this approximation results in a larger region where nucleation does not take place. Nonetheless, one clearly recognizes the same trend for the various parameters in these scans. Indeed, α and $\beta/H_\star$ still display the same correlation: as α increases, $\beta/H_\star$ decreases, together with the nucleation temperature $T_\star$. Furthermore, the highest values of α and thus, also the lowest values of $\beta/H_\star$, can be found closest to the region where nucleation does not take place.

It was previously mentioned that when lowering the original Yukawa coupling a few percent, the approximation would match the exact result better. To illustrate this, the scan is repeated using the semi-analytic approximation, but with a lower Yukawa coupling. This results in the scans depicted in Fig. 38. One notices that the region where nucleation does not happen now matches in both scans, showing that a lower Yukawa coupling indeed reduces the bounce action.

As an example, the analysis of one of the benchmark points will be performed using the above approximation for comparison. To this end, consider benchmark point 1 in Table 2, i.e. $\lambda = -0.4,\ m = 2,\ y = 1.05$, and $\Lambda = \mu = 100$. Only the case where the units are chosen such that $f_a = 2.86 \times 10^8$ GeV will be considered here, namely 4.08×10^6 GeV. The relevant quantities will be computed using the semi-analytic approximation for two different Yukawa couplings : $y = 1.05$ and $y = 0.97$ as in the scans above. The bounce action is depicted in Fig. 39 for comparison. The parameters describing the phase transition in the various cases are summarized in Table 8.

	Full potential	Approximation	
Yukawa y	1.05	1.05	0.97
f_a (10^8GeV)	2.86	2.76	2.82
α	0.038	0.043	0.030
$\beta/H_\star$	498	330	404
$T_\star$ (10^7GeV)	12.1	11	12.7

Table 8: Quantities pertaining to the analysis of the gravitational spectrum for various scales for the benchmark $\lambda = -0.4,\ m = 2,\ y = 1.05$, and $\Lambda = \mu = 100$ for the full potential and the approximation. The appropriate units for the dimensionful parameters can be restored by multiplying by 4.08×10^6 GeV.

From Table 8, it is clear that the values of the parameters α, $\beta/H_\star$ and the nucleation temperature $T_\star$ obtained using the semi-analytic expression with only fermionic contributions do not entirely match the exact result using the full potential. This was to be expected, as the scalar contributions are after all completely neglected. Nonetheless, the

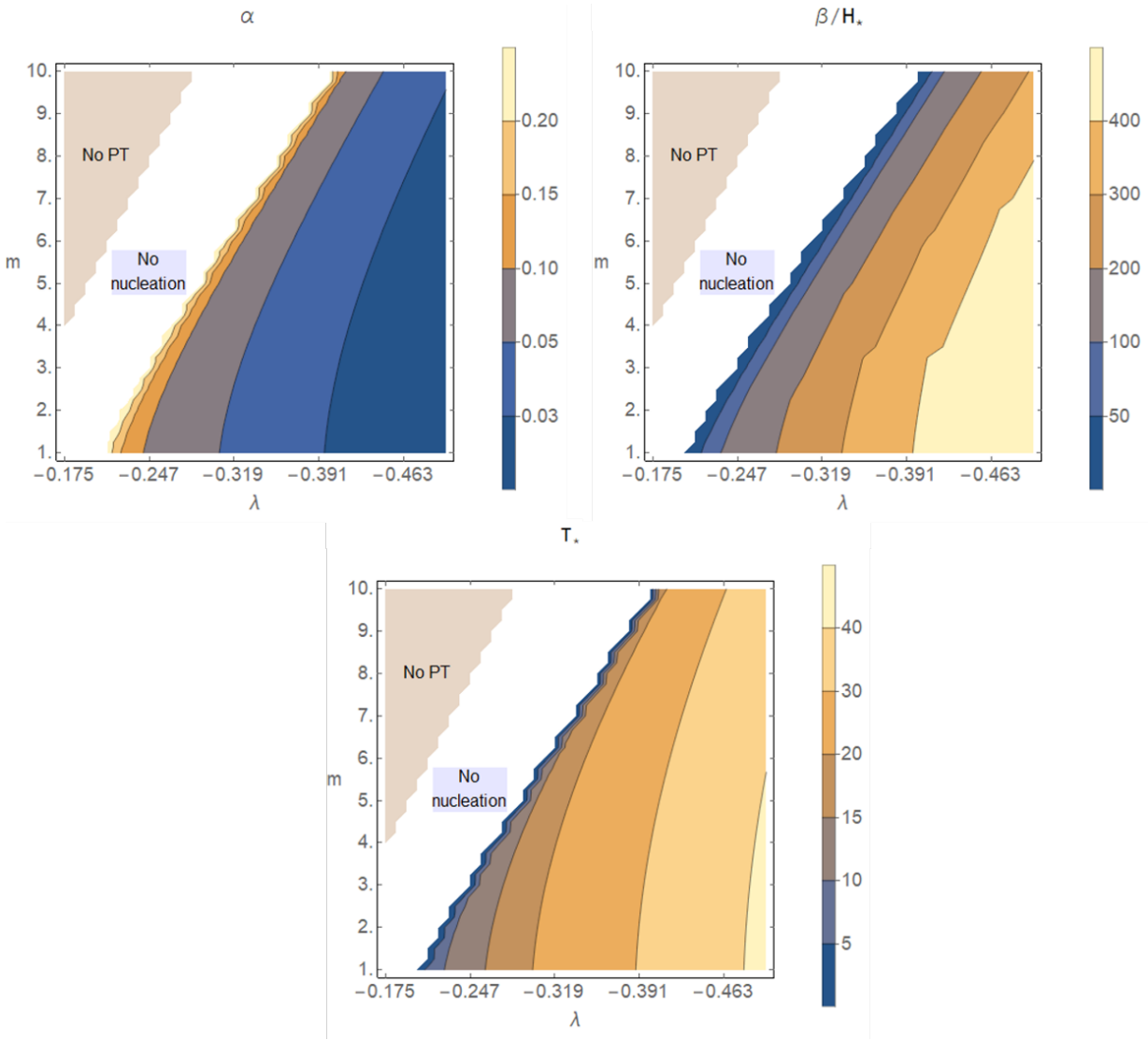

Figure 38: α, $\beta/H_\star$ and $T_\star$ for various values of λ and m, with $y = 0.97$ and $\mu = \Lambda = 100$ using the semi-analytic approximation with only fermionic contributions. The appropriate units for the dimensionful parameters can be restored by multiplying by 4.08×10^6 GeV.

semi-analytic approximation is still useful. It allows to get an estimate of the behavior of the quantities describing the phase transition in a computationally efficient way. Indeed, one sees that the behavior of the parameters in the scans with the semi-analytic approximation, i.e. location of highest values, correlation, etc., agree with the scans where the quantities are computed exactly using the full potential. Therefore, such an approximation can be used to probe large regions of parameter space very efficiently.

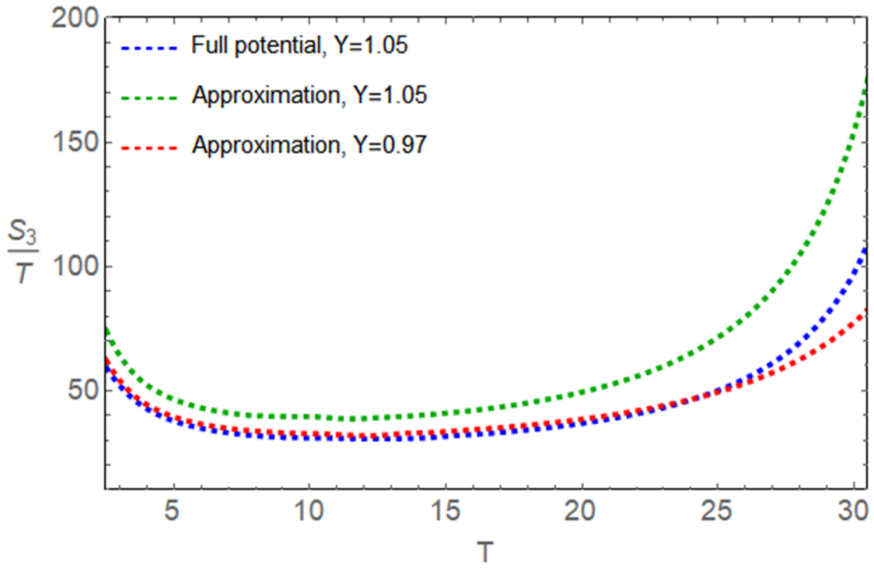

Figure 39: Bounce action computed exactly for the full potential (blue), together with the semi-analytic computation with only fermionic contributions for $y = 1.05$ (green) and $y = 0.97$ (red) for $\lambda = 0.4$, $m = 2$ and $\Lambda = \mu = 100$. The appropriate units for the dimensionful parameters can be restored by multiplying by 4.08×10^6 GeV.

After this, one can then focus on a specific region of interest and use the exact numerics with the full potential to obtain the correct value of the parameters.

5.3.4 Summary of the results

This last realization of the axion assumed a KSVZ-type model where the tree-level potential was augmented by a dimension 6 operator, motivated by effective field theory. It is found that this model exhibits first order phase transitions for a wide range of parameter values. Scans were performed to explore the parameter space, after which some benchmark points were studied in more detail. A more in depth analysis revealed that the stochastic background of gravitational waves generated during this phase transition is within reach of the Einstein Telescope and even the LIGO-Virgo experiments once their designed sensitivity is reached, as can be seen from Fig. 30 and Fig. 31. Furthermore, a semi-analytic understanding of the potential was developed as a way to have more intuition on how the various parameters of the phase transition vary as function of the underlying parameters of the model.

6 Conclusion and Outlook

This work started with the review of gravitational waves and more specifically, a stochastic background of gravitational waves. This background can be generated by a number of unresolved sources such as the merger of binary black holes or binary neutron stars, but can also be generated during the cosmological evolution of the Universe, e.g. during phase transitions [13]. The latter constituted the focus of this thesis. After the introduction of the effective potential, which includes both one-loop and thermal corrections to the tree-level potential, first order phase transitions were discussed in detail. It was explained how bubbles of true vacuum start appearing in a sea of false vacuum, converting the Universe from false to the true vacuum as the bubbles expand. The bubbles themselves do not generate a stochastic background of gravitational waves, but the collision of such bubbles does. This is because asymmetry is needed for the generation of gravitational waves, as the signal is related to the quadrupole moment. This gravitational wave signal was found to get contributions from the collision of bubble walls, from sound waves developing in the plasma and from magnetic turbulence. However, it was seen that the largest contribution came from sound waves. The position of the peak of the stochastic background of gravitational waves is determined by the scale of the temperature at which the phase transition completes, favoring lower scales, typically $T_\star \sim 10^2 - 10^7$ GeV, to be within reach of the current and future experiments. The above concepts were then applied to the analysis of a stochastic gravitational wave background from first order phase transitions in the remainder of the thesis.

Next, the Strong CP problem was reviewed in more detail. This problem follows from the fact that a CP violating term $\frac{\theta}{32\pi^2} G_{\mu\nu}\widetilde{G}^{\mu\nu}$ cannot be excluded from the Lagrangian. From experimental bounds on the neutron electric dipole moment, it follows that the θ-angle must be less than 10^{-9} [5]. As the other sources of CP violation in the SM are $\mathcal{O}(1)$, namely in the CKM matrix, this poses the question as to why this new angle is so small compared to the other sources of CP violation in the SM [6]. This question is also known as the Strong CP problem. Various solutions to this problem have been proposed, but the one of interest in this work is the axion solution. This solution assumes an extra $U(1)$ symmetry, usually referred to as the Peccei-Quinn symmetry [7,8]. The Goldstone boson associated with the spontaneous symmetry breaking of this $U(1)_{PQ}$ is the axion. The θ angle is then promoted to a dynamical variable including the axion field $a(x)$: $\theta(x) = a(x) + \theta$. The axion field is such that its potential is minimized for $\theta(x) = 0$, thus solving the Strong CP problem.

A warm-up exercise was then preformed in order to get acquainted with the various methods involved in the analysis of the phase transition and the gravitational wave signal. First order phase transitions were explored in the context of the SM with a cubic term in the Higgs potential. The same approach as in [98] was followed and yielded similar results.

The last section constituted original work on the analysis of the KSVZ model and its extensions. The possibility of the generation of visible gravitational wave signatures from first order phase transitions associated with the breaking of the Peccei-Quinn symmetry was explored. Armed with the necessary tools from the previous section, the minimal KSVZ model, i.e. the SM together with a scalar and a fermion both charged under $U(1)_{PQ}$, was explored. An extension of this model with two fermions instead of one was also considered. In both cases a barrier was not present and thus, no first order phase transition was found. Nevertheless, it is not excluded that adding more fermions would not generate a barrier.
Subsequently, another approach was adopted, in which the minimal KSVZ model was considered again, but with a dimension 6 operator added to the tree-level potential. This model was found to exhibit first order phase transitions leading to a gravitational wave signal. As the computation of the various quantities describing the phase transition is quite cumbersome, a semi-analytic approach was developed as a way to simplify the numerical computations and therefore, obtain results in a computationally more efficient way. This method is based on various approximations of the potential and does not yield exact quantitative results. Nevertheless, it clearly displayed the same qualitative behavior for the parameters describing the phase transition. Furthermore, this semi-analytic approximation can be used to explore the parameter space and acquire more information on how different quantities change as the parameters of the model are varied.

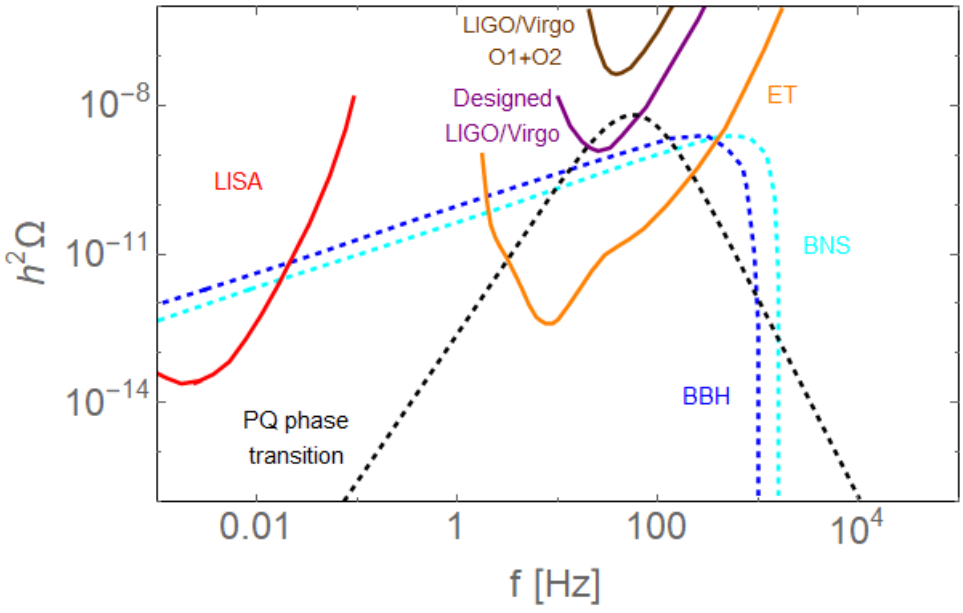

Figure 40: Gravitational wave experiments with signal for various stochastic backgrounds, including binary black holes (blue) [37], binary neutron stars (cyan) [111] and Peccei-Quinn phase transition obtained in this work (black).

The exploration of the parameter space allowed to find parameter values for which the resulting gravitational wave spectrum would be detectable by the future Einstein Telescope and even LIGO-Virgo once their designed sensitivity is reached. This is displayed in Fig. 40, which illustrates that the stochastic background of gravitational waves generated during phase transitions can be larger than the predicted astrophysical background (e.g. binary black holes and binary neutron stars). Moreover, the shape of the spectrum from a phase transition is different, obeying a broken power-law. These elements make the detection of such spectra generated by phase transitions promising, both with current and future gravitational wave detectors. These results provide a working example of how gravitational waves can be used to probe high energy physics beyond the Standard Model which would not be otherwise accessible at colliders due to the high energy scales involved.

A first aspect that should be the subject of research following this work is the generation of a barrier in models including more fermions. In this work, only the KSVZ model with up to two fermions was considered. Other models with more fermions were not explored due to the large amount of free parameters in such a model. Adding more fermions would yield more complicated mass eigenvalues as a function of the scalar field, potentially allowing for the thermal generation of a barrier [46].
Finally, it would be interesting to consider non-standard realization of the axion still solving the strong CP problem. In more extended theories, the typical relation between the axion decay constant and its mass can be different than the one for the QCD axion. This leads to different phenomenological constraints on the axion, e.g. it allows to lower the scale of the decay constant. From the point of view of the generation of a detectable stochastic background of gravitational wave this is very interesting, as it was seen that lower scales are favored to ensure that the peak of the gravitational wave is in the favorable frequency range to allow for detection. A specific mechanism to lower the scale of the decay constant is given in [112] and is reviewed in Appendix B.

7 Acknowledgment

Many people should be thanked for being there for me during this year while working on my thesis. Most importantly, I would like to thank Professor A. Mariotti for a great job done as a promotor. He was able to fulfill his role admirably in both physics and human aspects. Both of us did not know much about the topic when the year started, but thanks to many interesting conversations, we learned quickly. In times of doubt, he was able to reassure me and found the words to motivate me when needed.
I would also like to express my gratitude towards Dr. I. Baldes. His expertise on phase transitions was much needed and proved to be very helpful. This collaboration led to many instructive discussions and progress with the thesis. I truly appreciate the time and effort he put into helping me completing this thesis successfully.
Both Professor S. de Buyl and Professor A. Sevrin agreed to read this thesis, which I am very thankful for. I value their time and opinion a lot.

Appendices

A Renormalization Conditions

It will now be shown that one can go from the $\overline{\text{MS}}$ renormalization scheme, given by Eq. (2.11), to the one where the tree-level vacuum expectation value and mass are not altered by the one-loop correction, namely Eq. (2.14). This will be done for the case the squared masses are at most quadratic in the fields. This entails that the potential of the scalar will be taken of the form

$$V = -\frac{m^2}{2}\phi^2 + \frac{\lambda}{4}\phi^4. \tag{A.1}$$

This potential has a vacuum expectation value v, such that $v^2 = \frac{m^2}{\lambda}$. For simplification, only one fermion will be considered together with the scalar. The method remains the same when generalizing to more fermions. The mass of the scalar and the fermion are respectively given by

$$m_\phi^2(\phi) = 3\lambda\phi^2 - \lambda v^2 \qquad \text{and} \qquad m_f^2(\phi) = \frac{y^2}{2}\phi^2. \tag{A.2}$$

One starts from the one-loop correction and counter-terms

$$V_1 + V_1^{ct} = \frac{1}{64\pi^2}\sum_i n_i m_i^4(\phi)\left(\log\frac{m_i^2(\phi)}{\mu^2} - C_i\right) + \frac{1}{2}a\phi^2 + \frac{1}{4}b\phi^4, \tag{A.3}$$

where the sum ranges over the scalar and the fermion and a and b are determined by requiring that

$$\left.\frac{d(V_1 + V_1^{ct})}{d\phi}\right|_{\phi=v} = 0 \qquad \text{and} \qquad \left.\frac{d^2(V_1 + V_1^{ct})}{d\phi^2}\right|_{\phi=v} = 0. \tag{A.4}$$

Evaluating the first derivative of Eq. (A.3) yields

$$\begin{aligned}\frac{d(V_1 + V_1^{ct})}{d\phi} = \frac{1}{32\pi^2}\Bigg(&m_\phi^2\frac{dm_\phi^2}{d\phi}\log\frac{m_\phi^2}{\mu^2} - m_\phi^2\frac{dm_\phi^2}{d\phi} \\ &- 12\left(m_f^2\frac{dm_f^2}{d\phi}\log\frac{m_f^2}{\mu^2} - m_f^2\frac{dm_f^2}{d\phi}\right)\Bigg) + a\phi + b\phi^3,\end{aligned} \tag{A.5}$$

where the ϕ-dependence of the masses is not written explicitly, i.e. $m_\phi^2 = m_\phi^2(\phi)$ and $m_f^2 = m_f^2(\phi)$. The second derivative reads:

$$\begin{aligned}\frac{d^2(V_1 + V_1^{ct})}{d\phi^2} = \frac{1}{32\pi^2}\Bigg(&\left(\frac{dm_\phi^2}{d\phi}\right)^2\log\frac{m_\phi^2}{\mu^2} + m_\phi^2\frac{d^2m_\phi^2}{d\phi^2}\log\frac{m_\phi^2}{\mu^2} - m_\phi^2\frac{d^2m_\phi^2}{d\phi^2} \\ &- 12\left(\left(\frac{dm_f^2}{d\phi}\right)^2\log\frac{m_f^2}{\mu^2} + m_f^2\frac{d^2m_f^2}{d\phi^2}\log\frac{m_f^2}{\mu^2} - m_f^2\frac{d^2m_f^2}{d\phi^2}\right)\Bigg) + a + 3b\phi^2.\end{aligned} \tag{A.6}$$

A short-hand notation is now introduced:

$$\begin{aligned}
\omega &= m_\phi^2(v) = 2\lambda v^2, \quad \omega' = \left.\frac{dm_\phi^2(\phi)}{d\phi}\right|_{\phi=v} = 6\lambda v, \quad \omega'' = \left.\frac{d^2m_\phi^2(\phi)}{d\phi^2}\right|_{\phi=v} = 6\lambda \\
\gamma &= m_f^2(v) = \frac{y^2v^2}{2}, \quad \gamma' = \left.\frac{dm_f^2(\phi)}{d\phi}\right|_{\phi=v} = y^2 v, \quad \gamma'' = \left.\frac{d^2m_f^2(\phi)}{d\phi^2}\right|_{\phi=v} = y^2
\end{aligned} \tag{A.7}$$

After this, both Eq. (A.5) and Eq. (A.6) can be evaluated at $\phi = v$ and solved for a and b, yielding:

$$\begin{aligned}
a = &-\frac{1}{64\pi^2}\left(\left(3\frac{\omega\omega'}{v} - \omega'^2 - \omega\omega''\right)\log\frac{\omega}{\mu^2} + \omega\omega'' - 3\frac{\omega\omega'}{v}\right. \\
&+ \left. 12\left(\left(\gamma'^2 + \gamma\gamma'' - 3\frac{\gamma\gamma'}{v}\right)\log\frac{\gamma}{\mu^2} - \gamma\gamma'' + 3\frac{\gamma\gamma'}{v}\right)\right)
\end{aligned} \tag{A.8}$$

$$\begin{aligned}
b = &\frac{1}{64\pi^2v^2}\left(\left(\frac{\omega\omega'}{v} - \omega'^2 - \omega\omega''\right)\log\frac{\omega}{\mu^2} + \omega\omega'' - \frac{\omega\omega'}{v}\right. \\
&+ \left. 12\left(\left(\gamma'^2 + \gamma\gamma'' - \frac{\gamma\gamma'}{v}\right)\log\frac{\gamma}{\mu^2} - \gamma\gamma'' + 3\frac{\gamma\gamma'}{v}\right)\right)
\end{aligned} \tag{A.9}$$

Filling in the explicit expression for ω and γ, one finds

$$a = -\frac{1}{16\pi}\left(-3\lambda^2v^2\log\frac{\omega}{\mu^2} - 6\lambda^2v^2 + 3y^4v^2\right) \tag{A.10}$$

and

$$b = \frac{1}{16\pi^2}\left(-9\lambda^2\log\frac{\omega}{\mu^2} + 3y^4\log\frac{\gamma}{\mu^2}\right). \tag{A.11}$$

These can be plugged back into Eq. (A.3). To obtain the final result, one uses the fact that the squared masses are of the form $m_i^2 = \sigma^2 + \tau\phi^2$. This is essential to be able to write the final expression. If the masses were not of that form, some extra terms would be present in the following equation. It can then be shown that the above expression for the one-loop potential and its counterterms reduces to

$$\begin{aligned}
V_1 + V_1^{ct} = &\frac{1}{64\pi^2}\left(m_\phi^4(\phi)\left(\log\frac{m_\phi^2(\phi)}{m_\phi^2(v)} - \frac{3}{2}\right) + 2m_\phi^2(\phi)m_\phi^2(v)\right. \\
&- \left. 12m_f^4(\phi)\left(\log\frac{m_f^2(\phi)}{m_f^2(v)} - \frac{3}{2}\right) - 24m_f^2(\phi)m_f^2(v)\right)
\end{aligned} \tag{A.12}$$

This is exactly the one-loop correction from the other renormalization scheme given by Eq. (2.14). Thus, the above computation shows that one can go from one renormalization scheme to the other by requiring that the tree-level vacuum expectation value and mass are not altered by the one-loop contribution and its counterterms, provided that the square of the masses is at most quadratic in the field.

B Lowering the scale f_a

One recalls from Section 3 that the value of f_a can be constrained by experiments. The most stringent constraint came from supernovae, reading $f_a \gtrsim 2 \times 10^8$ GeV. However, it was argued that one might want to consider lower scales to be within reach of gravitational wave experiments. A possible way to lower the scale is given in [112]. There, a mirror sector is introduced as an attempt to lower the scale for f_a. A $\mathbb{Z}_2$ symmetry is considered to exchange between the fields of the mirror sector and the ones of Standard Model. The mirror sector is assumed to have the same gauge structure as the Standard Model to ensure that the Standard Model does not carry any charges of the mirror sector and vice versa. Furthermore, the dimensionless couplings are the same in both sectors, including the θ angle. A $\mathbb{Z}_2$-invariant coupling between QCD and axion is given by

$$\frac{\alpha_s}{8\pi}\left(\frac{a}{f_a}+\theta\right)\left(G\widetilde{G}+G'\widetilde{G}'\right). \tag{B.1}$$

The non-perturbative QCD' contribution to the axion potential near its minimum will be [112]:

$$V' = 0.3 \times (\alpha_s^{-0.4} \times \Lambda'_{\mathrm{QCD}})^4 \left(\frac{a}{f_a}+\theta\right)^2 + \mathcal{O}\left(\left(\frac{a}{f_a}+\theta\right)^4\right). \tag{B.2}$$

This shows that the potential, although having a contribution from the mirror sector, is still minimized for $\langle a \rangle = -f_a\theta$. Thus, one axion is enough to solve the strong CP problem in both sectors. Furthermore, the above addition to the axion potential will contribute to the mass of the axion, changing it to

$$m_a^2 \approx \left(\frac{m_u m_d}{(m_u+m_d)^2} m_\pi^2 f_\pi^2 + 0.6(\alpha_s^{-0.4} \times \Lambda'_{\mathrm{QCD}})^4\right)\frac{1}{f_a^2} \tag{B.3}$$

instead of the one given by Eq. (3.47), which only included the first term. One of the effects of this mirror sector is to increase the mass of the axion, or put in other words, lower the scale of the vacuum expectation value f_a. Therefore, the mirror sector provides a way to lower the scale of f_a such that it escapes the current constraints. This would allow to generate a gravitational wave signal, associated with a first order phase transition, that falls within reach of gravitational wave experiments. For the discussion about how the scale influences the peak of the gravitational wave signal, we refer to Section 2. The values of f_a as a function of the axion mass m_a are displayed in Fig. 41 for various cases. From this it is clear how the mirror sector allows for values of f_a at a lower scale, which are not excluded by experiments.

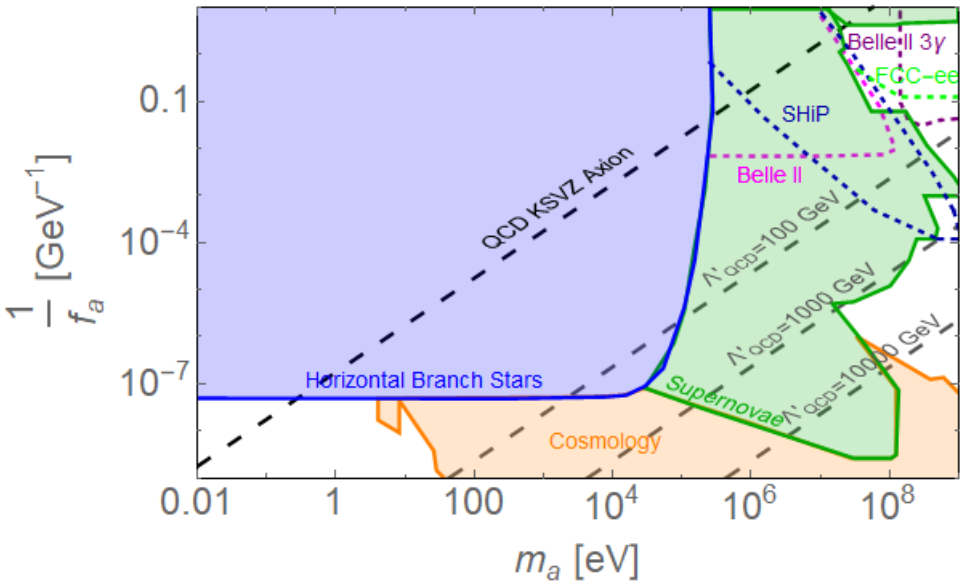

Figure 41: Relation between m_a and f_a for the QCD KSVZ axion (dotted black) and for the case of a mirror sector with various values of Λ'_{QCD}. This allows for lower scales, while escaping current constraints on the axion [112–116].

C Effective Field Theory

The modification of the minimal KSVZ model in Section 5 included a dimension 6 operator in the potential of the scalar. It was mentioned that such an operator could be achieved in the context of effective field theories (EFTs), as done for the Standard Model in [106]. A brief review of EFTs and how exactly this can be achieved is outlined below.

The effective Lagrangian is made up of a renormalizable Lagrangian and higher-dimensional interactions:

$$\mathcal{L}_{\text{eff}} = \mathcal{L} + \sum_i \frac{1}{\Lambda^{d_i-4}} c_i \mathcal{O}_i, \tag{C.1}$$

where d_i represents the dimension of the operator $\mathcal{O}_i$, Λ is the cut-off scale of the EFT and c_i is called a Wilson coefficient. These coefficients run as functions $c_i(\mu)$ of the renormalization group scale μ. It is important to note that the higher-dimensional operators respect the symmetries of the Lagrangian $\mathcal{L}$. To make sure that the UV model matches the EFT at the energy scale $\mu = \Lambda$, the coefficients $c_i(\Lambda)$ are determined order by order in a loop expansion such that the S-matrix elements in the EFT are the same as the ones of the UV model at that scale. How this matching concretely works, will not be described here. Nevertheless, one can now think of a possible scenario in which EFTs might be used. Assume someone has a UV model with massive states and wants to know how these new states will affect the theory. Of course, one could use the UV model itself to compute these effects. However, computations using the full UV model

are usually quite cumbersome, favoring the use of an EFT.

As just mentioned, new massive states can influence the underlying theory. To introduce a dimension 6 operator in the potential of the Peccei-Quinn scalar Φ given by

$$\mathcal{L} \supset m^2 \Phi^\dagger \Phi + \lambda \left(\Phi^\dagger \Phi\right)^2, \tag{C.2}$$

another massive complex scalar S charged under $U(1)_{PQ}$ with mass $m_S^2 \gg f_a^2$ is added, where f_a is the decay constant of the axion. Writing down the allowed couplings for the new scalar yields the following Lagrangian

$$\begin{aligned} \mathcal{L} \supset |\partial_\mu S|^2 - m_S^2 |S|^2 + \frac{\lambda_S}{4}|S|^4 + \left(\eta_\Phi |\Phi|^2 + \eta_S |S|^2\right)\left(\Phi^\dagger S + S^\dagger \Phi\right) \\ -\lambda_1 |S|^2 |\Phi|^2 - \lambda_2 |\Phi^\dagger S|^2 - \lambda_3 \left((\Phi^\dagger S)^2 + (S^\dagger \Phi)^2\right), \end{aligned} \tag{C.3}$$

where Φ is the original Peccei-Quinn complex scalar. From the linearized equation of motion for the field S, one obtains

$$S \approx -\frac{1}{\partial^2 - m_S^2} \eta_\Phi |\Phi|^2 \Phi \approx \frac{\eta_\Phi}{m_S^2} |\Phi|^2 \Phi. \tag{C.4}$$

When the new massive field is integrated out, i.e. replaced in Eq. (C.3) by the above value, the term $\eta_\Phi |\Phi|^2 \left(\Phi^\dagger S + S^\dagger \Phi\right)$, which is linear in the new field S, will contribute to the effective Lagrangian at tree-level. Indeed, in [106] it is shown that to ensure a tree-level contribution to the effective Lagrangian, a term linear in S is needed. Plugging in the value of the field S obtained from the equation of motion, one sees this term will contribute to the Lagrangian as follows:

$$\Delta\mathcal{L} = \frac{\eta_\Phi^2}{m_S^2} |\Phi|^6. \tag{C.5}$$

This illustrates how a dimension 6 operator can be generated in the context of effective field theory and motivates the addition of such operator to the tree-level potential of the KSVZ model, which was considered in Section 5.

D Sensitivity curves for gravitational wave experiments

In this work, the sensitivity curve of various experiments was considered for comparison with the gravitational wave signal obtained in the different models. The computation of these sensitivity curves is outlined below for the specific example of the LISA interferometer [117].

The output of a detector can be decomposed into noise and signal: $s(t) = n(t) + h(t)$,

where n represents the noise and h the signal. A quantity that is used in the computation of sensitivity curves is called the power spectral density (PSD). It can be shown that the noise PSD $S_n(f)$ is related to the noise $n(t)$ as

$$\overline{|n(t)|^2} = \int_0^\infty df\ S_n(f). \tag{D.1}$$

In other words, the time average of the square of the noise in the detector is equal to the integral of the PSD over all positive frequencies [118]. The simulated noise PSD for LISA is plotted in Fig. 42.

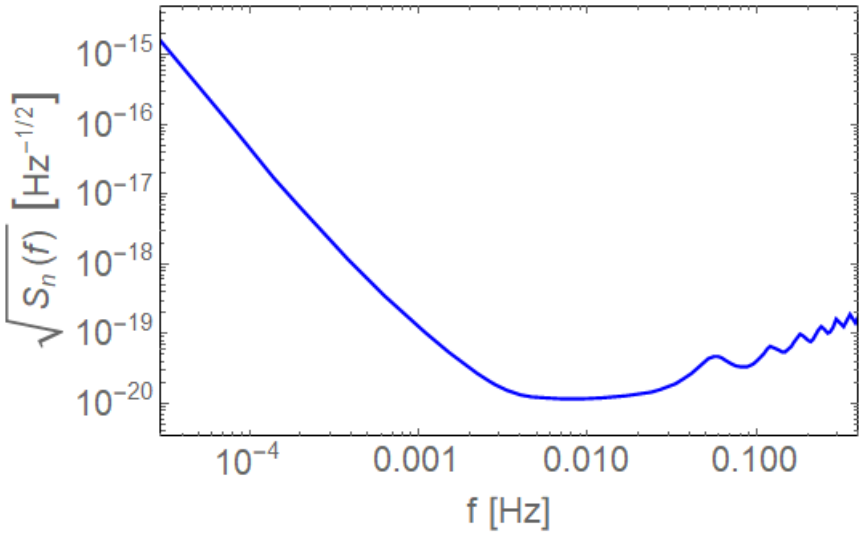

Figure 42: Square root of the LISA noise PSD $S_n(f)$ from the LISA simulator (reproduced from [117]).

Apart from the noise PSD, another quantity is of particular interest when considering sensitivity curves, namely the energy density sensitivity. As a function of the noise PSD, it reads

$$\Omega_s(f) = \frac{4\pi^2}{3H_0^2} f^3 S_n(f), \tag{D.2}$$

where $H_0 \approx 67$ km s^{-1} Mpc^{-1} is the Hubble constant and S_n the noise PSD [119]. Note that the energy density was already introduced in Eq. (2.6) as the energy density per log-frequency interval. Similarly the energy density of the gravitational wave itself Ω_{GW} can be considered, after which the signal to noise ratio SNR can be defined:

$$\text{SNR} = \sqrt{T \int_{f_{min}}^{f_{max}} df \left(\frac{\Omega_{GW}(f)}{\Omega_s(f)} \right)^2}, \tag{D.3}$$

where f_{min} and f_{max} denote the minimal and maximal frequencies accessible at the detector and T is the observation time.

With the above ingredients, one can now compute the power law sensitivity curve (PLS). The PLS is such that a power law stochastic gravitational wave signal which lies above this curve has a SNR larger than a given threshold $\mathrm{SNR}_{\mathrm{thr}}$. To compute the PLS, one assumes the energy density of the gravitational wave takes the form of a power law, i.e. $\Omega_{GW}(f) = c_\beta f^\beta$, where c_β is a proportionality coefficient. For a wide range of values of β, ranging from negative values to positive values, the coefficient c_β is determined such that it provides a SNR equal to some threshold $\mathrm{SNR}_{\mathrm{thr}}$:

$$\mathrm{SNR}_{\mathrm{thr}} = \sqrt{T \int_{f_{min}}^{f_{max}} df \left(\frac{C_\beta^2 f^{2\beta}}{\Omega_s^2(f)} \right)}. \tag{D.4}$$

Attributing to each frequency the largest value of $c_\beta f^\beta$ yields the PLS, guaranteeing that a power law signal above this curve has an SNR value larger than $\mathrm{SNR}_{\mathrm{thr}}$. This PLS is given in Fig. 43 for a $\mathrm{SNR}_{\mathrm{thr}}$=10 and $T = 3$ years. This corresponds to a data-taking efficiency of about 75% of the 4 year LISA mission.

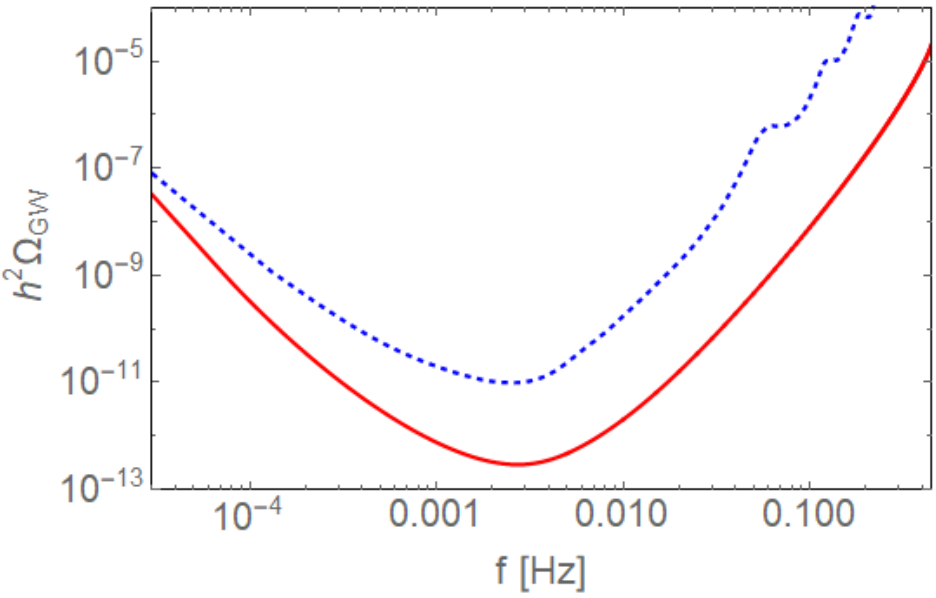

Figure 43: *Blue*: $h^2\Omega_s(f)$ computed using the noise spectral density $S_n(f)$. *Red*: Power law sensitivity curve for LISA with $\mathrm{SNR}_{\mathrm{thr}}$=10 and $T = 3$ years, corresponding to a data-taking efficiency of about 75% of the 4 year LISA mission.

References

[1] Mariano Quiros. 1999, hep-ph/9901312.

[2] Albert Einstein. *Sitzungsber. Preuss. Akad. Wiss. Berlin (Math. Phys.)*, 1916:688–696, 1916.

[3] Albert Einstein. *Sitzungsber. Preuss. Akad. Wiss. Berlin (Math. Phys.)*, 1918:154–167, 1918.

[4] Sean Carroll. Benjamin Cummings, 2003.

[5] C. A. Baker, D. D. Doyle, P. Geltenbort, K. Green, M. G. D. van der Grinten, P. G. Harris, P. Iaydjiev, S. N. Ivanov, D. J. R. May, J. M. Pendlebury, and et al. *Physical Review Letters*, 97(13), Sep 2006.

[6] M. Tanabashi et al. *Phys. Rev.*, D98(3):030001, 2018.

[7] Roberto D. Peccei. *Axions*, page 3–17, 2008.

[8] Roberto D Peccei and Helen R Quinn. *Phys. Rev. Lett.*, 38(ITP-568-STANFORD):1440–1443, 1977.

[9] P.S. Bhupal Dev, Francesc Ferrer, Yiyang Zhang, and Yongchao Zhang. *JCAP*, 11:006, 2019.

[10] Benedict Von Harling, Alex Pomarol, Oriol Pujolas, and Fabrizio Rompineve. 2019, 1912.07587.

[11] Luigi Delle Rose, Giuliano Panico, Michele Redi, and Andrea Tesi. 2019, 1912.06139.

[12] Sean M. Carroll. 1997, gr-qc/9712019.

[13] Nelson Christensen. *Rept. Prog. Phys.*, 82(1):016903, 2019.

[14] Michele Maggiore. Oxford University Press, 2018.

[15] J. H. Taylor and J. M. Weisberg. *Astrophys. J.*, 253:908–920, 1982.

[16] B. P Abbott et al. *Phys. Rev. Lett.*, 116:061102, Feb 2016.

[17] Yoichi Aso, Yuta Michimura, Kentaro Somiya, Masaki Ando, Osamu Miyakawa, Takanori Sekiguchi, Daisuke Tatsumi, and Hiroaki Yamamoto. *Physical Review D*, 88(4), Aug 2013.

[18] B. P. Abbott et al. *Phys. Rev.*, X9(3):031040, 2019.

[19] R. Hamburg et al. 2020, 2001.00923.

[20] Michele Maggiore et al. *JCAP*, 03:050, 2020.

[21] Wen-Hong Ruan, Chang Liu, Zong-Kuan Guo, Yue-Liang Wu, and Rong-Gen Cai. *Nat. Astron.*, 4:108–109, 2020.

[22] Pau Amaro-Seoane et al. 2017, 1702.00786.

[23] J I Read. *Journal of Physics G: Nuclear and Particle Physics*, 41(6):063101, May 2014.

[24] B.P. Abbott et al. *Phys.Rev.D*, 100(6):061101, 2019.

[25] T. Gold. *Nature*, 218:731–732, 1968.

[26] L. A. RAWLEY, J. H. TAYLOR, M. M. DAVIS, and D. W. ALLAN. *Science*, 238(4828):761–765, 1987.

[27] L. Lentati et al. *Mon. Not. Roy. Astron. Soc.*, 453(3):2576–2598, 2015.

[28] G. H. Janssen, G. Hobbs, M. McLaughlin, C. G. Bassa, A. T. Deller, M. Kramer,

K. J. Lee, C. M. F. Mingarelli, P. A. Rosado, S. Sanidas, A. Sesana, L. Shao, I. H. Stairs, B. W. Stappers, and J. P. W. Verbiest. 2014, 1501.00127.
[29] P. A. R. Ade et al. *Astron. Astrophys.*, 536:A1, 2011.
[30] Scott Koranda and Bruce Allen. *Phys. Rev.*, D52:1902–1919, 1995.
[31] B Allen and S Koranda. *Physical review. D, Particles and fields*, 50(6):3713—3737, September 1994.
[32] Michael Coughlin and Jan Harms. *Phys. Rev. D*, 90:042005, Aug 2014.
[33] Michele Maggiore. *Physics Reports*, 331(6):283–367, Jul 2000.
[34] Richard H. Cyburt, Brian D. Fields, Keith A. Olive, and Evan Skillman. *Astroparticle Physics*, 23(3):313–323, 4 2005.
[35] M Punturo et al. *Classical and Quantum Gravity*, 27(19):194002, sep 2010.
[36] Chia-Feng Chang and Yanou Cui. 2019, 1910.04781.
[37] B. P. Abbott et al. *Phys. Rev. Lett.*, 116(13):131102, 2016.
[38] Greg W. Anderson and Lawrence J. Hall. *Phys. Rev. D*, 45:2685–2698, Apr 1992.
[39] Cédric Delaunay, Christophe Grojean, and James D Wells. *Journal of High Energy Physics*, 2008(04):029–029, Apr 2008.
[40] Sidney R. Coleman. *Phys. Rev. D*, 15:2929–2936, 1977. [Erratum: Phys.Rev.D 16, 1248 (1977)].
[41] Jr. Callan, Curtis G. and Sidney R. Coleman. *Phys. Rev. D*, 16:1762–1768, 1977.
[42] Andrei D. Linde. *Nucl. Phys. B*, 216:421, 1983. [Erratum: Nucl.Phys.B 223, 544 (1983)].
[43] Gerald V. Dunne and Hyunsoo Min. *Physical Review D*, 72(12), Dec 2005.
[44] Victor Guada, Miha Nemevšek, and Matevž Pintar. 2020, 2002.00881.
[45] John Ellis, Marek Lewicki, and José Miguel No. *Journal of Cosmology and Astroparticle Physics*, 2019(04):003–003, Apr 2019.
[46] Iason Baldes and Camilo Garcia-Cely. *Journal of High Energy Physics*, 2019(5), May 2019.
[47] Alan H. Guth and S.H.H. Tye. *Phys. Rev. Lett.*, 44:631, 1980. [Erratum: Phys.Rev.Lett. 44, 963 (1980)].
[48] Alan H. Guth and Erick J. Weinberg. *Phys. Rev. D*, 23:876–885, Feb 1981.
[49] Michael S. Turner, Erick J. Weinberg, and Lawrence M. Widrow. *Phys. Rev. D*, 46:2384–2403, Sep 1992.
[50] Chiara Caprini et al. *JCAP*, 1604(04):001, 2016.
[51] Marc Barroso Mancha, Tomislav Prokopec, and Bogumila Swiezewska. 2020, 2005.10875.
[52] Guy D. Moore and Tomislav Prokopec. *Physical Review D*, 52(12):7182–7204, Dec 1995.
[53] Guy D Moore. *Journal of High Energy Physics*, 2000(03):006–006, Mar 2000.
[54] Ariel Mégevand and Alejandro D. Sánchez. *Nuclear Physics B*, 825(1-2):151–176, Jan 2010.
[55] Ariel Mégevand. *Journal of Cosmology and Astroparticle Physics*, 2013(07):045–045, Jul 2013.
[56] Dietrich Bödeker and Guy D Moore. *Journal of Cosmology and Astroparticle*

Physics, 2009(05):009–009, May 2009.
[57] Dietrich Bödeker and Guy D. Moore. *Journal of Cosmology and Astroparticle Physics*, 2017(05):025–025, May 2017.
[58] Vincent Corbin and Neil J Cornish. *Classical and Quantum Gravity*, 23(7):2435–2446, Mar 2006.
[59] John Ellis, Marek Lewicki, and José Miguel No. 2020, 2003.07360.
[60] Chiara Caprini et al. 2019, 1910.13125.
[61] José R Espinosa, Thomas Konstandin, José M No, and Géraldine Servant. *Journal of Cosmology and Astroparticle Physics*, 2010(06):028–028, Jun 2010.
[62] Mark Hindmarsh, Stephan J. Huber, Kari Rummukainen, and David J. Weir. *Phys. Rev.*, D92(12):123009, 2015.
[63] Daniel Cutting, Mark Hindmarsh, and David J. Weir. 2019, 1906.00480.
[64] Michael E. Peskin and Daniel V. Schroeder. Addison-Wesley, Reading, USA, 1995.
[65] Steven Weinberg. *Phys. Rev. D*, 11:3583–3593, Jun 1975.
[66] Stephen L. Adler. *Phys. Rev.*, 177:2426–2438, Jan 1969.
[67] John S Bell and Roman Jackiw. *Il Nuovo Cimento A (1965-1970)*, 60(1):47–61, 1969.
[68] William A Bardeen. *Nuclear Physics B*, 75(2):246–258, 1974.
[69] Alexander A Belavin, Alexander M Polyakov, Albert S Schwartz, and Yu S Tyupkin. *Physics Letters B*, 59(1):85–87, 1975.
[70] Sidney Coleman. Cambridge University Press, 1988.
[71] M Aubry. Birkhäuser Verlag, 1995.
[72] Ta-Pei Cheng, Ling-Fong Li, and Ta-Pei Cheng. 1984.
[73] Curtis G Callan Jr, RF Dashen, and David J Gross. pages 29–35. World Scientific, 1994.
[74] Ramamurti Rajaraman. 1982.
[75] Anson Hook. *PoS*, TASI2018:004, 2019.
[76] David B. Kaplan. 2009, 0912.2560.
[77] Mark Srednicki. Cambridge Univ. Press, Cambridge, 2007.
[78] Ann E. Nelson. *Phys. Lett. B*, 136:387–391, 1984.
[79] S. M. Barr. *Phys. Rev. Lett.*, 53:329–332, Jul 1984.
[80] David B. Kaplan and Aneesh V. Manohar. *Phys. Rev. Lett.*, 56:2004–2007, May 1986.
[81] Jürg Gasser and Hubert Leutwyler. *Physics Reports*, 87(3):77–169, 1982.
[82] Marco Gorghetto and Giovanni Villadoro. *Journal of High Energy Physics*, 2019(3), Mar 2019.
[83] Michael Dine, Willy Fischler, and Mark Srednicki. *Phys. Lett.*, 104B:199–202, 1981.
[84] A. R. Zhitnitsky. *Sov. J. Nucl. Phys.*, 31:260, 1980. [Yad. Fiz.31,497(1980)].
[85] Jihn E. Kim. *Phys. Rev. Lett.*, 43:103, 1979.
[86] Mikhail A. Shifman, A. I. Vainshtein, and Valentin I. Zakharov. *Nucl. Phys.*, B166:493–506, 1980.
[87] Giovanni Grilli di Cortona, Edward Hardy, Javier Pardo Vega, and Giovanni Vil-

ladoro. *Journal of High Energy Physics*, 2016(1), Jan 2016.
[88] R. et al. Ballou. *Physical Review D*, 92(9), Nov 2015.
[89] *Nature Physics*, 13(6):584–590, May 2017.
[90] Adrian Ayala, Inma Domínguez, Maurizio Giannotti, Alessandro Mirizzi, and Oscar Straniero. *Physical Review Letters*, 113(19), Nov 2014.
[91] Tobias Fischer, Sovan Chakraborty, Maurizio Giannotti, Alessandro Mirizzi, Alexandre Payez, and Andreas Ringwald. *Physical Review D*, 94(8), Oct 2016.
[92] K. A. Olive et al. *Chin. Phys.*, C38:090001, 2014.
[93] Jae Hyeok Chang, Rouven Essig, and Samuel D. McDermott. *Journal of High Energy Physics*, 2018(9), Sep 2018.
[94] M.E. Carrington. *Phys. Rev. D*, 45:2933–2944, 1992.
[95] F. Csikor, Z. Fodor, and J. Heitger. *Phys. Rev. Lett.*, 82:21–24, 1999.
[96] K. Kajantie, M. Laine, K. Rummukainen, and M. Shaposhnikov. *Nuclear Physics B*, 466(1-2):189–258, Apr 1996.
[97] Michela D'Onofrio and Kari Rummukainen. *Phys. Rev. D*, 93(2):025003, 2016.
[98] Archil Kobakhidze, Cyril Lagger, Adrian Manning, and Jason Yue. *The European Physical Journal C*, 77(8), Aug 2017.
[99] Archil Kobakhidze. 2012, 1208.5180.
[100] M. Punturo et al. *Class. Quant. Grav.*, 27:194002, 2010.
[101] Denis Martynov, Haixing Miao, Huan Yang, Francisco Hernandez Vivanco, Eric Thrane, Rory Smith, Paul Lasky, William E. East, Rana Adhikari, Andreas Bauswein, and et al. *Physical Review D*, 99(10), May 2019.
[102] Iason Baldes, Thomas Konstandin, and Geraldine Servant. *Phys. Lett. B*, 786:373–377, 2018.
[103] Iason Baldes, Thomas Konstandin, and Geraldine Servant. *JHEP*, 12:073, 2016.
[104] Daniel Egana-Ugrinovic. *JHEP*, 12:064, 2017.
[105] Marcela Carena, Ariel Megevand, Mariano Quiros, and Carlos E.M. Wagner. *Nucl. Phys. B*, 716:319–351, 2005.
[106] Brian Henning, Xiaochuan Lu, and Hitoshi Murayama. 2014, 1412.1837.
[107] John Ellis, Marek Lewicki, and Jose Miguel No. *Submitted to: JCAP*, 2018.
[108] Jeff Crowder and Neil J. Cornish. *Phys. Rev.*, D72:083005, 2005.
[109] Fred C. Adams. *Physical Review D*, 48(6):2800–2805, Sep 1993.
[110] I.Yu. Kobzarev, L.B. Okun, and M.B. Voloshin. *Sov. J. Nucl. Phys.*, 20:644–646, 1975.
[111] Duncan Meacher, Michael Coughlin, Sean Morris, Tania Regimbau, Nelson Christensen, Shivaraj Kandhasamy, Vuk Mandic, Joseph D. Romano, and Eric Thrane. *Physical Review D - Particles, Fields, Gravitation and Cosmology*, 92(6), September 2015.
[112] Anson Hook, Soubhik Kumar, Zhen Liu, and Raman Sundrum. 2019, 1911.12364.
[113] Matthew J. Dolan, Torben Ferber, Christopher Hearty, Felix Kahlhoefer, and Kai Schmidt-Hoberg. *Journal of High Energy Physics*, 2017(12), Dec 2017.
[114] T. Abe et al. 2010, 1011.0352.
[115] SHiP Collaboration. 2015, 1504.04956.

[116] M. et al. Bicer. *Journal of High Energy Physics*, 2014(1), Jan 2014.
[117] Chiara Caprini, Daniel G. Figueroa, Raphael Flauger, Germano Nardini, Marco Peloso, Mauro Pieroni, Angelo Ricciardone, and Gianmassimo Tasinato. *JCAP*, 11(11):017, 2019.
[118] C J Moore, R H Cole, and C P L Berry. *Classical and Quantum Gravity*, 32(1):015014, Dec 2014.
[119] Michele Maggiore. Oxford Master Series in Physics. Oxford University Press, 2007.